The Messenger

No. 129 – September 2007

LABOCA commissioned on APEX
Testing of Multi-conjugate AO Demonstrator
Astroparticle Physics in Europe
Weighing Ultracompact Dwarf Galaxies

A New Era in Submillimetre Continuum Astronomy has Begun: LABOCA Starts Operation on APEX

Giorgio Siringo[1]
Axel Weiss[1]
Ernst Kreysa[1]
Frederic Schuller[1]
Attila Kovacs[1]
Alexandre Beelen[1,2]
Walter Esch[1]
Hans-Peter Gemünd[1]
Nikhil Jethava[1]
Gundula Lundershausen[1]
Karl M. Menten[1]
Rolf Güsten[1]
Frank Bertoldi[3]
Carlos De Breuck[4]
Lars-Åke Nyman[4]
Eugene Haller[5]
Jeff Beeman[5]

[1] Max-Planck-Institut für Radioastronomie, Bonn, Germany
[2] Institut d'Astrophysique Spatiale, Université Paris-Sud, Paris, France
[3] Argelander-Institut für Astronomie, Universität Bonn, Germany
[4] ESO
[5] Lawrence Berkeley National Laboratory, Berkeley, California, USA

In May 2007, the Large APEX Bolometer Camera LABOCA was commissioned as a facility instrument on the APEX 12-m submillimetre telescope located at an altitude of 5100 m in northern Chile. The new 870-μm bolometer camera, in combination with the high efficiency of APEX and the excellent atmospheric transmission at the site, offers unprecedented capability in mapping submillimetre continuum emission. An overview of LABOCA and the prospects for science are presented.

A technological challenge

A new facility instrument has started operation on the APEX telescope (Atacama Pathfinder Experiment, Güsten et al., 2006) as a collaborative effort between the Max-Planck-Institut für Radioastronomie in Bonn (MPIfR), ESO and the Onsala Space Observatory (OSO). The new Large APEX BOlometer CAmera (LABOCA) is an array of bolometers designed for fast mapping of large sky areas at high angular resolution and with high sensitivity: a challenging task. Developed by the Bolometer Group of the MPIfR, LABOCA is the most complex system ever developed by this group. The design of this new facility takes advantage of the experience accumulated over several years in developing bolometers for millimetric and submillimetric atmospheric windows and operating them on ground-based telescopes.

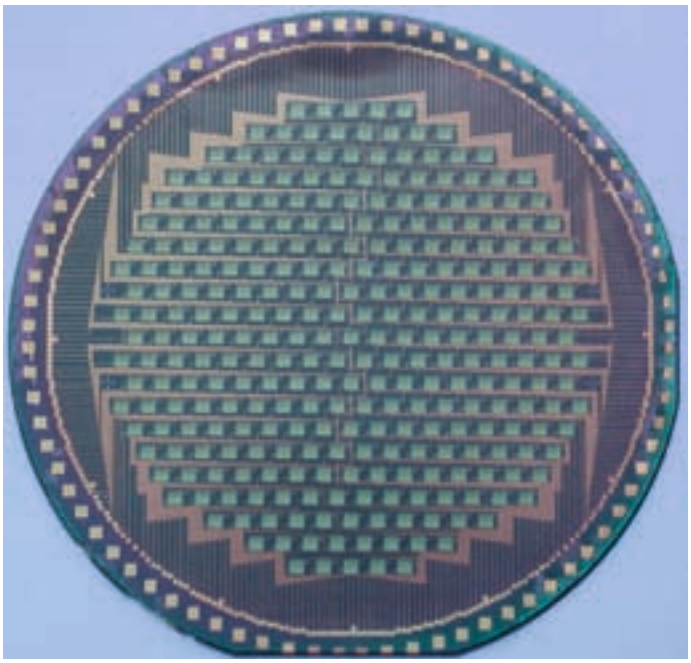

Figure 1: A 'naked' LABOCA silicon wafer. Each small square is a bolometer.

The main obstacle, when observing at millimetre and submillimetre wavelengths, is our Earth's atmosphere, which is seen by a bolometer like a bright screen. It is as difficult as trying to do astronomical observations in the optical during daytime. This is largely due to the water vapour present in the atmosphere, with only small contributions from other components, like ozone. In the submillimetre range the only sources in the sky brighter than the atmosphere are the planets Venus, Mars, Jupiter and Saturn (and, of course, the Sun and the Moon). All other celestial objects have weaker fluxes, usually orders of magnitude weaker than the atmospheric emission. Besides, the atmosphere is not stable and the amount of water vapour along the line of sight can change quickly, giving rise to instabilities of emission and transmission, called 'sky noise'.

Observations of astronomical objects from ground-based telescopes have to pierce that screen presented by the atmosphere, therefore requiring techniques to minimise its effects. The most widely-used technique is application of a switching device, usually a chopping secondary mirror (commonly called a 'wobbler'), to observe alternatively the source and an area of blank sky close by, at a frequency higher than the variability of the sky noise. Invented for observations with single pixel detectors, this method is also used with arrays of bolometers. However, it presents some disadvantages and the most evident are, among others, that the wobbler is usually slow (1 or 2 Hz), posing a limitation to the scanning speed, and that not all telescopes are equipped with a wobbler.

LABOCA has been specifically designed to work without a wobbler to remove the atmospheric contribution, using a different technique which well suits observations with an array of detectors. This technique, called 'fast scanning' (Reichertz et al. 2001), is based on the idea that, when observing with an array, each unit bolometer looks at a different part of the sky and chopping is no longer needed. A modulation of the signal is produced by moving the telescope across the source field of interest. The atmospheric contribution (as well as part of the instrumental

noise) will be strongly correlated in all bolometers and a post-detection analysis of the correlation across the array will allow extraction of the signals of astronomical interest from the atmospheric foregrounds. The post-detection bandwidth is defined by the beam size and by the scanning speed; relatively high scanning speeds are ideal. This technique was first tested by the MPIfR bolometer group in 2000 with the MAMBO (Max-Planck Millimetre Bolometer, Kreysa et al. 1999) array of 37 bolometers, installed on the IRAM 30-m telescope (Instituto de Radioastronomía Milimétrica, Pico Veleta, Spain; Baars et al. 1987). The same technique was extensively used in the following years for observations with the SIMBA (SEST Imaging Bolometer Array, Nyman et al. 2001) bolometer array on the SEST (Swedish-ESO Submillimetre Telescope, La Silla, Chile; Booth et al. 1989) telescope, which is not equipped with a chopping secondary mirror.

The experience with MAMBO and SIMBA has been essential for the design of LABOCA, which represents the evolution to a receiver specifically optimised for the fast scanning technique. Challenging technological choices have been implemented in its design. The most evident is the large number of pixels (nominally 295, see Figure 1), making the correlation removal extremely efficient. Another point is the large post-detection bandwidth. SIMBA was built following the same design scheme as MAMBO: that is both receivers are optimised for the differential technique with a wobbler, and a high-pass filter is used to cut off frequencies below the chopping frequency. LABOCA, instead, is a true total power system (without high-pass filtering) with a large stable post-detection bandwidth, extending down to 0.1 Hz. Moreover the reduction of the data acquired in fast scanning requires the use of special algorithms (Weferling et al. 2002) and the lack of a software package ready to reduce the data was the major drawback of the fast scanning technique applied to MAMBO and SIMBA. For this reason, in parallel with the hardware development of LABOCA, completely new software was developed, the Bolometer Data Analysis package (BoA, Schuller et al., in prep.), which is able to reduce data acquired with LABOCA in any of the possible observing modes.

APEX is the ideal telescope for using the fast scanning technique as it can move extremely fast and its control software allows new observing patterns which fit well to the fast scanning technique. The 5100 metre high site on Llano de Chajnantor, where APEX is located, on the one hand can make the maintenance of the system uncomfortable, but on the other hand provides excellent atmospheric conditions for most of the year.

Figure 2: LABOCA in the Cassegrain cabin of the APEX telescope. The receiver is in the centre of the picture. Four of the five mirrors used for the optical coupling are visible.

Technical overview

The detector array of LABOCA is micromachined on a 4-inch (102-mm) silicon wafer where unstructured silicon nitride membranes carry the composite bolometers. The membranes are only 0.4 µm thick and are coated with a thin titanium film which absorbs the incoming radiation. Neutron-transmutation-doped (NTD) germanium chips (called thermistors), soldered to the membranes, detect the temperature rise due to the absorption of the radiation. The array is mounted inside a cryostat, which uses liquid nitrogen and liquid helium for thermal shielding and pre-cooling of the array. A closed-cycle double-stage sorption cooler is then used to reach a stable operation temperature of 0.285 K. The cryostat is mounted in the Cassegrain cabin of the telescope (see Figure 2) and the optical coupling to the main telescope beam is provided by a series of metal mirrors and a lens placed at the cryostat entrance. A set of cold filters, mounted on the liquid nitrogen and liquid helium shields, define the spectral passband, centred at a wavelength of 870 µm (345 GHz) and about 150 µm (60 GHz) wide (see Figure 3). A monolithic array of conical horn antennas, placed in front of the bolometer wafer, collects the radiation onto the bolometers. One LABOCA beam is 18.6 arcseconds wide (full width at half maximum, FWHM) and the field of view (FoV) of the complete array covers 11.4 arcminutes. The array undersamples the sky, with a distance of two beams between adjacent pixels

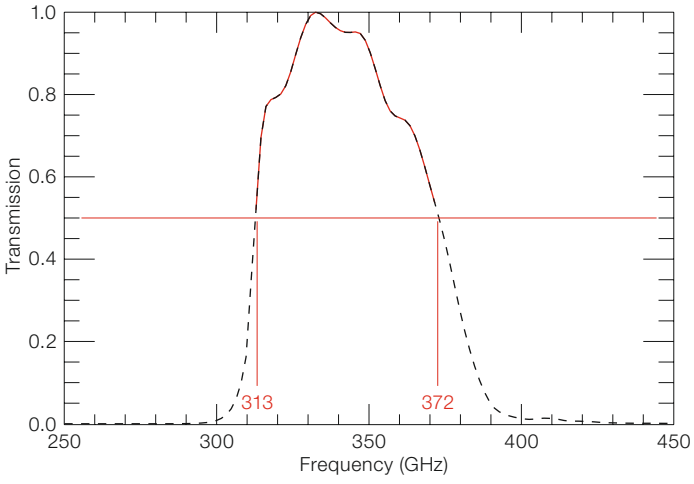

Figure 3: Spectral response of LABOCA. The central frequency is 345 GHz and the 50 % transmission is between 313 and 372 GHz.

(see Figure 4). The voltages at the edges of the thermistors are channelled to the outside of the cryostat along 12 flat cables (made of manganin wires on kapton substrate) going through low-noise, unity gain JFET amplifiers heat sinked to the liquid nitrogen bath. Upon exiting the cryostat, the signals pass to room-temperature low-noise amplifiers and electronics. The 295 signals are distributed to four identical, custom made, amplification units, providing 80 channels each for a total of 320 available channels. The extra 25 channels are used for technical purposes like noise monitoring and calibrations. The amplification units are equipped with microprocessors providing a digital interface, accessible remotely via the local network, to control some of their properties, like the amplification gain which can be set in the range 270–17 280.

At the beginning of each observation, the DC offset is removed from each channel to avoid the risk of saturation. The values of the 320 removed offsets are temporarily stored in a local memory and, at the end of the observation, are written in the corresponding data file, to be used during the data-reduction process. The 320 channels are digitized over 16 bits by four multifunction DAQ PCI boards mounted in an industrial computer. The data-acquisition software provides an interface to the APEX control software, used to set up the hardware, and a TCP data server, for the data output. The amplification units provide an AC current to bias the bolometers and perform real-time demodulation of the 320 signals. This electronic scheme is fundamental for the stability of the post-detection signals at low frequencies. The AC bias frequency is provided by the data acquisition system as a submultiple of the sampling frequency (usually set to 1 kHz) thus synchronising the bias to the data sampling. Before reaching the telescope's control software, the data (about 4 MB/s) are digitally filtered and downsampled to 25–50 Hz in real time by a computer specifically equipped for bridging between data-acquisition and control software. Another computer is devoted to monitoring and control of most of the electronics embedded in the receiver (e.g. monitoring of all the temperature stages, control of the sorption cooler, calibration unit,

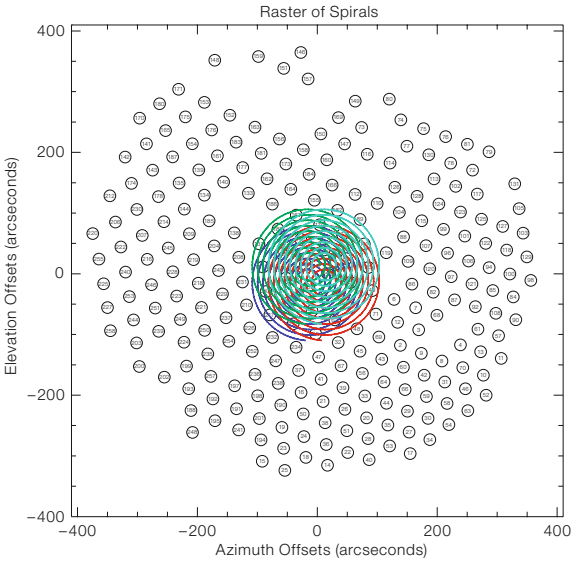

Figure 4: The coloured lines show the scanning pattern of a single bolometer for a four-point raster of spirals. The circles show the measured positions and sizes on sky of all the functional LABOCA detectors.

etc.) and also provides an interface to the APEX control software, allowing remote operation of the system.

Observing modes and performance on the sky

In order to reach the best signal-to-noise ratio using the fast scanning technique with LABOCA, the frequencies of the signal produced by scanning across the source need to match the white noise part of the post-detection frequency band (0.1–20 Hz), mostly above the frequencies of the atmospheric fluctuation. The maximum telescope scanning speed for LABOCA is limited by the time resolution of the position information given by the APEX control system, that is about 4 arcminutes/s. The minimum scanning speed required for a sufficient source modulation depends on the atmospheric stability and on the source structure and is typically about 3 arcseconds/s.

The APEX control system currently supports two basic scanning modes: on-the-fly (OTF) maps and spiral scanning patterns. OTF scans are rectangular scanning patterns, with a constant scanning speed, in horizontal or equatorial coordinates. The OTF pattern is typically used to map sky areas much larger than the FoV of LABOCA (i.e. greater than 30 arcminutes). For compact objects, or pointing and flux calibrations, the spiral scanning pattern provides the faster method to obtain a fully sampled coverage of the FoV of LABOCA at the required scanning speed. In this mode the telescope scans with a constant angular speed along a spiral, in horizontal or equatorial coordinates. A single spiral is typically much smaller than the FoV and can be repeated on a raster pattern to increase the sampling density. Figure 4 shows the path of a single bolometer for a four-point raster of spirals, plotted over the measured footprint on the sky of all the functional bolometers of the array.

The attenuation of the astronomical signals due to the atmospheric opacity is determined with skydips. These scans measure the power of the atmospheric emission as a function of the airmass while tipping the telescope from high to low elevation. Further details on the LABOCA observing modes are accessible at *www.apex-telescope.org/bolometer/laboca.*

During the science verification run in May 2007, the sensitivity on sky (noise equivalent flux density or NEFD) of LABOCA has been determined to be 75 mJy·s$^{1/2}$ (root mean square of weighted average of all 250 functional bolometers). In typical observing conditions of 1 mm of precipitable water vapour (which corresponds to a zenith opacity τ = 0.3), this sensitivity translates into a mapping speed of 1 square degree per hour down

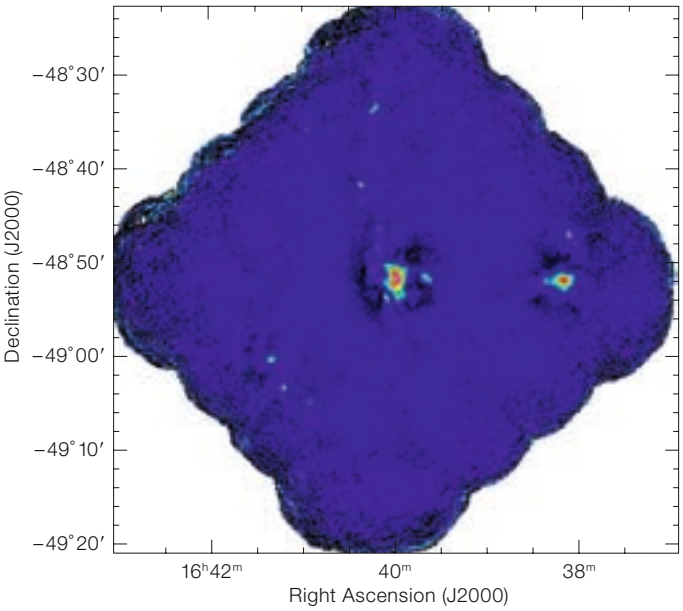

Figure 5: Quarter square degree map observed with LABOCA towards the reflection nebula NGC 6188. The total observing time for this field is only 30 min resulting in a noise level of 35 mJy/beam. The map is a mosaic of raster-spiral patterns.

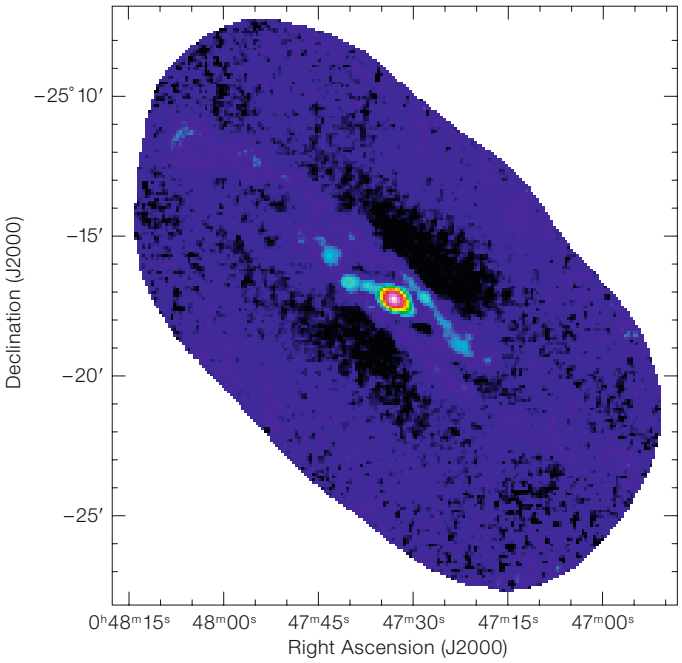

Figure 6: 870 μm emission of the nuclear starburst galaxy NGC 253. The map reveals for the first time the full extension of the low surface-brightness emission arising from the spiral arms in this galaxy.

to a noise level of 40 mJy/beam. An online time estimator for LABOCA is available at *www.apex-telescope.org/bolometer/laboca/obscal.*

Science with LABOCA

On account of its spectral passband, centred at a wavelength of 870 μm, LABOCA is particularly sensitive to thermal emission from cold objects which is of great interest for a number of astrophysical research fields.

Planet formation

The study of Kuiper Belt Objects in the Solar System as well as observations of debris discs of cold dust around nearby main-sequence stars can give vital clues to the formation of our own Solar System and planets in general. With the angular resolution of 18.6 arcseconds, LABOCA will be capable of resolving the debris discs of nearby stars.

Star formation in the Milky Way

The outstanding power of LABOCA in mapping large areas of the sky with high sensitivity (see Figure 5) will allow, for the first time, unbiased surveys of the distribution of the cold dust in the Milky Way to be performed.

As the dust emission at 870 μm is typically optically thin, it is a direct tracer of the gas column density and gas mass. Large-scale surveys in the Milky Way will reveal the distribution and gas properties of a large number of pre-stellar cores in different environments and evolutionary states. Equally importantly, they provide information on the structure of the interstellar medium on large scales at high spatial resolution, an area little explored so far. Such surveys are vital to improve our understanding of the processes that govern star formation as well as the relation between the clump mass spectrum and the stellar initial mass function (IMF).

Large unbiased surveys are also critical for finding precursors of high-mass stars which are undetectable at other wavelengths due to the high obscuration of the massive cores in which they are embedded. LABOCA will help to obtain a detailed understanding of their evolution. In addition, deep surveys of nearby, star-forming clouds, will allow the study of the pre-stellar mass function down to the brown dwarf regime.

Cold gas in Galaxies

The only reliable way to trace the bulk of dust in galaxies is through imaging at submillimetre wavelengths. It is becoming clear that most of the dust mass in spiral galaxies lies in cold, low-surface brightness discs, often extending far from the galactic nucleus (as in the case of the starburst galaxy NGC 253, see Figure 6). Understanding this component is critically important as it dominates the total gas mass in galaxies. For example studies of the Schmidt Law, based on H I observations alone, heavily underestimate the gas surface density in the outer parts of galaxies. In addition to studying individual nearby galaxies, LABOCA will be vital for determining low-*z* benchmarks, such as the local luminosity and dust mass functions, which are required to interpret information from deep cosmological surveys.

Galaxy formation at high redshift

Owing to the advantageous interaction of redshift and the cool dust spectral energy distribution (negative-K correction), submillimetre observations offer equal sensitivity to dusty star forming galaxies over a redshift range from $z \sim 1$–10 and therefore provide information on the star formation history at epochs from about half to only 5 % of the present age of the Universe. Recent studies have shown that the volume density of luminous submillimetre galaxies (SMGs) increases over a thousand-fold out to $z < 2$ (Chapman et al. 2005), and thus, in contrast to the local Universe, luminous obscured galaxies at high redshift could dominate the total bolometric emission from all galaxies at early epochs. These studies also suggest that approximately half of all the stars that have formed by the present day may have formed in highly obscured systems which remain undetected in the optical or NIR. One example of such a source is SMM 14009+0252 (see Figure 7) which is strong in the submillimetre and has a 1.4 GHz radio counterpart, but no obvious counterpart in deep *K*-band images (Ivison et.al. 2000). Clearly it is critical to include these highly-obscured sources in models of galaxy formation in order to obtain a complete understanding of the evolution of galaxies. With its fast mapping capabilities, LABOCA allows us to map fields of half a square degree, typical of the size of deep cosmological fields observed at other wavelengths, down to the confusion limit in a reasonable amount of observing time. These deep observations will also greatly improve the statistics of high-redshift galaxies detected at submillimetre wavelengths.

A set of science verification projects has been observed with LABOCA. The raw and reduced data are publicly available from *http://www.eso.org/sci/activities/apexsv/labocasv/index.html* where more details of the SV programme can be found.

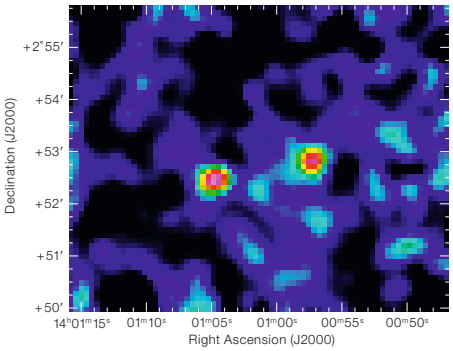

Figure 7: LABOCA image of SMM 14011+0252 (left) and SMM 14009+0252 (right) smoothed to 25 arcsecond resolution. Both submillimetre galaxies were first detected by SCUBA (Ivison et al. 2000). SMM 14011 is at a redshift of $z = 2.56$ (confirmed by CO detections) while SMM 14009 has no clear optical counterpart and therefore no reliable redshift determination. The noise level of the map is about 2.5 mJy/beam.

Acknowledgements

We acknowledge the APEX staff for their support during installation and commissioning. For the fabrication of the LABOCA wafer, Ernst Kreysa enjoyed the hospitality of the microfabrication laboratory of University of California at Berkeley.

References

Baars J. W. M. et al. 1987, A&A 175, 319
Booth R. S. et al. 1989, A&A 216, 315
Chapman S. C. et al. 2005, ApJ 622, 722
Nyman L.-Å. 2001, The Messenger 106, 40
Güsten R. et al. 2006, A&A 454L, 13
Ivison R. J. et al. 2000, MNRAS 315, 209
Kreysa E. et al. 2002, AIPC 616, 262
Reichertz L. A. et al. 2001, A&A 379, 735
Weferling B. et al. 2002, A&A 383, 1088

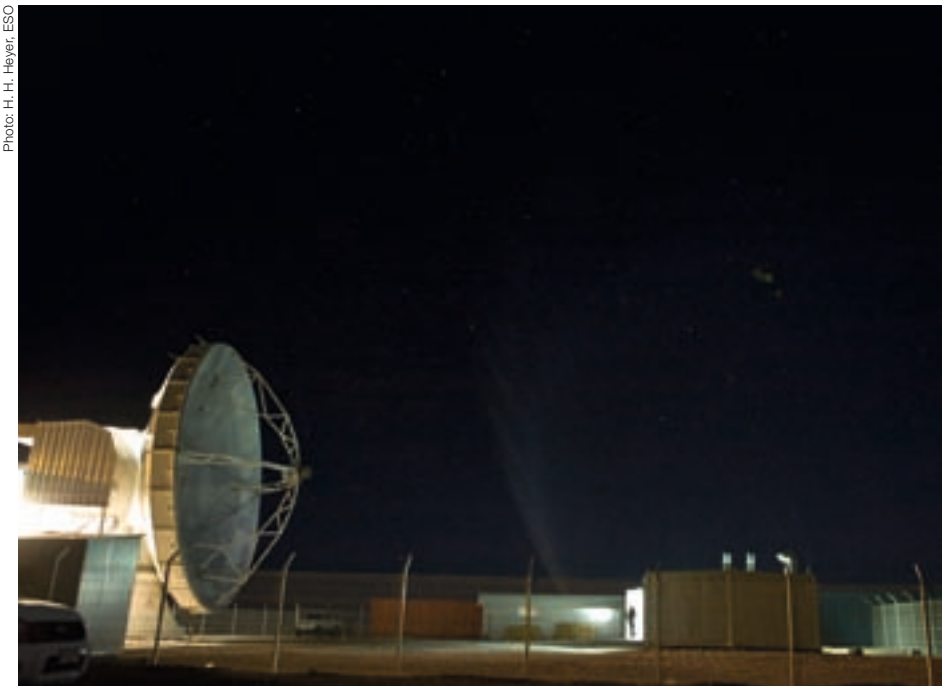

Photo: H. H. Heyer, ESO

Left: A view of Comet McNaught, with APEX in the foreground. The photograph was taken on 23 January 2007 when the comet was 10 days past its peak brightness.

Right: APEX/LABOCA 870 micron image of the Horsehead nebula (NGC 2023, also called Barnard 33). The image covers 8.5 by 10.5 arcminutes, and has a spatial resolution of 18.6 arcsec. The inset shows the VLT FORS1 three colour image (from *B*, *V* and *R* filters) of the central 6.5 × 6.7 arcminute (see ESO PR Photo 02a-02 for details). LABOCA traces the emission of the cool dust, which is however seen in absorption in the optical image. LABOCA image produced by the MPIfR LABOCA commissioning team.

On-sky Testing of the Multi-Conjugate Adaptive Optics Demonstrator

Enrico Marchetti[1]
Roland Brast[1]
Bernard Delabre[1]
Robert Donaldson[1]
Enrico Fedrigo[1]
Christoph Frank[1]
Norbert Hubin[1]
Johann Kolb[1]
Jean-Louis Lizon[1]
Massimiliano Marchesi[1]
Sylvain Oberti[1]
Roland Reiss[1]
Joana Santos[1]
Christian Soenke[1]
Sebastien Tordo[1]
Andrea Baruffolo[2]
Paolo Bagnara[2]
The CAMCAO consortium[3]

[1] ESO
[2] INAF – Astronomical Observatory of Padova, Italy
[3] Universidade de Lisboa, Portugal

The aim of the Multi-Conjugate Adaptive Optics Demonstrator (MAD) is to correct for atmospheric turbulence over a field of view which is much larger than the one typically covered by the existing adaptive optics systems installed on 8-m-class telescopes. After a long period of testing at the ESO premises, MAD was installed at the VLT early in 2007 in order to evaluate its correction performance. Here we present the MAD project and the recent results obtained during the on-sky testing at the VLT UT3 telescope Melipal.

MAD (Marchetti et al. 2006) is a demonstrator instrument aimed at correcting atmospheric turbulence over a large field of view by implementing a novel adaptive optics technique called Multi-Conjugate Adaptive Optics (MCAO).

MCAO and similar atmospheric turbulence correction techniques have been recognised as strategic both for the second-generation VLT instrumentation and for the European Extremely Large Telescope (Gilmozzi and Spyromilio 2007), the 42-m telescope facility whose project is in development at ESO. In fact both the above-mentioned projects will make extensive use of wide-field-of-view adaptive optics correction systems for sharpening the astronomical images, before feeding them into the scientific instrument.

In this framework the final goal of MAD is to prove, on-sky, the feasibility of MCAO and related techniques, and to evaluate all the technical issues as well as to identify the key aspects involving the design, construction and operation of such systems.

MAD is not a fully internal ESO project as it has benefited from the collaboration of two consortia to develop some strategic components of the system. A consortium led by Universidade de Lisboa (Portugal) designed and built the Camera for MCAO (CAMCAO), which is a high spatial resolution infrared imaging camera used by MAD for evaluating the correction performance. An Italian consortium formed by the Observatories of Padova and Arcetri, both part of the Italian National Institute for Astrophysics (INAF), developed the instrument control software and a novel concept of wavefront sensor, called Layer Oriented, which will be tested separately on the sky in September 2007 (Vernet-Viard et al. 2005).

What is MCAO?

Adaptive optics corrects in real time for the atmospheric turbulence which affects the spatial resolution of the astronomical images obtained by ground based telescopes. In the existing adaptive optics systems, the field of view which benefits from the real-time atmospheric turbulence correction is very limited, typically a few arcseconds for images obtained at infrared wavelengths. This limitation arises from the fact that the distorted wavefront is estimated by the wavefront sensor only in the direction of a sufficiently bright guide star located near the observed astronomical object, and is corrected for this same direction by a deformable mirror. In this configuration, only the volume of the atmosphere probed by the beam of the observed guide star is efficiently sensed, while the atmospheric volumes probed by the light of astronomical objects far from the guide star are only partially sensed. The direct consequence of this misregistration is that the images of the astronomical objects far from the guide star are only partially corrected, with a blurring size which increases with the distance from the guide star. This phenomenon is called atmospheric anisoplanatism and a graphical representation is given in Figure 1.

MCAO tries to overcome this limitation by sensing and correcting for the whole atmospheric volume probed by the observed field of view (Beckers 1988). The process of implementing MCAO correction consists of three main steps. The first one is to measure the deformation of the wavefront due to the atmospheric turbulence along different directions in the field of view. This is performed with several wavefront sensors looking at different guide stars in the field of view. The greater the number of guide stars, the better the knowledge of the wavefront distortion in the sky field of interest. The second step is called atmospheric tomography and consists in reconstructing the vertical distribution of the atmospheric turbulence at different locations of the field, in order to obtain a three-dimensional mapping of the turbulence above the telescope. The solution to this step represents quite a complex problem, since the number of measurable quantities (the guide stars) is always smaller than the number of the unknown ones (the turbulence at several discrete altitudes above the telescope). This limitation comes from the fact that, while the vertical distribution of the atmospheric turbulence is continuous, the number of available guide stars is always limited to a few, both for natural and technical reasons.

The atmospheric tomography problem, which is quite complex and requires some a priori assumptions to achieve a simplified solution, has been already given in its theoretical form (Ragazzoni, Marchetti and Rigaut 1998) and then demonstrated in an open-loop experiment on the sky (Ragazzoni, Marchetti and Valente 2000). The third step is to apply the wavefront correction to the whole field of view and not only in a specified direction. This is achievable by using several deformable mirrors which are optically conjugated to different altitudes in the atmosphere above the telescope. The deformable mirrors intercept the light

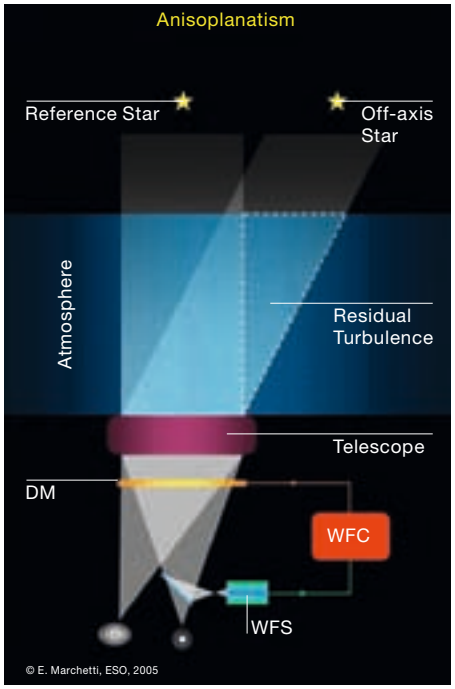

Figure 1: Graphical representation of the atmospheric anisoplanatism effect for a classical Adaptive Optics system. By means of the wavefront sensor (WFS), the wavefront computer (WFC) and the deformable mirror (DM), the system senses, computes the correction and applies it only in the direction of the guide star. The stars not in the direction of the correction see a different portion of the atmosphere, which is partially corrected, and thus appear blurred.

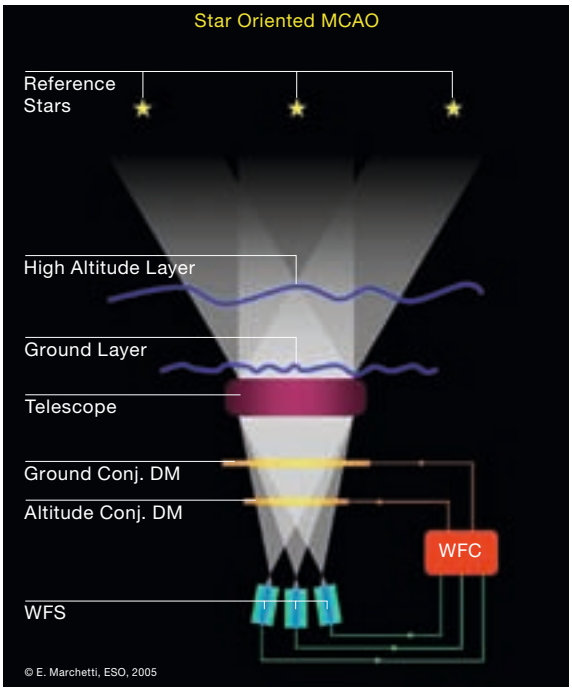

Figure 2: Graphical representation of Multi-Conjugate Adaptive Optics in Star Oriented configuration. Many guide stars are simultaneously sensed to probe the full volume of atmospheric turbulence over the field of view of interest. The signals from the wavefront sensors are recombined and applied to several deformable mirrors optically conjugated to different altitudes in the atmosphere above the telescope.

from the whole field of view and it is possible in this way to tune the correction depending on the location in the field. A graphic representation of MCAO is given in Figure 2. From this concept of multiple conjugations comes the definition of MCAO. This differs substantially from the actual adaptive optics systems which have only one deformable mirror, typically conjugated to the pupil of the telescope at the altitude of a few metres in the atmosphere.

The atmospheric turbulence has a continuous vertical structure which induces a systematic error in the wavefront correction, due to the fact that, for technical reasons, the number of conjugation altitudes at which the deformable mirrors can be placed is limited. What in practice is done for an MCAO system is to optimise the correction to be given to each deformable mirror in order to minimise the uncorrected turbulence, both along the vertical of the telescope and in the scientific field of view.

The wavefront sensing concept presented here is called Star Oriented and it is based on using as many wavefront sensors as guide stars. MAD is actually equipped with a Star Oriented wavefront sensor and it has been used to perform the first two demonstration runs of 2007. All the results presented have been obtained with the Star Oriented wavefront sensor.

As mentioned before MAD will be equipped with a second wavefront sensor, called Layer Oriented, which will have first light during the third MAD demonstration run planned for September 2007. This wavefront sensor, based on a pyramidal optical component, works with a completely new concept, which allows sensing all the guide stars simultaneously and uses as many detectors as deformable mirrors. In this way the quality of the signal from the guide stars is improved by co-adding the light on the same detector; but the complexity does not scale as the first order with the number of guide stars used. A detailed description of the Layer Oriented concept is given in Ragazzoni, Farinato and Marchetti (2000).

The MAD system

The full MAD system with the exceptions of the CAMCAO infrared imaging camera, the instrument control software and the Layer Oriented wavefront sensor has been fully designed and built by ESO in Garching. The MAD system has been optimised for providing the best correction in *K*-band (2.2 μm) and all the performance has been evaluated at this wavelength.

The main strategy we have followed has been to reuse as much as possible existing hardware and software components developed in the framework of the other ESO adaptive optics projects. We also decided to follow rigorously the ESO standards in matters of instrumentation,

being fully compliant with the installation of new instruments at the VLT.

Despite the prototype nature of MAD, the full project underwent the ESO review procedure before the initiation of the procurement and construction of the main hardware components. MAD passed the Conceptual and the Final Design Reviews, as well as the Preliminary Acceptance for Europe, just before the shipment to Paranal to evaluate the compliance with VLT Paranal standards for instrument installation and operation.

The MAD optical bench consists of a static table supported by a structure which elevates the main optical axis to the level of the one from the VLT on the Nasmyth platform. The light from the 2-arcminute field of view coming from the telescope enters MAD through an optical derotator which compensates for the field rotation affecting the images at the Nasmyth focus. After a collimator lens there are the two deformable mirrors, the first one conjugated at 8.5 km above the telescope and the second at the telescope pupil (see Figure 3). Both deformable mirrors are spare units of the ones used in the MACAO family adaptive optics systems installed at the VLT (60-element bimorph mirrors). The pupil-conjugated deformable mirror is supported by a fast steering mount to assist the mirror in compensating for the largest contribution of the atmospheric tip-tilt. This mirror is also a spare unit from the MACAO systems. A dichroic allows reflection of the visible part of the light in the direction of the wavefront sensor. The infrared light is transmitted and folded down through a hole in the bench, below which is located the infrared imaging camera. CAMCAO is based on a Hawaii2 2k × 2k detector driven by an ESO IRACE control system; the pixel size projected on the sky is 0.028 arcseconds for a total field of view of ~ 57 arcseconds. A scanning table allows CAMCAO to patrol the full 2-arcminute field of view, while keeping the adaptive optics loop closed and without the need to offset the telescope or move other optical components into the light path. CAMCAO is equipped with standard *J*, *H*, *Ks* filters plus some narrowband ones.

The Star Oriented wavefront sensor is based on three Shack-Hartmann sensors of 8 × 8 sub-apertures each, which are able to scan the full 2-arcminute field of view to easily pick up the light of the guide stars. The wavefront sensor detectors are commercial E2V CCD39 units, 80 × 80 pixels, a device commonly used in existing adaptive optics systems, and driven by an ESO FIERA control system. In proximity to the wavefront sensor is located the acquisition camera, based on the standard ESO new technical CCD and its related controller; the camera images the 2-arcminute field of view in order to locate the exact position of the guide stars. During operation an interactive procedure allows correct centring of each Shack-Hartmann on the desired guide stars, using only the image from the acquisition camera. Finally two movable units, supporting illuminated fibres, can be inserted into the optical beam for instrument calibration and testing.

The MAD real-time computer provides acquisition from the wavefront sensor, wavefront reconstruction and deformable mirror actuation up to a frequency of 400 Hz with no detector binning, and up to 640 Hz in 2 × 2 binning mode. At each loop cycle 312 slopes are received and multiplied by the reconstruction matrix. In total MAD controls 122 real-time channels, 38 movable functions, and 5 detectors simultaneously through six dedicated Local Control Units located in four electronics cabinets.

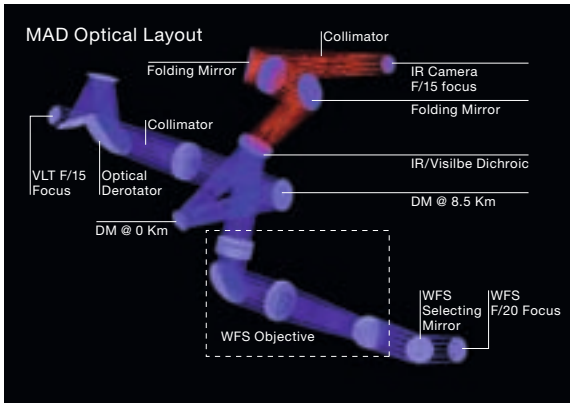

Figure 3: MAD optical layout. The input beam from the VLT is folded by the deformable mirrors and split by the dichroic. The visible light is sent to the wavefront sensor while the infrared light feeds the CAMCAO camera located below the MAD bench.

MAD installation and first light

MAD was first integrated in the optical laboratory at ESO Garching where the MAD team performed extensive system tests, lasting more than one year, before the shipment to Paranal. During the tests we characterised the performance of the system under different correction configurations, including a long phase of debugging during which we implemented the useful corrective actions to optimise both the performance and the operability of the system. A dedicated facility to emulate a three-dimensional, time-evolving atmosphere and variable configuration of guide stars, called MAPS, was placed at the MAD entrance window and used during the full testing period.

In December 2006 MAD successfully passed the Preliminary Acceptance Europe and in January 2007 it was dismounted and shipped to Paranal. The system reintegration at the VLT visitor focus located at the Nasmyth platform A of UT3 Melipal started around mid-February and lasted for about one month. In this period around 15 people, including Paranal staff, participated in the MAD installation which was completed without major problems. In the second half of March we spent about two weeks in fully characterising and calibrating the system following the procedures established the year before during the laboratory system testing.

Finally in the evening of 25 March, after concluding some software functional tests, we pointed at NGC 3293, a bright open cluster, selected three suitable guide stars and successfully closed the MCAO loop.

From the beginning we realised that the system was stable and reliable, a condition which lasted for the whole demonstration run. The run consisted of a mix of

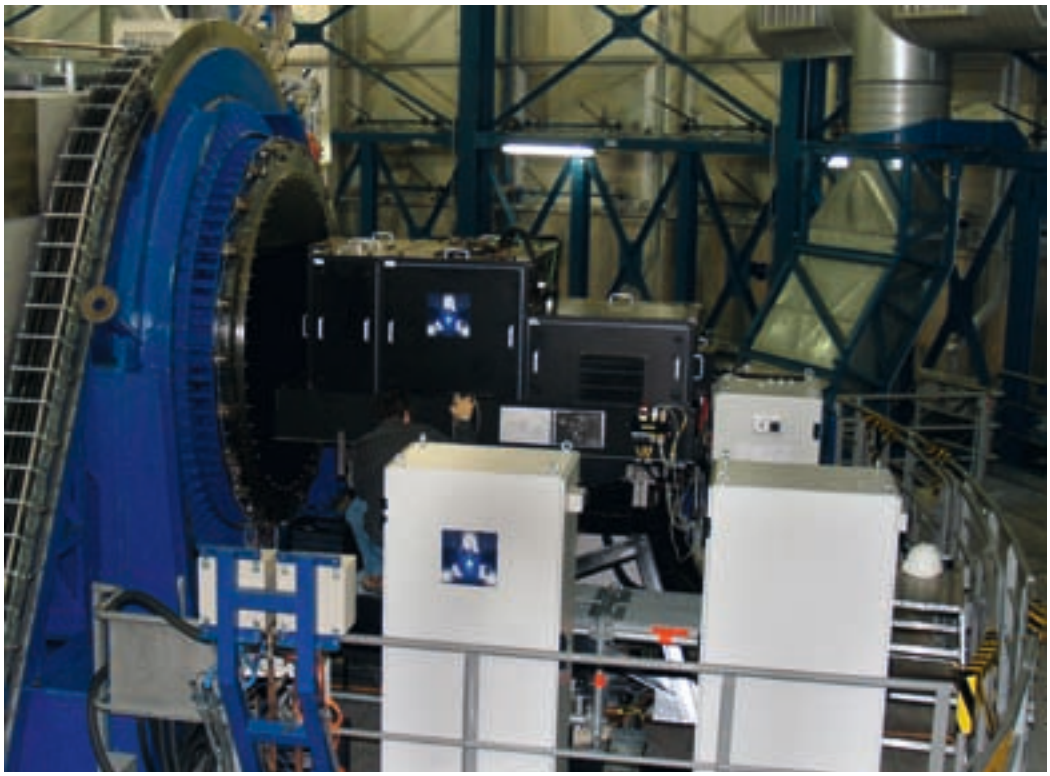

Figure 4: MAD installed at the Nasmyth visitor focus of UT3 Melipal.

half and full nights for a total of 8.5 effective nights spread over 12 nights. This long period, originally not planned, had two positive aspects: it increased the chances of having good seeing; it permitted collection of statistics on seeing, thus allowing estimation of the MAD performance under different conditions.

On-sky results

The main target selected for the correction performance evaluation was Omega Centauri, the brightest globular cluster visible from Earth. Omega Centauri offers several relatively bright guide stars suitable for wavefront sensing and it is extremely crowded, allowing an efficient mapping of the correction quality over the whole field of view.

In Figure 5 is shown a typical example of the correction performance for a 2-arcminute field under good seeing conditions (~0.7 arcseconds as given by the DIMM monitor). Three guide stars of V magnitude ~ 11.5 were used, equally spaced and located on a circle of approximately 100 arcseconds diameter. The maps shown represent the Strehl ratio distribution in *K*-band (2.2 μm) in the field with three different correction modes: classical adaptive optics, that is, sensing and correcting for a single star in the field; Ground Layer adaptive optics; and MCAO.

Figure 5: Strehl ratio maps (in % at 2.2 μm) for classical (left), Ground Layer (middle) and Multi-Conjugate (right) Adaptive Optics. The useful corrected field of view for classical adaptive optics is reduced to 20 arcseconds. In GLAO it enlarges reaching the best performance at the centre. In MCAO the performance is much better with peaks on the guide stars and a valley at the centre of the field of view.

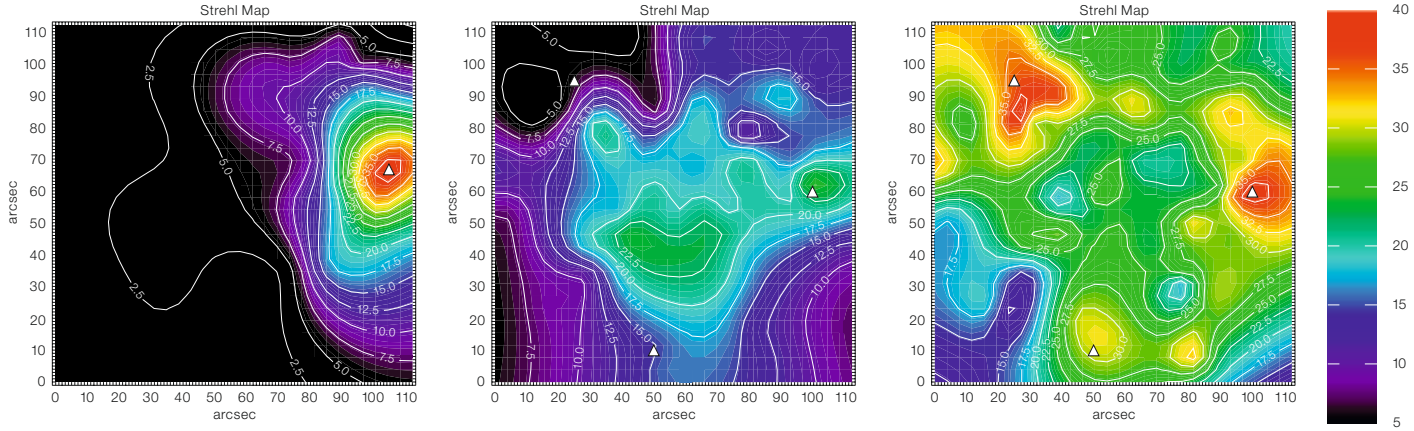

The Ground Layer Adaptive Optics (GLAO) is a special case of MCAO when the guide stars sensed are the same but only one deformable mirror, conjugated at the telescope pupil, is used for correction. This technique does not achieve the peak Strehl ratio of MCAO, but it can guarantee a moderate improvement in the concentration of the light for the observed objects and is a simpler technical implementation. The second-generation VLT instruments MUSE and HAWK-I will be fed by GLAO modules, which justifies its study in the framework of MAD.

The advantage of MCAO with respect to classical adaptive optics is fairly clear: for the latter the well-corrected area (Strehl ratio above 20 %) will not extend more than 20 arcseconds from the guide star; for MCAO almost the full 2-arcminute field of view benefits from such a Strehl ratio improvement. Another typical behaviour of MCAO is also evident: the correction is effective inside the polygon identified by the guide stars, with maxima located on those stars and a 'valley' at the centre, but it quickly drops in the outer regions of the field of view.

For GLAO the correction behaviour is the opposite: the performance peak is at the centre of the field of view and drops outwards. The absolute Strehl ratio values for GLAO are not much smaller than the ones for MCAO at the field of view centre while MCAO is clearly superior for all the rest of the field. As a comparison, GLAO had higher performance than in the laboratory testing, while MCAO performed as expected. Our explanation of this is that some obvious technical limitations, imposed by the laboratory atmospheric model (with a few discrete turbulence layers), do not match the situation on the sky (continuous turbulent structure). This difference penalised the performance estimation for GLAO.

During the observing runs, continuous real-time data have been collected from the atmospheric seeing monitors DIMM (seeing, coherence time) and MASS (atmospheric turbulence vertical profile) for cross-correlating the MAD correction performance with the instantaneous atmospheric turbulence conditions. A detailed analysis has shown that both MCAO and GLAO exhibit the expected performance, weakening with the worsening of the seeing, with MCAO dropping slower than GLAO. MCAO proved also to be much more robust when atmospheric turbulence tends to concentrate at higher altitudes. This trend is expected since GLAO corrects mainly the ground atmospheric layer and the effectiveness of the correction depends strongly on the relative strength of the ground layer. On the other hand, MCAO benefits from the deformable mirror conjugated to the upper layer and compensates more efficiently for the high-altitude atmospheric turbulence. The same trend can be observed when considering the correction uniformity across the field of view. MCAO is more uniform than GLAO in terms of the standard deviation of the Full Width at Half Maximum of image size over the field of view, while for both correction modes the uniformity improves with the seeing conditions.

A very impressive example of the gain provided by MCAO is demonstrated in Figure 6, where the open loop and the MCAO closed loop *K*-band images for the same region of 20 × 20 arcseconds near the centre of Omega Centauri are shown. The open-loop image has been obtained with ISAAC and the stars have a Full Width at Half Maximum of 0.6 arcseconds. The MCAO closed-loop image has been obtained with MAD using three guide stars of V magnitude ~ 11.5 on a circle of 2 arcminutes in diameter. The 20 × 20 arcseconds region is at the centre of this circle, that is, the closest guide star is at ~ 1 arcminute distance. The gain in angular resolution is enormous and allows very close and faint stars in the cluster to be distinguished. The MCAO image was obtained with 0.7 arcsecond seeing and the Full Width at Half Maximum of the star images ranges from 0.087 to 0.107 arcseconds, with an average of 0.098 arcseconds. The light concentration is significant since on average 56 % of the light from a star is included in 3 × 3 pixels (0.084 arcseconds). For a total integration time of 600 seconds the measured limiting magnitude is K ~ 20.5 (3σ), which makes this the deepest ever image in *K*-band of this globular cluster and permits significant increase in the observable population of the cluster's main sequence.

Figure 7 shows a 1 × 1 arcminute MCAO corrected *K*-band image centred on the well-known Trapezium cluster, a massive star-formation region in the constellation of Orion. For this image three guide stars of V magnitude ~ 10 to 12 have been

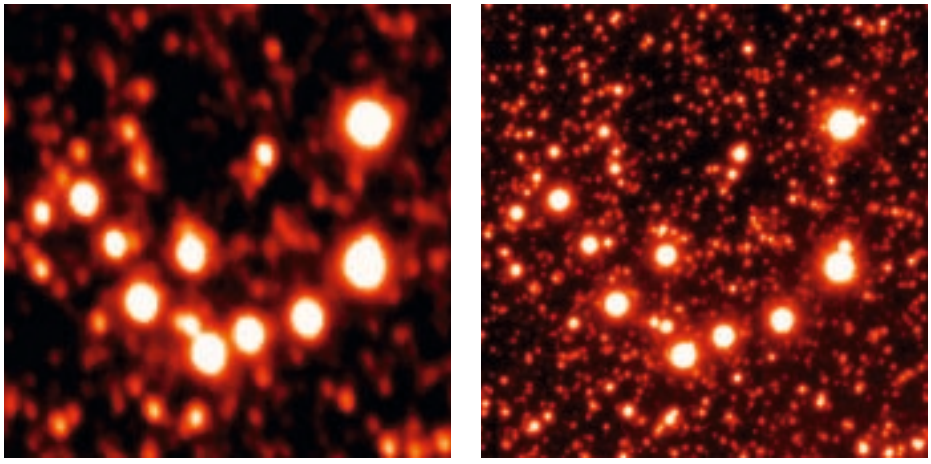

Figure 6: 20 × 20 arcseconds region nearby the centre of the globular cluster Omega Centauri. The image on the left was obtained in *K*-band by ISAAC and has an average FWHM of 0.6 arcseconds. The right-hand image was obtained at the same wavelength by MAD with MCAO correction. In the latter case the FWHM is often below 0.1 arcsecond, a remarkable value taking into accont that the closest guide star is ~ 1 arcmin away. The angular resolution improvement is dramatic and allows very close and faint stars to be distinguished. The limiting magnitude in K is ~ 20.5.

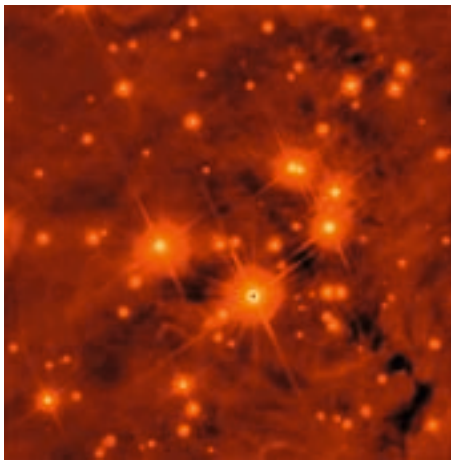

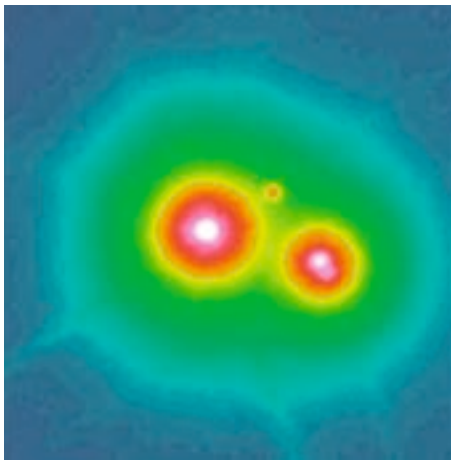

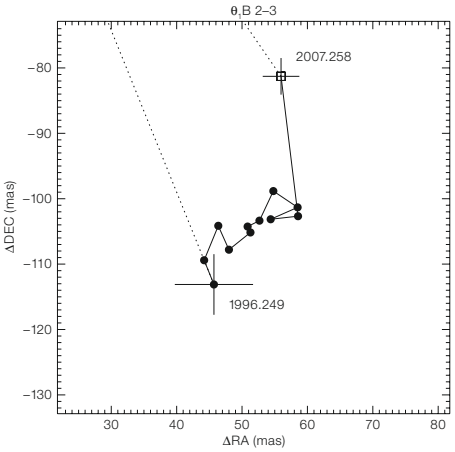

Figure 7: Left: 1 × 1 arcminute *K*-band MAD image of the region of the Orion Trapezium (north up, east left). The FWHM is ~ 0.1 arcseconds varying slightly across the field. It is possible to distinguish several protoplanetary discs as well as identify close binaries. **Centre:** Close-up view of the multiple system θ^1 Orionis B, the northernmost component of the five bright stars of the Trapezium group. The four brightest companions are clearly resolved. **Right**: Orbital evolution since 1996 for components 2 and 3 (the two rightmost ones) of θ^1 Orionis B; the latest point is the one measured from MAD images. For previous measurements see the Fourth Catalog of Interefero-metric Measurements of Binary Stars (Hartkopf et al. 2001 and *http://ad.usno.navy.mil/wds/int4.html*).

selected in a quite non symmetric configuration. The seeing at the moment of the exposure was 1.2 arcseconds (DIMM monitor) and, despite the non-optimal configuration of the guide stars, the Full Width at Half Maximum of the objects in the corrected image ranges from 0.090 to 0.120 arcseconds, with an average of 0.100 arcseconds. The limiting magnitude is K ~ 19 for an exposure time of 300 seconds.

This example shows another great potential of MCAO, that is the field of view multiplexing for imaging a large portion of the sky with very high angular resolution. In the image it is possible to identify simultaneously several protoplanetary structures blown away by the stellar wind of the nearby stars. At the same time it is possible to distinguish several binary or multiple stars and measure their positions with very high accuracy. As an example, in Figure 7 is shown the orbital evolution for the components 2 and 3 of the multiple system θ^1 Orionis B, consisting of at least five stars mutually orbiting around each other. The position measured with MAD together with the ones previously obtained, both with adaptive optics and speckle interferometry, range over a total span of 11 years and show a clear trend in motion suggesting a very long-period orbit.

The scientific data obtained during the first demonstration run have been released to the community and are accessible to anybody interested in looking in more detail at the capabilities of such a technique (see *http://www.eso.org/projects/aot/mad/commdata/*).

Owing to the success of the MAD experiment, ESO decided to grant two science demonstration runs of one week each and has released a call for proposals to the scientific community to exploit the science capabilities of the prototype before the final dismounting from the VLT. The science demonstration runs will take place in November 2007 and January 2008.

After the completion of the second run MAD will be dismounted and shipped back to Garching for reintegration. The system will then be available to any research group interested in performing further and more detailed tests in view of future applications.

The future of MCAO

The scientific impact of MCAO has been recognised to be valuable both for Galactic and extragalactic astrophysics. The capability to add Laser Guide Stars as sources for wavefront sensing will improve the sky coverage for astronomical objects, enhancing the potential of this technique. The first laser guide star based MCAO instrument will have first light in 2008 at the Gemini Observatory, and quite likely its example will be followed by other large telescopes.

In the case of the E-ELT, the MCAO facility has been recognised as a primary instrument and the related Phase A design has already started in the framework of a larger study of E-ELT instrumentation.

References

Beckers J. M. 1988, in ESO conference "Very Large Telescopes and their instrumentation", ed. M.-H. Hulrich, 693
Gilmozzi R. and Spyromilio J. 2007, The Messenger 127, 11
Hartkopf W. I., McAlister H. A. and Mason B. D. 2001, AJ 122, 3480
Marchetti E. et al. 2006, SPIE 6272, 21M
Ragazzoni R., Marchetti E. and Rigaut F. 1999, A&A 342, L53
Ragazzoni R., Marchetti E. and Valente G. 2000, Nature 403, 54
Ragazzoni R., Farinato J. and Marchetti E. 2000, SPIE 4007, 1076
Vernet-Viard E. et al. 2005, Opt. Eng. 44, 6601

Circular Polarimetry Now Offered at EFOSC2

Ivo Saviane[1]
Vilppu Piirola[2,5]
Stefano Bagnulo[3]
Lorenzo Monaco[1]
Damien Hutsemekers[4]
Seppo Katajainen[2]
Harry Lehto[2]
Tommi Vornanen[2]
Andrei Berdyugin[2]
Pasi Hakala[2]

[1] ESO
[2] Tuorla Observatory, University of Turku Piikkiö, Finland
[3] Armagh Observatory, Armagh, Northern Ireland
[4] University of Liège, Belgium
[5] Vatican Observatory, Città del Vaticano, Rome, Italy

Starting from period P79, circular polarimetry measurements can be carried out with EFOSC2 at the ESO 3.6-m telescope. Here we describe the motivations behind the upgrade of the instrument, and a few results from the commissioning runs are used to show the excellent performance of the new polarimetry unit.

Reasons for having the new EFOSC2 mode

Polarisation originates whenever any kind of anisotropy occurs in the radiative source, e.g., scattering by matter, presence of collimated beams of particles, presence of a magnetic field, and so forth. Thus it occurs in many different physical processes of emission of photons, and in many different kinds of astrophysical objects. Therefore, instruments offering imaging and/or spectro-polarimetry are of interest to a broad astronomical audience. Indeed there has been a recent increase in the pressure on the polarimetric modes of both FORS1 at the VLT and EFOSC2 at the ESO 3.6-m telescopes. Just in the two ESO periods P77 and P78, about 1/3 of the EFOSC2 proposals asked for the polarimetric mode, and the subjects ranged from Solar System objects (comets and Near-Earth Objects), to planets and dust in nearby stars, to stars in the Galaxy and the Magellanic Clouds (magnetic cataclysmic variables (CV), asymptotic giant branch (AGB) stars, magnetic white dwarf (WD) stars, Galactic super star clusters), to active galaxies (Seyfert, active galactic nuclei (AGN), BL-Lacs), and interacting galaxies. The proposals came from seven countries (Finland, Switzerland, UK, Germany, Italy, Chile, and France), and ten institutes altogether (just counting the PIs). For this reason, more than one year ago it appeared that expanding the polarimetric capabilities of EFOSC2 would meet a substantial demand of the European astronomical community.

In April 2006 a proposal for a new polarimetric unit was then submitted to the Director of the La Silla Paranal Observatory, and it was accepted shortly afterwards. The proposal was to offer the possibility to measure circular polarimetry with EFOSC2 in addition to the available linear polarimetry. EFOSC2 has a couple of advantages compared to FORS1. First, recently we have been able to offer fast imaging polarimetry of point sources, reaching a sample rate of 12 sec (plus exposure time), thanks to the possibility to read only a corner of the CCD, and to the faster retarder plate rotation. This is an essential requirement for example in the case of 'intermediate polar' cataclysmic variables, since circular polarisation originates close to the shock region near the surface of the fast spinning WD. In some cases significant variations can occur in a few minutes (e.g. GG Leo where circular polarisation rises from zero to +20% in about 10 minutes). Furthermore, longer observing runs are easier to obtain at La Silla, allowing monitoring programmes to be carried out. Note also that preliminary measurements have shown that the instrumental linear polarisation is less than 0.1% at field centre, and about 0.4% at the edge, while FORS1 has an instrument linear polarisation reaching 1.5% at the edges.

A copy of the current polarimetry unit was then built, to house a new quarter wavelength (λ/4) retarder plate in a safe way. This allows to easily exchange the two units, making operations relatively easy (see Figure 1). Exchanging the two units only requires a few minutes, and in terms of both control software and observing templates, the operation is completely transparent. The super-achromatic quarter wave retarder plate (of 50 mm diameter × 12 mm thickness) was purchased from Astropribor Kiev at a special price, due to some minor defects of the glass, which do not compromise the quality of the measurements. Having two mutually exclusive units means that linear and circular polarisation will have to be measured in two consecutive nights, if required, but this is not a concern for most scientific cases. If absolutely needed linear and circular polarisation can be measured simultaneously with the λ/4 plate (rotated in 22.5° steps), but then with only 50% efficiency for linear, and 70% efficiency for circular polarisation. The old and new units are displayed in Figure 1.

Commissioning and science verification

Due to the major problem with the dome of the 3.6-m telescope (see the article by Ihle et al. on page 18), which absorbed most of the resources of the mechanical

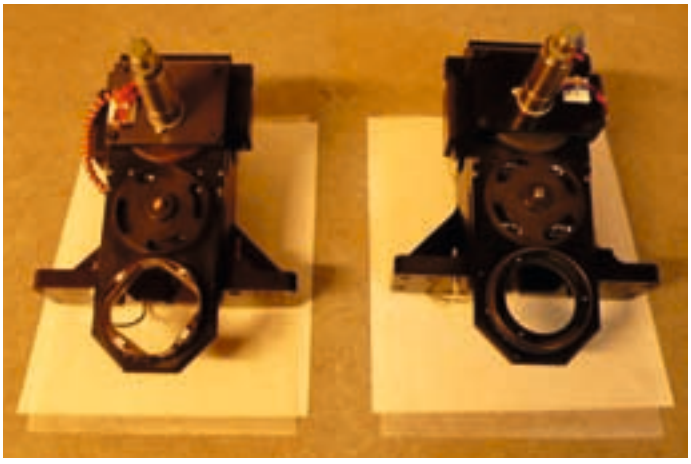

Figure 1: A photograph of the old (left) and new (right) polarimetry units.

workshop, the fabrication of the unit suffered a delay, and it was not ready at the very start of P79. So for the first commissioning, which was done in March, the observations were done with the λ/4 plate housed in the old unit. However the unit was ready for the second commissioning which happened in April, and just before the first visitor run. Several scientific and calibration targets were observed, and we illustrate here only a few cases. Results for another target observed in June are also included.

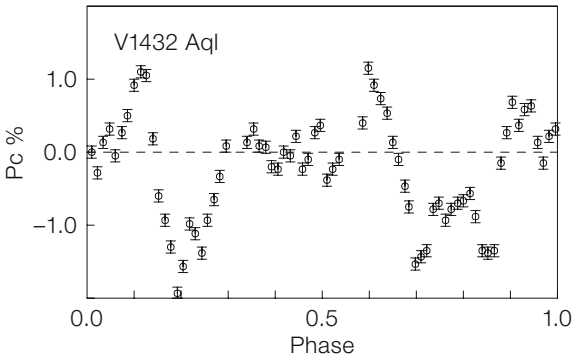

Figure 2: Circular polarisation curve over the WD spin period in the asynchronous polar V1432 Aql.

Polarimetry standards

During the second commissioning night on 17 April, several standard stars and science targets were observed. In particular imaging polarimetry in broadband filters (*BVRi*) was obtained for the magnetic WD LP790-29, and the data were analysed with the following result: V_B = 5.50 ± 0.07 %, V_V = 7.10 ± 0.05 %, V_R = 9.28 ± 0.04 %, V_i = 7.12 ± 0.06 %. This is consistent with West (1989), who measured V_B = 5 %, V_V = 6.5 % and V_R = 10 %. Another test was done by measuring Hiltner 652, a highly *linearly* polarised standard star. In this case we should measure null circular polarisation, and indeed V_V = 0.03 ± 0.03 % was computed. Hence we can conclude that the cross talk between linear-polarisation and circular polarisation is comfortably small. Finally the measurement of WD1615-154, an unpolarised standard, gives V_V = 0.03 ± 0.05 %, a result indeed consistent with zero polarisation.

As an additional test, LP790-29 was repeated with the retarder plate at slightly different angles with respect to the adopted reference, and it was found that a few degrees of difference do not have a significant impact on the measurements. During the first visitor night LP790-20 and WD1615-154 were observed again, obtaining consistent results: V_V = 7.07 ± 0.09 % for LP790-29 and V_V = 0.00 ± 0.04 % for WD1615-154. The linear-circular polarisation cross-talk was checked again with the highly linearly polarised standards Vela 1 95 and HD 155197, with results V_V = +0.03 ± 0.05 % and V_V = +0.03 ± 0.04 %. Again this is consistent with zero circular polarisation.

Circular polarimetry of the asynchronous polar V1432 Aql

Polars (AM Her objects) are a subclass of magnetic cataclysmic variables (mCVs) and consist of a highly magnetic (B = 10–200 MG) WD accreting matter from a low-mass companion. The WD rotates synchronously (or nearly so) with the orbital motion. The strong field of the WD prevents the formation of an accretion disc. Instead, the matter is channelled along the field lines, and flows onto the WD surface through accretion columns (see e.g. Cropper 1990, for a review). The temperature of the accretion shock is T_e ~ 10–40 keV, and the mildly relativistic electrons of the hot magnetised plasma emit strongly polarised cyclotron radiation in the optical and near-infrared.

Asynchronous polars are important to understand better the magnetic braking mechanism, which re-synchronises the WD with the orbital motion very rapidly (T_s < 100–1 000 yr) after nova eruptions (e.g. V1500 Cyg, BY Cam, V1432 Aql). An especially interesting system is V1432 Aql (see e.g. Staubert et al. 2003; Rana et al. 2005; Andronov et al. 2006). It is unique among asynchronous polars in the sense that the white dwarf spin period is about 0.3 % *longer* than the binary orbital cycle. This is against the earlier plausible explanation that synchronism in polars is broken by transfer of a small amount of orbital angular momentum during the common-envelope phase of a nova eruption, which should *speed up* the WD spin, as seen e.g. in V1500 Cyg = Nova Cygni 1975 (Schmidt, Liebert and Stockman 1995). Another possible mechanism is rotational braking of the white dwarf during the mass-loss phase by the strong magnetic field. The triple-hump profile seen in the *XMM-Newton* and the *ASCA* light curves requires *three* hot spots on the surface of the white dwarf (Rana et al. 2005). These peculiarities make V1432 Aql an important object for further study.

Circular spectro-polarimetry of V1432 was carried out with EFOSC2 on 28 June 2007. Figure 2 shows the variations of broadband optical circular polarisation over the 3.4 hr spin period of the WD. Fast excursions of positive (right handed) and negative circular polarisation are seen, as the visibility of the cyclotron emission regions on the spinning WD, and the angle between our line of sight and the magnetic field lines, change. The shape of the circular polarisation curves suggest that there are two negative poles dominating during these observations, and the field lines at the cyclotron emission region are significantly inclined with respect of the normal to the WD, i.e., accretion takes place onto the WD relatively far from the magnetic poles. The accretion geometry also changes during the 50-day beat period of the WD spin and orbital periods. These results demonstrate that circular polarimetry is an efficient tool for probing the magnetic field and accretion geometry in mCVs, and that EFOSC2 can detect variations of circular polarisation of the order of 0.1 % or less.

Spectro-polarimetry of the magnetic WD G99-37

For the science verification, a number of targets were selected with known circular polarisation properties. One of the most interesting objects is the DGp WD G99-37. Circular polarisation in the optical continuum due to a strong magnetic field was discovered by Landstreet and Angel

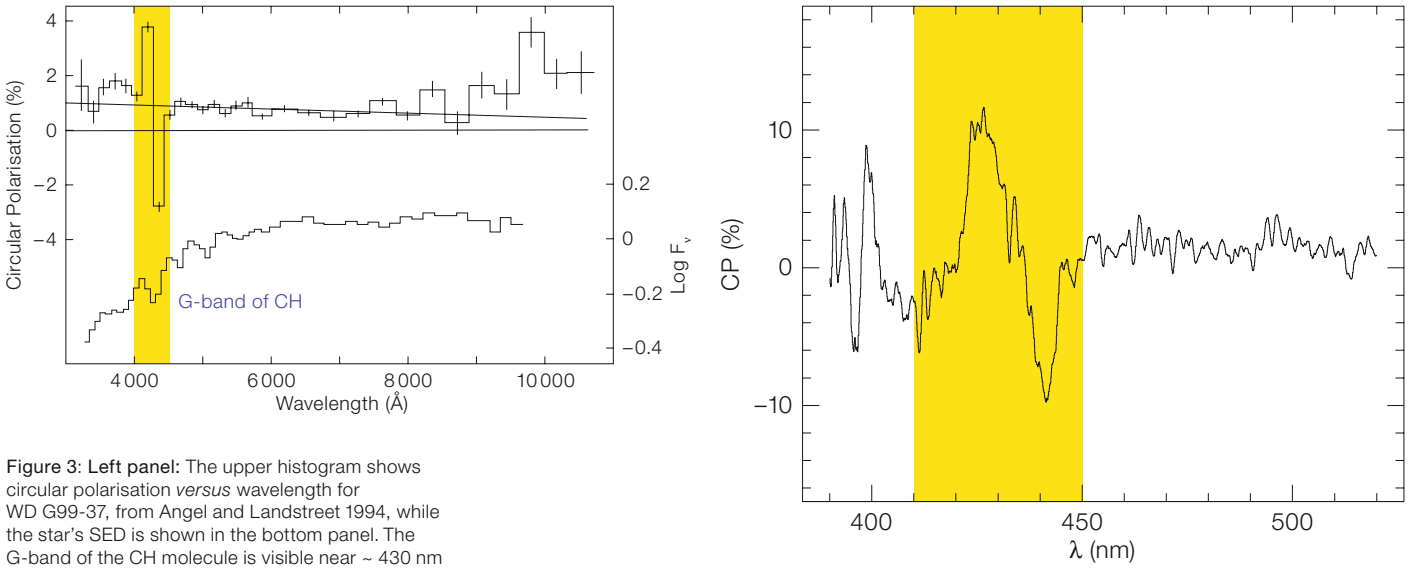

Figure 3: Left panel: The upper histogram shows circular polarisation *versus* wavelength for WD G99-37, from Angel and Landstreet 1994, while the star's SED is shown in the bottom panel. The G-band of the CH molecule is visible near ~ 430 nm in the SED, and its polarisation structure is evident in the upper histogram. **Right panel:** the polarisation spectrum of the same star as measured with the new EFOSC2 unit. In both panels the G-band is highlighted by the yellow shaded area.

(1971), and later Angel and Landstreet (1974) measured a field strength of 3.6×10^6 Gauss, using the Zeeman effect on the absorption G-band of CH at ~ 430 nm. The effect on the circular polarisation spectrum is shown in Figure 3 (left panel), and it can be qualitatively understoodby looking at Figure 1 in Landstreet (1980) and the inset in Bagnulo et al. (2001). A magnetic field parallel to the line of sight splits the band into two components symmetric with respect to the central wavelength, and the two components are circularly polarised in opposite directions. So if the magnetic field was purely longitudinal, the absorption band would appear bluer than the central wavelength in left-polarised light, and redder in right-polarised light. As polarimetry measures the ratio $(I_L - I_R) / I$, where I_L and I_R are the intensities of the left- and right- polarised light, the spectrum of circular polarisation will show the rapid change across the G-band which is seen in Figure 3. This polarised absorption feature, at the wavelength range 0.42–0.44 nm, peaks from +10 % to −10 %, so it is relatively easy to measure.

The star was observed with EFOSC2 on the night of 16 March. Briefly, eight 15-min spectra were taken with the 20″ Wollaston prism and the quarter wave retarder plate scanning the angle sequence 135°–45°–45°–135°–135°–45°–45°–135°. The 1″ slit was used, together with grism #7, which allows to cover the range ~ 330 nm to ~ 520 nm at 0.2 nm px^{-1} dispersion. The data reduction was carried out using standard IRAF reduction packages for extracting the two polar-ised spectra from each exposure, and our own routines to calculate the degree of circular polarisation from the exposures made at the two orientations of the quarter-wave plate.

The resulting spectrum of the circular polarisation (CP) is shown in Figure 3 (right panel), and the CP structure induced by the magnetic field across the CH band at 415–440 nm can be clearly seen. This demonstrates that useful measurements of this star were obtained, and that we recovered the ~ ± 10 % maximum values of the CP.

Spectro-polarimetry of HD 94660

HD 94660 is a well-known chemically peculiar star that shows an almost constant longitudinal magnetic field of about −2 kG. This star has been repeatedly observed with FORS1 in polarimetric mode during various surveys of magnetic fields to check the instrument behaviour (see Bagnulo et al. 2001). We observed HD 94660 with EFOSC2, and measured the mean longitudinal field via formula (1) of Bagnulo et al. (2001). The result is $\langle B_z \rangle = -2\,105 \pm 80$ G (see Figure 4) which is fully consistent with the values measured during the last few years with FORS1 at the VLT (see Bagnulo et al. 2006).

Acknowledgements

We thank the La Silla Engineering Department (and in particular Gerardo Ihle and Juan Carlos Pineda) and the SciOps engineer Emilio Barrios for their dedication to this project, that has made it a reality.

References

Andronov I. L., Baklanov A. V. and Burwitz V. 2006, A&A 452, 941
Angel J. R. P. and Landstreet J. D. 1974, ApJ 191, 457
Bagnulo S. et al. 2001, The Messenger 104, 32
Bagnulo S. et al. 2006, A&A 450, 777
Cropper M. 1990, Space Sci. Rev. 54, 195
Landstreet J. D. and Angel J. R. P. 1971, ApJ 165, L67
Landstreet J. D. 1980, AJ 85, 611
Rana V. R. et al. 2005, ApJ 625, 351
Schmidt G. D., Liebert J. and Stockman H. S. 1995, ApJ 441, 414
Staubert R. et al. 2003, A&A 407, 987
West S. C. 1989, ApJ 345, 511

Figure 4: The left panels show the Stokes I spectrum of HD 94660 (top left panel) and the Stokes *V* normalised to the intensity (bottom left panel), in the spectral region from *Hγ* down to almost the Balmer jump. All Balmer lines show a well-detected signal of circular polarisation, and what appers as noise in between the various Balmer lines is in fact mostly a polarisation signal coming from hundreds of metal lines not fully resolved by the instrument. The right panel shows how the magnetic field is calculated. For a longitudinal field, the circular polarisation depends linearly on the expression given in the abscissa. The angular coefficient is the mean field, so a linear regression of the spectro-polarimetric data allows to compute $\langle B_z \rangle \simeq -2000$ Gaus.

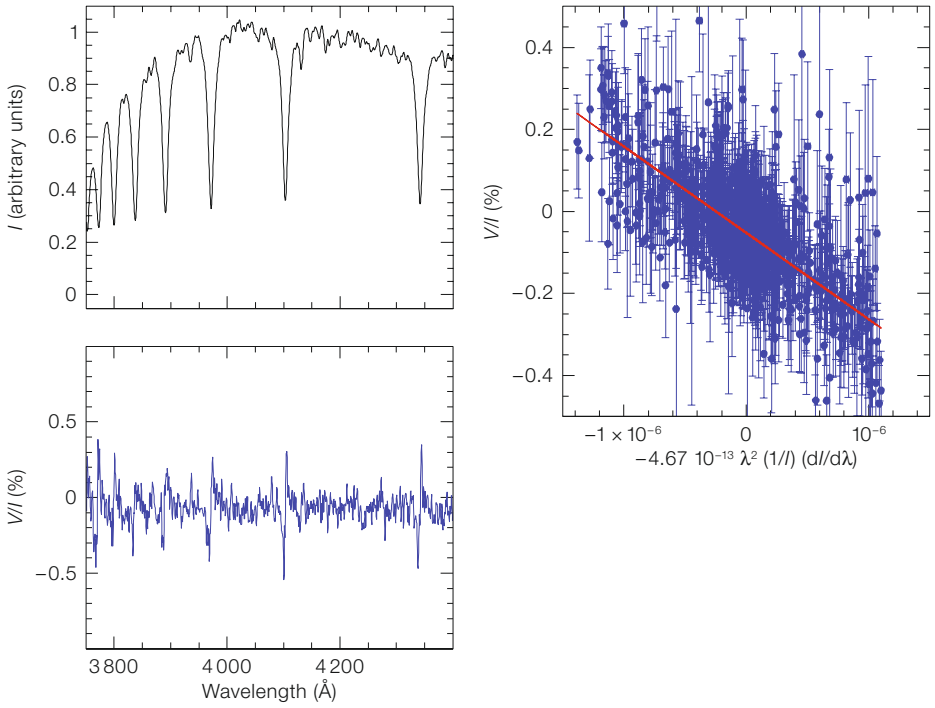

Photo: H. H. Heyer, ESO

Maintenance work on the dome shutter of the ESO 3.6-m telescope. Below in the distance can be seen the SEST telescope, which is no longer in active use (photograph from 1996).

The 3.6-m Dome: 30 Years After

Gerardo Ihle, Nelson Montano, Roberto Tamai (all ESO)

After rotating for more than 30 years, the dome support wheels for the ESO 3.6-m telescope started to degrade, resulting in a shutdown in October 2006. The engineering process of reshaping the track and gradual replacement of the supporting wheels is described. The rotation of the dome is now returning to its original efficiency.

Figure 1: The 3.6-m dome at La Silla pictured during unusual weather.

Figure 2: One of the original dome bogies, with the large centred wheel and rubber rim, is shown.

It is more than 30 years since the 3.6-m telescope (Figure 1) saw first light and the dome started to turn. Through all these years this telescope has been a flagship of La Silla and a continuous source of scientific return. The heavy structure, based on 'classical' telescope and dome construction, has continued to operate with minimum interruption due to significant failures.

The rotating part of the dome is a steel structure, built by Krupp, with an estimated weight of 350 tons. Thirty wheels support the dome as it turns on a rail fixed on top of the concrete part of the building. The movement is controlled by two sets of friction wheels that allow the dome to move during pre-setting and tracking, or simply positioning.

But after all these years the dome rotating part began to feel the test of time. Seven years ago the failures of the supporting wheels occurred, requiring the change of these units.

In 1999 we started the search for a provider who could help in the repair of the damaged wheels, but without success. The company that made these wheels for Krupp had disappeared. We could not find any European provider who, taking into account the Europe-La Silla time and space separation, was willing to produce the right rubber component for us, within reasonable costs.

The supporting wheels are built with a central mass used to house the bearings and the axis that fixes the wheel to the support unit or bogie (see Figure 2). A cast rim is used as the rail rolling contact surface and between these two metallic parts a compound rubber vulcanised layer joins them, providing the elastic part of the structure (see the sketch in Figure 3). Two lateral wheels centre the dome while it is turning (white in Figure 2).

The quest of finding the right rubber for replacement was not easy as the information was no longer available from the as-built configuration and the characteristics of the rubber were difficult to obtain from a degraded compound. Only after extensive investigation did we reach a company from the Weir Minerals group, called VULCO, that produces spare parts or special products for mines in Chile. They were willing to find the right compound, but this proved not to be an easy task. Many wheels were tried, a lot of water flowed under the bridge, but the problem still remained.

A serious problem triggered the shutdown at the beginning of October 2006, when a chain reaction of failures rendered the dome impossible to move. Interventions to overcome the problem proved unsuccessful; the solution required a decision to stop the dome for a long period.

The wheel rims had completely lost their shape (in terms of angle, concentricity with the axis, deformation of the rolling surface, etc.), but so also had the rail lost its top flat surface. The rails had built up an inverted V shape section (see sketch in Figure 4, right). In addition the rail was

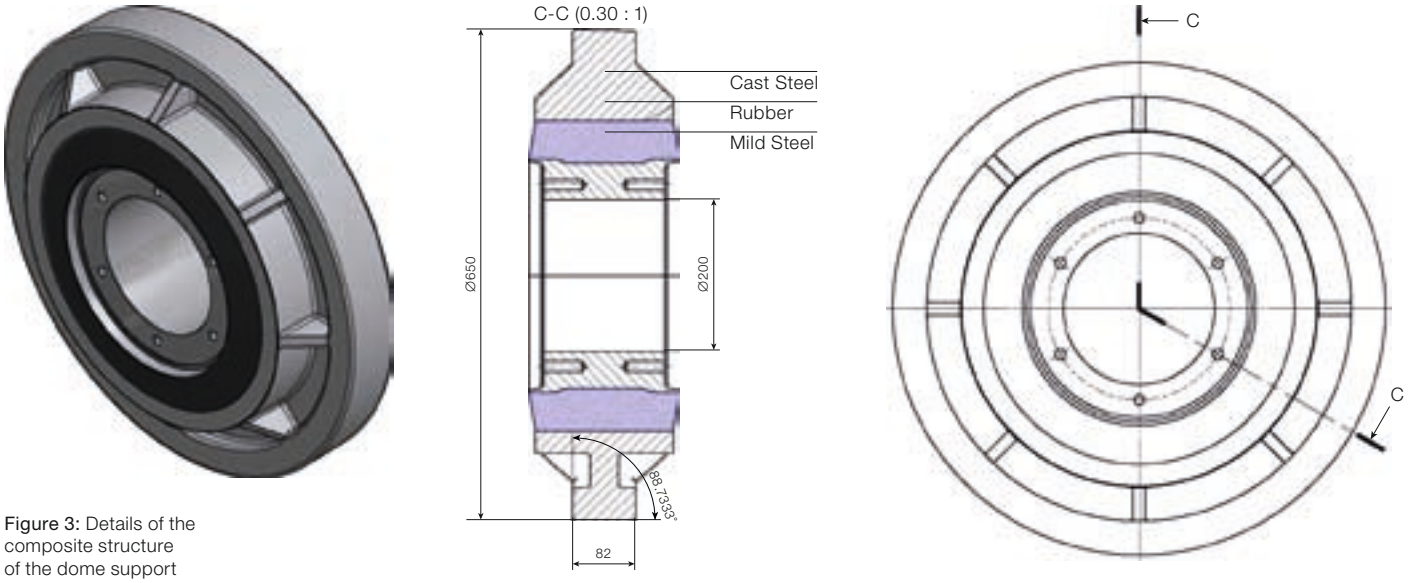

Figure 3: Details of the composite structure of the dome support wheels.

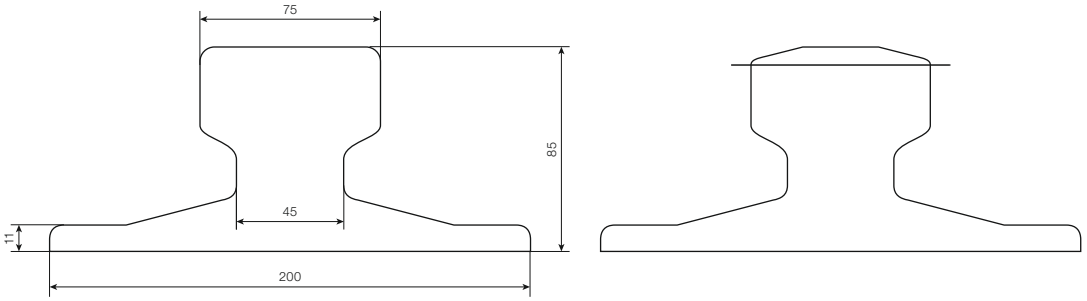

Rail type A75

Rail top shape before machining of 1.5 to 1.8 mm

Figure 4: Shown left is the original profile of the support rail, and, right, the rail profile after 30 years of use. The rail top was machined 1.5 to 1.8 mm to restore the profile (shown by the line in the right figure).

not flat on a plane but showed hills and valleys around its perimeter.

The condition of the wheels and the rail resulted in unacceptable force during rolling of the wheels, creating excessive stresses in the rubber and rail system. The failure rate thus began to increase.

These conclusions were reached after a survey campaign of the rail and wheels, conducted with the cooperation of Maintenance and Engineering Departments of the La Silla Paranal Observatory. The close collaboration made possible a rescue plan to correct these problems.

First we had to make extensive measurements of the situation with a theodolite, then conduct a study of the situation of the rail with respect to the enclosure shape and relative dome positioning. Then the re-machining of the outer rim of the wheels to the right shape was done, together with the milling of the top surface of the rail (Figure 4, right) with the help of a specially designed milling head (shown in Figure 5) attached to the rotating part of the dome itself. The centring of the dome was performed by adjusting the two lateral wheels of each bogie. When this was not possible the bogies were re-positioned in order to have the wheels centred on top of the rail. All these activities took place in October 2006, and gave the first results by delivering the dome and telescope back to the community on 4 November.

After the unsuccessful attempts to find the proper rubber compound for the wheels, a more radical solution to the dome wheel problem was considered: the design and fabrication of entirely new wheel units. Figure 6 shows a cut-away design of one of the new wheel units. The construction is based on a double-wheel carriage supported by friction springs and with the possibility to measure, via load cells, the load applied in the respective bogie. This is an advantage with respect to the original design because it allows a constant control of the load along the rail track.

The new wheels have so far been installed in eight positions out of 30, and Figure 7 shows one of the installed

units. The loading has been recorded along the rail track and these wheels have helped to relax the loading on the other wheels and thus improve the load distribution of the dome onto the supporting rubber wheels.

After a long period working in a slow velocity mode, and after 109 rubber wheel replacements, the dome rotation returned to the nominal full rotational speed resulting in optimal utilisation of the observing night. It was concluded that a rubber compound with a Shore A hardness of 65 to 70 and a breaking modulus of 23–25 MPa was the most appropriate for these wheels and for their expected loading. At the end of this set of repairs, the dome is returning to the efficiency that the designers and constructors envisaged, and science on the 3.6-m telescope is benefitting.

Acknowledgements

The Maintenance and Engineering Departments of La Silla and Paranal made possible the return of the telescope to normal use with the minimum of effect on observations. The group of engineers and technicians of both sites in La Silla Paranal Observatory brought this project to a happy end.

Figure 5: The special milling head, fabricated to machine the rail, attached to the dome.

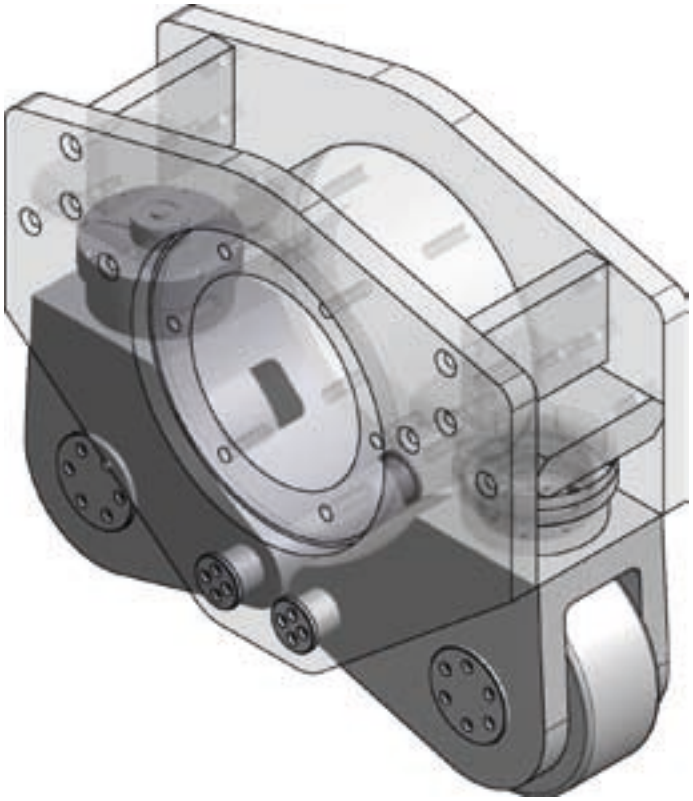

Figure 6: A cutaway showing the design of one of the new dome support wheel units.

Figure 7: One of the eight new wheel units is shown in position attached to the dome.

Calibration Sources for the Near-IR Arm of X-shooter

Florian Kerber, Francesco Saitta, Paul Bristow (all ESO)

We have studied the properties of wavelength calibration sources for the near-IR arm of X-shooter. In a novel approach we are combining laboratory measurements from a Fourier Transform Spectrometer (FTS), and literature data, with simulated data derived from a physical model of X-shooter. The sources studied are pen ray lamps filled with the noble gases Ne, Ar, Kr, and Xe and Th-Ar hollow cathode lamps. As a product we provide a quantitative order by order analysis of the expected properties of the calibration lamps during X-shooter operations. Based on these we give recommendations for the selection of the best combination of lamps. The combination of laboratory measurements and instrument modelling provides a powerful tool for future instrument development.

Intoduction to X-shooter

X-shooter is a single-target spectrograph for the Cassegrain focus of one of the VLT UTs, covering in a single exposure the spectral range from the *UV*- to the *K*-band (320–2500 nm). It is designed to maximise the sensitivity in this spectral range by splitting the incoming light into three arms – ultraviolet blue, visible and near-infrared (UVB, VIS and NIR) – with optimised optics, coatings, dispersive elements and detectors. X-shooter will be a unique instrument on 8-m-class telescopes in that it is capable of recording – over such a large wavelength range – the spectrum of an astronomical target in a single exposure. It operates at intermediate resolutions (R = 4 000–14 000, depending on wavelength and slit width) sufficient to address quantitatively a vast number of astrophysical applications, while working in a background-limited signal-to-noise regime in regions of the spectrum free from strong atmospheric emission and absorption lines. The instrument is currently undergoing subsystem assembly and commissioning is scheduled for 2008.

Wavelength calibration during X-shooter operations

X-shooter has a dedicated calibration unit providing light for flat fielding and wavelength calibration across the entire operating range of the instrument. For NIR wavelength calibration, the light of up to four pen ray lamps (Ne, Ar, Kr, Xe) is superimposed in the integrating sphere and the combined spectrum is fed to the spectrograph. The four pen ray lamps will be operated as a single source, that is all lamps, although using separate power supply units (PSUs), will be burning simultaneously and for the same length of time. Hence, the intrinsically different intensity levels of the lamps need to be balanced by the positioning of the lamps inside the integrating sphere and by shielding cylinders mounted around the lamps. We have studied the properties of pen ray lamps with a noble fill gas of Ne, Ar, Kr or Xe and Th-Ar hollow cathode lamps in order to provide a basis for the selection of the best lamp combination.

Wavelength calibration sources for X-shooter

In order to fully realise the scientific potential of X-shooter, excellent wavelength calibration across all three arms is essential. For UVB and VIS, Th-Ar hollow cathode lamps have been chosen as calibration sources following the successful operations of such lamps in e.g. FEROS, FLAMES, HARPS and UVES. For the NIR arm the situation is less obvious and we decided to conduct a dedicated programme to select the best combination of calibration sources for this wavelength region, which traditionally has relied on atmospheric features for wavelength calibration. Recently, ESO has gained significant experience with NIR wavelength standards in a collaboration with the US National Institute of Standards and Technology (NIST) as part of the CRIRES project (Kerber et al. 2007). Currently, there is no comprehensive database of emission line spectra of commercially available light sources. Based on experience, a combination of gas discharge lamps (Ne, Ar, Kr, Xe pen ray lamps) was envisaged. In addition we looked into the possibility of utilising a Th-Ar hollow cathode lamp – the calibration source for X-shooter UVB and VIS arms – also for the NIR arm.

Pen ray lamps

These lamps are called ‘Pencil’ lamps because of their size and shape. They are made of double bore quartz tubing with two electrodes at one end sealed into a handle. These lamps produce narrow, intense lines from the excitation of various rare gases and metal vapours. These commercial products are widely used for wavelength calibration of spectroscopic instruments such as monochromators, spectrographs, and spectral radiometers e.g. in industrial and chemical analysis applications. As input for our analysis, we used the line data available in the literature: Ne (Sansonetti, Blackwell and Saloman 2004); Ar (Whaling et al. 2002); Kr (Sansonetti and Greene 2007); and Xe (Saloman 2004).

Th-Ar hollow cathode lamps

Modern commercial hollow cathode lamps (HCLs) are sealed-off glass tubes that contain a metal cathode, a metal anode and a fill gas at a defined pressure. The lamp is operated by applying a voltage of a few hundred volts across cathode and anode. As a result, a discharge is formed in the low pressure (few hundred Pascal) fill gas and positive ions of the plasma are accelerated towards the cathode where they release matter through sputtering. As a result an HCL emits a rich spectrum of narrow emission lines from both the gas and metal atoms and ions in the plasma.

The Th spectrum was studied more than 20 years ago in the range from 278 nm to about 1000 nm at high resolution by Palmer and Engleman (1983). Its emission lines are very narrow and the spectrum is rich over a wide wavelength range. In nature Th has only one isotope, ^{232}Th, which has zero nuclear spin. Thus the use of Th for calibration lines avoids complex and asymmetric line profiles attributable to isotopic or hyperfine structure. Th-Ar HCLs are widely used for wavelength calibration of high-resolution spectrographs in the visual wavelength range,

including many examples at ESO such as FEROS, FLAMES, HARPS, and UVES. A detailed account of the properties, design and operations of HCLs is given in Kerber et al. (2007).

Two valuable studies (Hinkle et al. 2001; Engleman et al. 2003) of the Th-Ar spectrum in the near IR have recently been published, but neither is directly applicable to the operation of X-shooter. The spectrum of low current Th-Ar HCLs has been studied extensively at high spectral resolution by a collaboration of ESO and NIST for the ESO CRIRES spectrograph. X-shooter directly benefits from this experience.

Figure 1: The Fourier Transform Spectrometer in ESO's laboratory.

Laboratory measurements at ESO

ESO operates a commercial Fourier Transform Spectrometer (FTS) (model Thermo 5700) in its laboratory (Figure 1). The spectrometer is equipped with an external port that allows one to feed the light from an external light source to the FTS for analysis. We have built a permanent set-up for the external feed which replicates part of the optical train of the FTS.

Wavelength range and resolution were chosen to match the X-shooter NIR arm. We recorded several spectra of all lamps, varying both current and exposure time. Long exposure times are essential in order to reach a reasonable signal-to-noise ratio. Spectra of the four pen ray lamps are shown in Figure 2.

Physical modelling and simulated data

The Calibration and Modelling Support Group in the ESO Instrumentation Division uses advanced modelling techniques to describe the performance of an instrument. In this we replace the standard empirical method of wavelength calibration (polynomial fitting) by using our physical understanding of the instrument as it was employed in the optical design. During the testing of the instrument the model will be optimised and then describes the instrument as built. This configuration is later used to support the operations of the science data reduction pipeline. During the integration phase of X-shooter, the physical model uses the design parameters. For the purposes of this study it was important not only to know where a photon of a given wavelength arrives on the detector, but also the spectrograph throughput (which we combine with the spectral line intensity) at that wavelength. This is achieved via empirical functions that describe the quantum efficiency of the detectors and the throughput of the dichroics at each wavelength. In addition we include the grating blaze efficiency in the simulation.

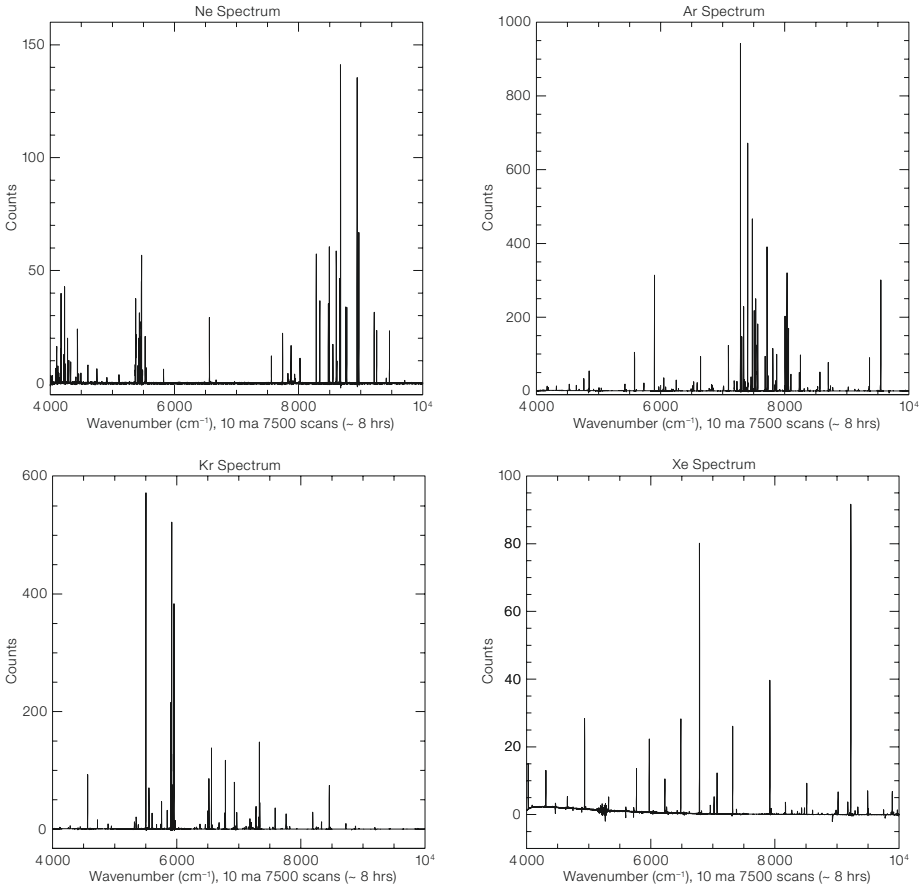

Figure 2: Spectra of the pen ray lamps filled with Ne, Ar, Kr, Xe observed at X-shooter spectral resolution.

We use a Monte-Carlo approach to simulate the counts expected on the detector array during an exposure. In this way 2D simulated data containing many photons are produced by multiple calls of the physical model code. In the current project, we take the 2D simulated data (see Figure 3) for each lamp and extract a 1D spectrum along the loci traced on the detector array by photons arriving at the centre of the entrance slit for all spectral orders. As a result we have, for each lamp and each order, a 1D extracted spectrum. Figure 4 shows a sample 1D spectrum (order #20 of the NIR arm). Full details and an atlas of all X-shooter NIR orders will be available in a comprehensive report (Kerber et al., in preparation).

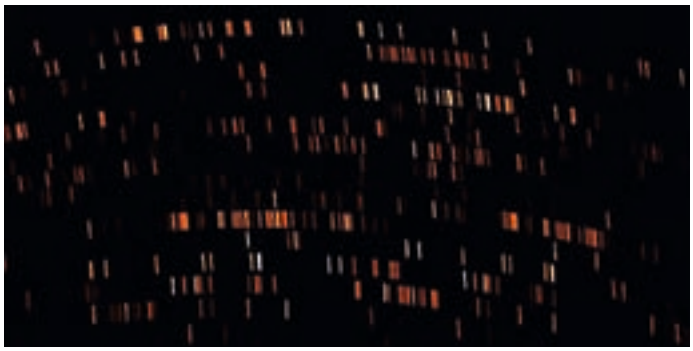

Figure 3: Simulated 2D spectrum of Ne as observed with the X-shooter NIR arm.

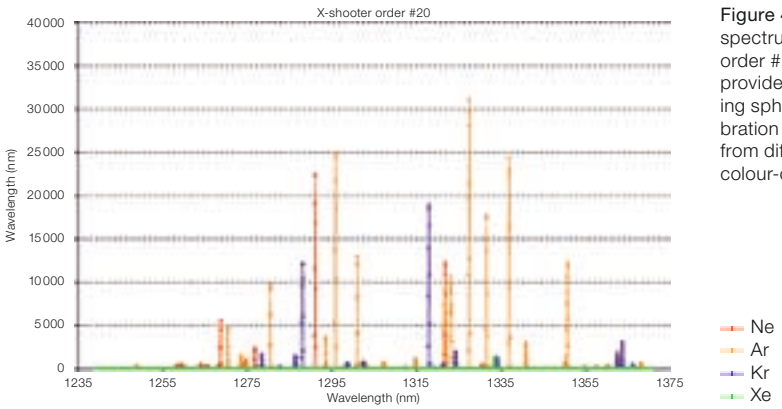

Figure 4: Simulated 1D spectrum of X-shooter order #20 as it will be provided by the integrating sphere in the calibration unit. The lines from different lamps are colour-coded.

Results

The following results have been derived from our measurements for the X-shooter NIR arm:

– The spectra of pen ray lamps filled with Ne, Ar, Kr, and Xe have been measured at a spectral resolution equivalent to the X-shooter NIR, as well as at higher and lower resolution to assess blending of lines.

– The relative intensities of the lamps have been derived as an integral of the line fluxes. The intensities of the Ne, Ar and Kr lamps are within a factor of three of each other while Xe is another three times fainter than the next faintest source.

– No good calibration spectrum can be created from any combination of two lamps.

– A combination of Ne, Ar and Kr provides a suitable spectrum for X-shooter calibration in the NIR. It meets the requirement of 10 lines per order for all but two orders and approaches the goal of 30 lines per order for many orders. We therefore recommend this combination as a baseline for implementation in the calibration unit.

– The addition of Xe will only bring a small improvement in the number of lines and coverage. Since Xe is the faintest source, the feasibility and usefulness of its addition needs to be assessed during laboratory integration and testing.

– The region between 1880 and 2015 nm (orders 13 and 14) is almost devoid of lines, leaving no easy option to remedy the situation. For a dispersion solution based on an empirical polynomial fit, this could be a difficult situation. Since X-shooter will use a physical model to drive the wavelength calibration in the pipeline, we don't expect any significant negative impact on the accuracy of calibrations.

– The spectrum from a Th-Ar HCL offers a less favourable distribution of lines across the NIR spectral range. At the resolution of X-shooter, many of the faint Th lines in its rich spectrum are blended, thus rendering them unusable for calibration purposes.

The results provided need to be verified in detail during testing and commissioning of X-shooter, but they will also help to optimise and speed up the laboratory tests by providing quantitative predictions on the performance of the calibration lamps. This also has the benefit of reducing the pressure on the very busy testing and commissioning phases.

For future instrument developments, our new approach offers the opportunity to estimate and optimise the performance of a calibration system for an instrument already in the design phase.

Acknowledgements

We thank Anton Norup and the Danish partners for providing the pen ray lamps and Gillian Nave and Craig Sansonetti (NIST) for providing line data. We gratefully acknowledge the work by Christophe Dupuy who designed and set up the permanent feed for the external port of the FTS. We thank all colleagues in the X-shooter project for their efforts.

References

Engleman R. Jr., Hinkle K. H. and Wallace L. 2003, JQSRT 78

Hinkle K. H. et al. 2001, PASP 113, 548

Kerber F. et al. 2007, in "The Future of Photometric, Spectrophotometric and Polarimetric Standardization", ed. C. Sterken, ASP Conf. Ser. 364, 461

Palmer B. A. and Engleman R. 1983, LANL 9615

Saloman E. B. 2004, J. Phys. Chem. Ref. Data 33, 765

Sansonetti C. J. and Greene M. M. 2007, Phys. Scr. 75, 577

Sansonetti C. J., Blackwell M. M. and Saloman E. B. 2004, J. Res. Natl. Inst. Stand. Technol. 109, 371

Whaling W., Anderson W. H. C. and Carle M. T. 2002, J. Res. Natl. Inst. Stand. Technol. 107, 149

Future Wavelength Calibration Standards at ESO: the Laser Frequency Comb

Constanza Araujo-Hauck[1]
Luca Pasquini[1]
Antonio Manescau[1]
Thomas Udem[2]
Theodor W. Hänsch[2]
Ronald Holzwarth[2,3]
Andreas Sizmann[3]
Hans Dekker[1]
Sandro D'Odorico[1]
Michael T. Murphy[4]

[1] ESO
[2] Max-Planck Institute for Quantum Optics, Garching, Germany
[3] Menlo Systems GmbH, Martinsried, Germany
[4] Institute of Astronomy, University of Cambridge, United Kingdom

A new technique for precise wavelength calibration of high-resolution spectrographs using frequency combs has recently been proposed. After introducing the basic concepts and advantages of this technique, we describe the ongoing development between ESO and the Max-Planck Institute for Quantum Optics for a novel wavelength calibration system that aims, within three years, to construct a laboratory demonstrator.

The quest for improved wavelength calibration

With the advent of large (and extremely large) telescope collecting areas and superstable instruments, high-precision spectroscopy in astrophysics is becoming a very exciting reality. Several areas of forefront research have been developed in the last decade, such as the detection of planets around other stars, the measurement of possible variations in physical constants, the determination of element isotope ratios and the proposed direct measurement of the expansion of the Universe. All share the requirement of very high precision in the measurement of spectral line wavelengths.

High-precision wavelength measurements require a high-resolution spectrograph with special characteristics in terms of thermal and mechanical stability, detector linearity and reproducibility. The reader interested in more details can refer to the proceedings of the "High Precision Spectroscopy in Astrophysics" workshop (Santos et al. in press), held in September 2006 in Aveiro (Portugal). There is now a general consensus that an even higher precision is needed:

- for the detection of earth-mass planets in habitable zones around solar-type stars and/or the unambiguous characterisation of stellar systems with many orbiting planets (like our own Solar System), which will require a long-term precision of better than 10 cm/sec.
- to resolve the currently controversial issue of possible variation in the physical constants as derived from quasar spectra and to increase the precision in order to compete with space-based constraints from atomic clock experiments (e.g. from the planned ACES experiment by ESA), which requires an improvement of a factor between 10 and 100 over the present measurements.
- for measuring the change of the expansion rate of the Universe from Ly-α forest quasar absorption spectra, which requires a precision of a few cm/sec over a 30-year baseline (Grazian et al. 2007; Liske et al. 2007).

One (if not THE) crucial subsystem in any high-precision spectrograph is the wavelength calibration source (Lovis et al. 2006). The ideal calibration source should have a very high density of lines that are uniformly spaced and whose wavelength is known from first principles. All the lines should have similar intensity and should cover the whole spectral range of interest without blends. Crucially, they must be stable and reproducible to an exceedingly high accuracy for many years. All of this may appear excessive to some of our readers, but it is worth recalling that a precision of 1 cm/sec corresponds, on the focal plane of a typical high-resolution spectrograph, to a shift of a few tenths of nanometer, which compares to typical molecular sizes. Moreover, we aim to maintain this precision over a period of 10 years, or more!

The standard wavelength calibration sources used in most spectrographs are the hollow-cathode Thorium-Argon (Th-Ar) lamps. These lamps have been used for decades, because of their numerous advantages. However when pushing the performance, a number of limitations arise, the most noticeable being: line blending; long-term variability; and the high non-uniformity of the line distribution and intensity (see e.g. Lovis et al. 2006).

Prompted by the need to improve this calibration scheme, a group of researchers from different institutes has started to look into other alternatives, finding that a significant step towards the ideal calibration source might be achieved with the relatively new technology of laser frequency combs (Udem et al. 2002; Murphy et al. 2007).

The Laser Frequency Comb

A laser frequency comb consists of thousands of equally-spaced frequencies over a bandwidth of several THz. It is based on the properties of femtosecond (fs) mode-locked lasers. The shorter the laser pulses, the broader the range of frequencies in the comb (see Figure 1).

The resulting modes of the frequency comb have their origin in the repetitive pulse train of the mode-locked laser. The mode spacing, which is constant in frequency space, is given by the pulse repetition frequency and resides in the radio frequency domain. The repetition frequency can readily be synchronised with a precise radio frequency reference such as an atomic clock. These clocks provide by far the most precise measurements of time and frequency currently available, the most reliably determined quantities in physics. Frequency combs therefore satisfy two requirements of the perfect calibration source which other methods do not: uniform line-spacing and long-term stability and reproducibility. The novelty of laser combs has been widely recognised, and the 2005 Nobel Prize in Physics was awarded to Profs. Ted Hänsch and John Hall, for their fundamental and pioneering work in the development of the optical frequency comb technique.

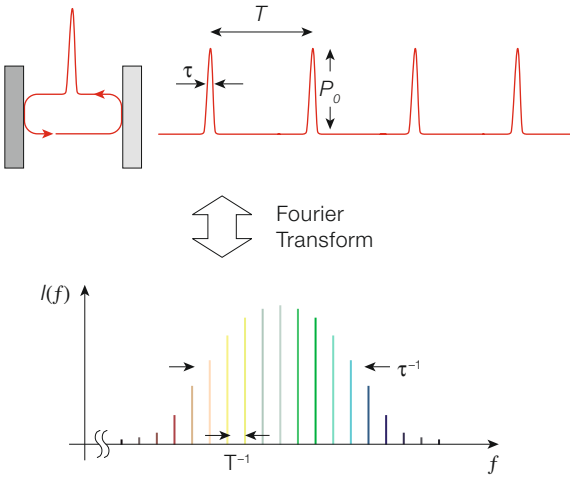

Figure 1: In the time domain, the pulses of a typical mode-locked laser (in red), characterised by its pulse repetition rate (T) and its pulse duration τ ~ fs, are shown (top). Shown below in the frequency domain, the pulse of the above mode-locked laser produces the frequency comb, with its parameters, the repetition frequency T^{-1} and spectral width τ^{-1}.

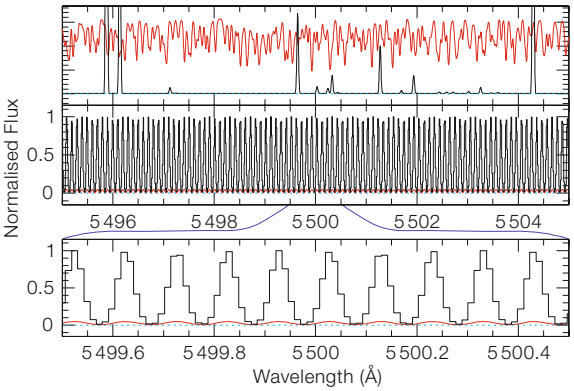

Figure 2: Th-Ar lamp (red) and the iodine cell spectra (black) as recorded at the focal plane of a high-resolution spectrograph (top), *versus* the simulated frequency comb spectra for the same spectral region (middle). In the lower frame is shown a zoom of the comb spectra for a 1 nm window, where the red solid line shows the error array, exaggerated by a factor of 25 (see Murphy et al. 2007).

The laser frequency comb has a number of advantages over other traditional wavelength calibration sources. It guarantees long-term stability over many years; the absolute wavelength of each line in the comb is known *a priori* (i.e. without the need for previous laboratory measurements); and it has a very high precision, only limited by the reference signal, which could be an atomic clock or a GPS receiver, depending on the required stability. Another interesting feature is the high density and equidistance of emission lines, over a wide wavelength range, both of which will allow tracing and modelling of the wavelength solution at the focal plane of the spectrograph with a very high accuracy, enabling higher S/N detection in spectra.

In Figure 2 we show the Th-Ar, the iodine cell and the simulated laser frequency comb spectra over the same spectral region for comparison. The advantage of the comb is evident.

Implementing a Laser Frequency Comb calibration system

ESO and the Max-Planck Institute for Quantum Optics (MPQ) have studied the technical feasibility of building a wavelength calibration system based on a laser frequency comb, which could be used in present and future generations of high-resolution spectrographs. The requirements and specification were based on a CODEX-like instrument (Pasquini et al. 2006). The conclusion of that study is that none of the presently available laser comb systems could provide all the characteristics required by this application, but the development of such a unit, although challenging, is feasible.

Two requirements have been identified as the most demanding (Araujo-Hauck et al. 2007): wavelength coverage; and frequency mode separation. The minimum spectral range of operation is in the visible band, from 400 to 680 nm with a possible extension from 350 to 1000 nm. Ideally, this would be obtained from a single comb by symmetric broadening of the frequency spectrum with some power constraint for the nonlinear conversions, like second or third harmonic generation, in order to reach the final spectral range.

Our simulations show that the optimum frequency mode separation for an R = 150000 spectrograph, is about 13 GHz. Commercial femtosecond lasers have typical frequencies as high as a few hundred MHz, which would appear as a continuum in our spectrographs. The feasibility of increasing the mode separation has not yet been demonstrated and is likely to be the most challenging part of this development, due to the high power required to carry out the nonlinear processes at high-pulse repetition rates. To date there is no laboratory demonstration of femtosecond laser sources with repetition rates larger than 10 GHz (Hoogland et al. 2005).

The proposed solution is shown in Figure 3. It consists of a High Repetition Rate (HRR) fs source, a non linear frequency conversion, and a mode filter cavity that will be the last step to achieve the desired mode spacing. The latter item presents a major development challenge, but has the significant advantage that the line spacing can be varied to lower and higher free spectral ranges in multiples of the fundamental comb line spacing.

On account of the common interest for ESO and MPQ, both organisations have agreed to start the research and development activities with the objective to build a laboratory prototype that meets the requirements of a wavelength calibration source. This research will focus on different key aspects of the desired system: identification of the high repetition rate light source, development of the non-linear conversion chain, and the filter mode cavity which will allow us to reach the desired frequency mode spacing. A Ph.D. thesis has been awarded on the subject at MPQ and a postdoctoral position de-

voted to support the project. The first set-up for the development of a filter mode cavity has been assembled on the MPQ optical bench, and is shown in Figure 4.

It is expected that within three years this research effort will result in a laboratory system that meets the performance requirements. A travelling unit to be tested, feeding a spectrograph operating at a telescope, could be available in a timeframe of approximately four years.

In conclusion, a programme to develop a frequency comb calibration system has been established in collaboration between ESO and the MPQ, with the aim to provide a wavelength calibration system of unique accuracy and long-term stability for astronomical spectroscopy. The success of this programme is crucial to maintain ESO community leadership in high-resolution spectroscopy and the associated scientific areas of research, such as exoplanet detection and cosmology from high-redshift absorption lines.

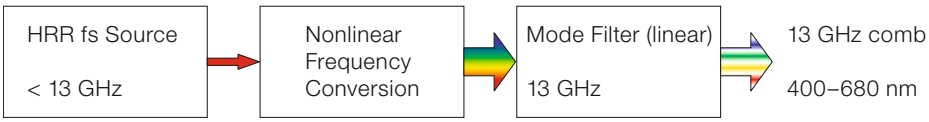

Figure 3 (above): Block diagram for the proposed laboratory demonstrator of the calibration system based on a frequency comb.

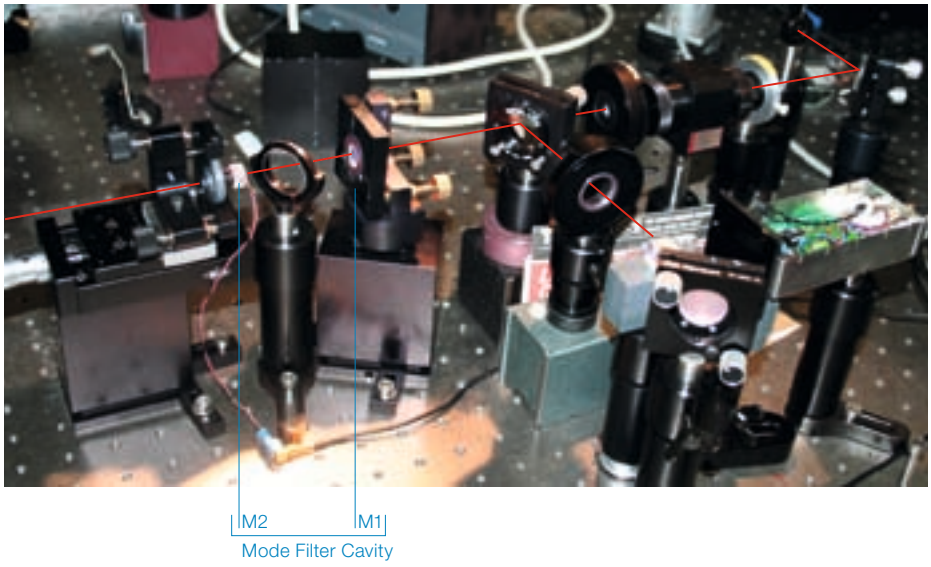

Figure 4 (below): Laboratory set-up at MPQ to test the filter cavity. The red line represents the laser path. On the left, the Fabry Perot filter cavity. On the right, the different optical components for analysis, control and diagnostics.

References

Araujo-Hauck C. et al. 2007, in Proceedings of the 2007 ESO Instrument Calibration Workshop, ESO Astrophysics Symposia Series, in press
Grazian A. et al. 2007, A&A, submitted
Hoogland S. et al. 2005, IEEE Photonics Technology Letters 17, 267
Liske J. et al. 2007, MNRAS, submitted
Lovis C. et al. 2006, Proc. SPIE 6269, 62690P
Murphy M. T. et al. 2007, MNRAS, submitted, astro-ph/0703622
Pasquini L. et al. (CODEX Team) 2006, in "The scientific requirements for ELTs", Proceedings of IAU Symposium 232, eds. P. Whitelock, M. Dennefeld, and B. Leibundgut, Cambridge, 193
Santos N., Pasquini L. and Romaniello M. (eds.) 2007, "Precision Spectroscopy in Astrophysics", Proceedings of the Aveiro Conference, Springer, in press
Udem T., Holzwarth R. and Hänsch T. W. 2002, Nature 416, 233

Photo: H. H. Heyer, ESO

A recent view of the Instrument Integration Hall at ESO Headquarters in Garching. In the foreground are parts of the HAWK-I dewar.

ESO's Next Generation Archive System in Full Operation

Andreas Wicenec, Jens Knudstrup
(ESO)

Considerations of the technical feasibility and the cost implications of a disk-based archiving system to store digital observations coming from the ever growing suite of ESO telescopes and instruments began in 2000. The so-called Next Generation Archiving System (NGAS) started archiving data in a prototype system in 2001. Now the second generation of NGAS hardware has been installed in the new ESO data centre and about 98 % of all data since 1998 have been migrated onto disks hosted on NGAS computers. In addition all data currently produced by ESO instruments is directly archived onto NGAS hosts both in La Silla and Paranal. Currently the ESO archive keeps about 125 TB of data online and the system has been scaled up to cope with the next data wave coming from VISTA and OmegaCAM.

The NGAS concept

The release of a white paper (Wicenec and Pirenne 2000) describing the technical feasibility and the cost implications of a disk-based archiving system marked the start of a new chapter in a quite different area than commonly described in the ESO Messenger. This story is about persistently storing digital observations coming from the ever growing suite of ESO telescopes and instruments. The so-called Next Generation Archiving System (NGAS) started out as an idea and a feasibility study. In the first Messenger article from December 2001 (Wicenec et al. 2001), it was still described as a prototype system. Early in July 2001 the Data Management Division (now Data Management and Operations Division) installed prototype versions of the archiving and buffering units of NGAS in the control room of the 2.2-m telescope in La Silla. The two units were the on-site part of an archiving system we were testing at that time for high data rate/high data volume instruments like the Wide Field Imager mounted at the 2.2-m telescope (WFI@2p2). The original NGAS concept was built around two basic ideas: use of cheap commodity hardware with magnetic ATA-100 disks as the archiving and transport media; a highly flexible and modular software called NG/AMS, Next Generation/Archive Management System. The main goals of the whole system are scalability and the ability to process bulk data within the archive itself. In fact NGAS scales in a way so that it is possible to process all the data in the archive within an almost constant time. In the meantime technology advances have led to the usage of SATA2 rather than ATA-100 disks, but that is quite a minor detail. On the technology side we had to change hardware components for newly procured NGAS computers several times, but the first computers installed at La Silla were only replaced and upgraded in 2005 in order to provide more redundancy and to be able to capture all data from all the instruments operating at La Silla. At the same time the NGAS systems were moved to the RITZ (Remote Integrated Telescope Zentrum).

Figure 1: Close-up view of some of the NGAS machines of the primary archive cluster in the new ESO data centre.

On the Garching side, in the main archive, we started with eight computers, with eight disk slots each. The disks used in 2001 had 80 GB and were close to the optimal price/capacity ratio at that time; they were filled up with one week of typical WFI@2p2 operation and were then ready to be shipped to Garching via the diplo bag. The latter highlights another key point of the NGAS concept, the shipping of hard disks and the full traceability of the shipment procedure. In NGAS operational terms, magnetic disks are consumables and data can be migrated freely from one disk to another. In fact every file stored on NGAS is fully virtualised in the sense that access to a file is solely controlled using a unique NGAS file ID. There is no need to know the actual computer, disk or directory path where the file is located. A request for a file with a given ID can be issued to any NGAS computer available on the network; the NG/AMS will figure out where the closest available copy is available and deliver that copy to the requester.

The last feature of the NGAS concept is the interoperability of NG/AMS with other components of the Data Flow System (DFS) and other client software or direct human users. In order to minimise the implementation impact on both the NG/AMS server and the clients, it was decided very early on in the project to use an existing very simple protocol which is as widely available as possible. Consequently NG/AMS is actually implemented as an HTTP server. All available commands can be issued through standard HTTP clients, including web browsers. NG/AMS is supposed to be used through software rather than directly by humans, and the latter is not recommended because the core NG/AMS does not provide a real page-oriented web interface.

NGAS requirements

Back in 2001, a new archiving system had to resemble the operational scheme of the existing system as closely as possible and be similar in terms of cost. For the costs, it is clear that one has to account for the pure hardware costs, as well as the operational and maintenance costs. The hardware includes the costs for the consumable media, readers, writers (if any) and computers. In order to be able to use magnetic disks as an archiving

media, the overall system has to fulfil a number of basic requirements:
– Homogeneous front-end (archiving at observatory) and back-end (science archive) design;
– Access to archive scalable, i.e. the number of entries and volume of data shall not affect the access time to single data sets;
– Support bulk data processing;
– Processing capabilities should scale along with archived data volume, i.e. it should be possible to process all data contained in the archive;
– An economical solution using commodity parts to reduce overall costs. This consideration also includes power economy, whereby unused servers are switched down after a configurable idle time and then woken up for a request, in order to save power;
– Possibility to use the magnetic disks as a transport medium for the bulk data.

The main goal of the first point is to limit maintenance costs, operational overheads and the time-to-archive. Time-to-archive is the total time the complete system needs until the data is online and retrievable (disregarding access restrictions) from the science archive. The support for bulk data processing is mainly driven by the fact that ESO is already now processing almost 100 % of all data, in order to ensure the data quality for service mode programmes, monitor the telescope/instrument parameters and provide master calibration frames for the calibration database.

NGAS archive facts and facets

The currently installed NGAS cluster for the primary archive can host up to 150 TB of data, distributed across 24 machines with 24 disks each (see Figure 1). In this configuration it is already prepared to start receiving and storing VIRCAM and OmegaCAM data from VISTA and VST respectively, in addition to the data stream from the VLT, VLTI, and La Silla telescopes. As of end July 2007, the primary archive holds more than 7.2 million individual frames obtained by ESO instruments (in general one observed frame results in one file in NGAS). The total number of files stored on NGAS at present amounts to almost 30 million. The large number is due to the fact that at the moment at least two copies of each file are kept in the primary archive, because the secondary archive is still in the process of being populated before becoming fully operational. In addition also the master calibration frames produced as a part of the quality control process of most of the ESO instruments, as well as auxiliary files and log files, are archived on NGAS. The archive system design and the use of commodity hardware in both the primary and the secondary archive meet the goal of keeping development, maintenance and operations costs low.

With the new VO-compliant science archive interfaces to be released by the end of this year, we expect that significantly more scientists will be able to exploit and use the archived data beyond its original scientific intent. About 1 million requests every month are served by the NGAS archive main servers. Most of these requests are internal to ESO operations, quality control processing and archive maintenance requests, but without the online nature of the NGAS archive all these processes would need substantially more time and staging disk space. The new VO compliant interfaces require also direct access to the data, essentially through web links (URLs). This introduces a new paradigm for access to ESO data by external users, because up to now the data is only served in an asynchronous way and requesters receive e-mails upon completion of their requests. In the future the data will be almost directly served by NGAS to the global astronomical community. In order to be able to cope with these new requirements, the network infrastructure of the NGAS cluster will be changed as well, in order to make full use of the intrinsic parallelism.

On the front-end side NGAS is archiving between 1000 and 6 000 new observations every night. This rate is mainly dependent on the number and type of instruments operated on the mountains and on the weather conditions. Some instrument modes are quite demanding for the rate of archiving files, which may in some exceptional cases rise to several hundreds of thousands of files per day. In addition to the La Silla Paranal instruments, the raw data of the WFCAM instrument on the UK Infrared Telescope (UKIRT) in Hawaii and the data from the APEX sub-millimeter telescope are also archived on NGAS. In particular, the data from WFCAM poses quite an additional load and required a special set-up, because, firstly, this instrument produces about 200 GB of data every clear night and, secondly, the data is archived through the network from Cambridge, UK.

The NGAS implementation

As already mentioned NGAS is an integrated hardware and software solution for bulk archiving, archive management and basic large-scale file processing. This means that both the hardware and software configurations have to be kept under strict configuration control. For the hardware this includes not only the single computers, but also the cluster and network configuration, the racks, the cooling concept, the connection to external systems, like the quality control processing cluster and the secondary archive, and the compatibility between the front-end mountain-top systems and the primary archive.

The hardware

As an integrated system where magnetic disks are to be used as consumables, we had to be more strict in the selection and maintenance of the machines and their components. In particular the requirement to use the disks as a data transport medium requires that the machines on the mountains and the machines in Garching use compatible disk slots and disk trays. Since removing and mounting disks is a very regular and standard procedure, the mechanics have to operate both smoothly and reliably and the parts have to be rigid enough to perform many mount/remove cycles. At the same time the trays should be compact, provide efficient cooling and not be too expensive. The disks are shipped in their trays and are then mounted in a different machine, thus the slots have to be fully compatible. In order to have better control on such details we have chosen a computer selection process which involves the specification of computer parts rather than a model. All of the parts are commodity parts and thus easily

available from many vendors. The new ESO data centre, which was inaugurated on 27 July, hosts the 24 machine NGAS cluster (see Figure 2). With a future upgrade of this cluster with high capacity disks and a different RAID configuration, these 24 machines can host up to 0.5 Petabyte of data.

The software

The machines are installed using a standard Scientific Linux OS installation with customised packages, and some customised system configuration, followed by an installation of the NG/AMS software. NG/AMS is written in 100 % pure Python. Python is an object-oriented scripting language in wide use; for more information on Python see *http://www.python.org*. The experience of writing and maintaining a rather big server application in Python is quite positive, mainly because of the clarity and compactness of the language. Things like 'Segmentation fault' and the related, sometimes tedious, debugging sessions simply do not occur and the very clear object orientation of the language allows for a clean and proper design of even complex object relations. The high-level built-in modules add to a very efficient way of programming, resulting also in a comparably low number of code lines.

NG/AMS in its core is a multi-threaded HTTP server. The software implements 20 custom commands, where the most important ones certainly are ARCHIVE and RETRIEVE. These commands are accessible through standard URLs of the form: *http://ngasserver:7777/RETRIEVE?file_id=this_is_my_file*[1].

The ARCHIVE command supports both push and pull of data, i.e. a file can be pushed by a client using a standard HTTP POST method or it can be pulled from some other server, for instance an ftp server, if a URL is specified. NG/AMS features full virtualisation, which means that on retrieval the only thing one has to know is the NGAS file-id and the name and port of *one* accessible NGAS server of the archive in order to access any file anywhere on any NGAS machine of the ESO archive. Thus, in principle, one could retrieve the last frame observed in Paranal by just knowing its file-id. In practice, however, this is not possible because access restrictions apply for computers running in the La Silla Paranal Observatory. To ensure the safety and security of the data, none of the operational NGAS servers are accessible from outside ESO and even inside ESO only a few machines and users can access them.

In order to trace the location of every file in the system, NGAS uses a database which contains information about all NGAS hosts, disks and files. There are additional tables to control the history and the location of disks even if they are not on-line, have been retired or are currently travelling to one of the sites. By default NGAS always keeps two copies of every file and this is rigidly controlled and checked throughout the operations. Without some effort and special permission it is not possible to remove a file if that would result in less than two copies being available, and, anyway, being an archiving system, deleting files is a protected action. The consistency of the contents of the database and the files on disks is checked periodically; this includes the calculation of a checksum for every file. If discrepancies are detected the software sends an notification e-mail to the archive administrators.

There are a number of advanced features in NGAS, which are currently not, or only marginally, used in the ESO operational environment. These include a power saving mode, where NGAS nodes will go into sleep mode and are automatically activated to handle requests and for consistency checking. Another as yet unimplemented feature is the processing of files upon request and the return of only the result of this process.

NG/AMS is very flexible and configurable. It provides 10 different plug-in types to customise the behaviour of various parts of the system, these include plug-ins which are executed when the system goes online and offline, when data is archived or registered, and for processing and checksum calculation. For the power-saving mode there is a plug-in which causes the node to go to sleep and another one which wakes it up. NG/AMS also provides a subscription service, where one node can subscribe for data being newly archived on another node.

Figure 2: The current 24-machine NGAS cluster in its new location, the ESO data centre. Each of the three racks weighs about 1 000 kg and uses a sophisticated dual cooling system, located behind the narrow grey doors. The cluster can host up to 576 SATA disks. With the currently used 400 GB disks this translates to a total capacity of 156 TB in 48 RAID5 disk arrays.

[1] This is a fake URL.

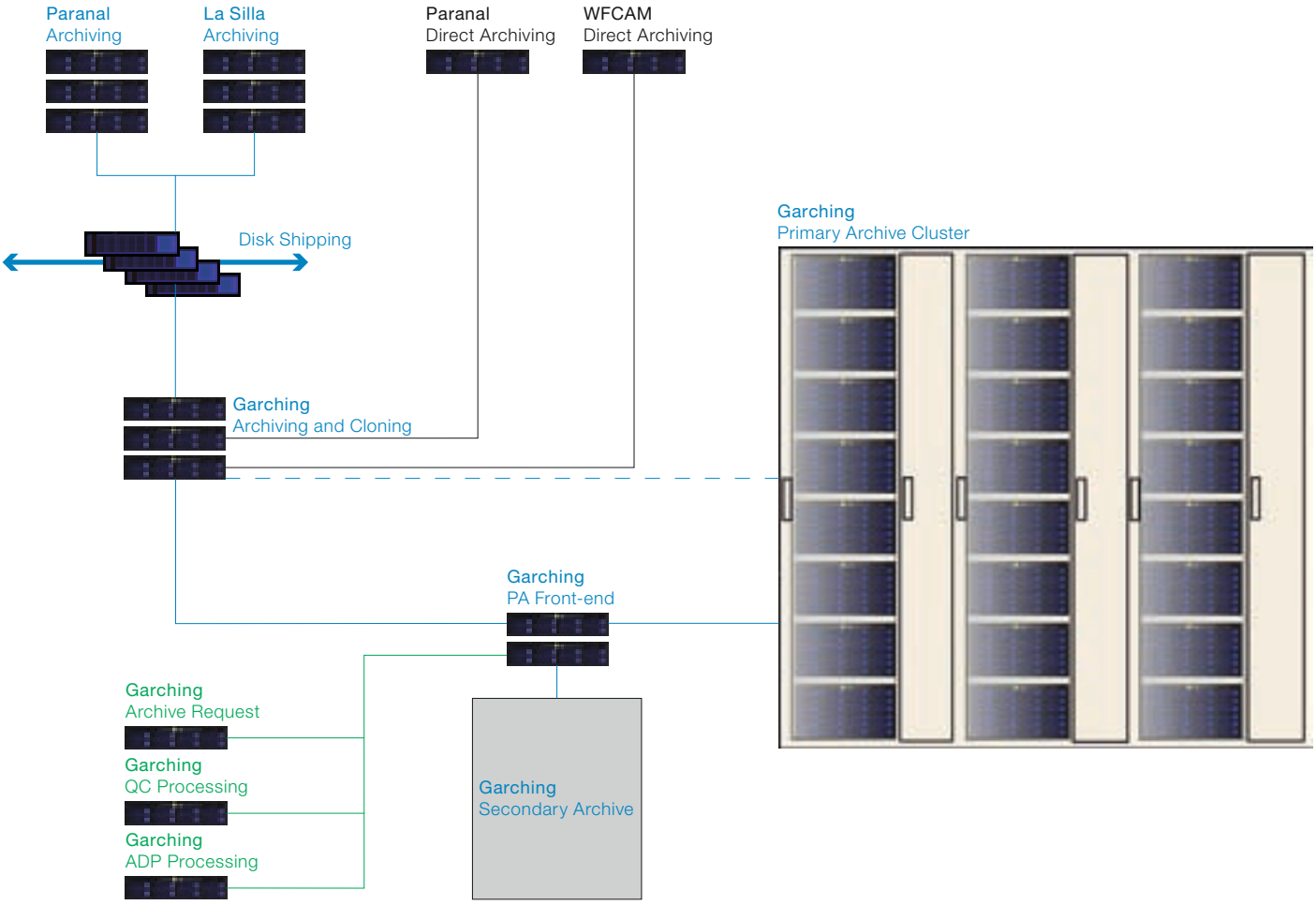

Figure 3: Schematic view of the complete NGAS data flow. The main data from the La Silla Paranal observatory is archived on NGAS machines in the observatory and then shipped to Garching. This part of the observatory data flow is highlighted with blue letters and lines. The green letters and lines highlight data flowing from and to the NGAS primary archive cluster, to post observation requests, quality control and advanced data product processing. The black letters and lines mark custom configurations for pre-imaging data from Paranal and for the data from the UK WFCAM camera.

For this subscription mechanism there is a filter plug-in to be able to subscribe only to data which fulfils certain criteria. In addition the latest version of the ALMA branch of the software also provides a mechanism to register and execute new commands. This flexibility enables the usage of NG/AMS in many different situations and hardware set-ups. The core software is completely independent of the hardware and can be run even on a laptop.

NGAS operations

As can be seen in Figure 3 NGAS, is operated at three different ESO sites. Both observatory sites have a small three-machine cluster, where only one machine is actually used for archiving data, one is a disk handling unit and one is a spare. The direct archiving from Paranal and Cambridge, UK, is done using a stand-alone NGAS archiving client and is thus not a full NGAS installation. The Garching installation is a bit more complex with the complete primary archive and a number of archiving and disk handling units. There are several external applications, which use NGAS to archive or request data. These include the standard archive requests, where the ESO request handler is the application which executes the actual retrieval. The quality control (QC) processing is executed on its own cluster of machines and retrieves almost all observed frames from NGAS using a direct client. After finishing the process, the QC scientists of the Data Flow Operations department also archive the results on NGAS. This involves mainly the master calibration frames, but a new application supporting the archiving and proper registration of the quality control science products is currently being tested. Another heavy user of the NGAS archive is the processing carried out by the Advanced Data Products (ADP) processing of the ESO Virtual Observatory Systems department. Also in this case a large fraction of the whole archive is requested, processed and the results are archived and registered.

The secondary archive essentially is a back-up of the whole NGAS cluster on a Sony Petabyte tape library. A special application has been developed to interface NGAS with the commercial application, called ProTrieve, controlling the

tape library. Obviously the tape library has to be able to store the same amount of data as the NGAS cluster and thus some care has been taken to procure a scalable solution for this as well. All the hardware for the primary archive and the secondary archive, as well as ProTrieve, have been procured and are maintained through a frame contract with the Munich-based company Kayser-Threde.

NGAS activities elsewhere

NGAS is not only used by the ESO archive, but has also been chosen by ALMA (*http://www.eso.org/projects/alma*); it hosts almost the complete ST-ECF Hubble Space Telescope Archive (*http://www.stecf.org/*) with about 10 TB of data; and it is used for the long-term VLA archive at the NRAO in Socorro. It is also under investigation for the Hubble Legacy Archive (HLA) activities (see *http://hla.stecf.org* for details) both at ST-ECF and at STScI in Baltimore.

Milestones and performance

The front-end system consisting of two NGAS units was installed at the ESO 2.2-m telescope in the beginning of July 2001. Since then, this prototype installation has evolved into a rather big operational system, which is now archiving and controlling practically all data collected by ESO instruments. The historical timeline is:

– NGAS unit prototype installation La Silla, 3 to 13 July 2001
– Start of operations on La Silla, 7 July 2001
– First terabyte of data controlled by NGAS, 18 September 2001
– Installation of first two NGAS units for the main archive at ESO Headquarters, 25 September 2001
– Commissioning and acceptance of front-end NGAS on La Silla, December 2001
– Commissioning and acceptance of back-end NGAS at ESO Headquarters, February 2002
– Installation of the VLTI NGAS on Paranal, January 2004
– Upgrade of the NGAS installation in La Silla, January 2005
– Upgrade of the NGAS installation in Garching and data migration, first half of 2005
– Installation of new NGAS hardware on Paranal and La Silla, supporting the archiving of all data from all instruments, November 2006
– Almost all data migrated from DVDs to NGAS, March 2007

The front-end NGAS is not yet fully optimised for performance, but the time-to-archive was always shorter than the production time of frames by the instruments. The typical throughput of the archiving process on the current hardware is up to 15 MB/second, including compression and replication of the files. The hardware used in the NGAS units provides very fast write access to the data disks in parallel, summing up to about 350 MB/second (measured), thus there is plenty of room for improvement of the overall system performance.

One bottleneck is the database access, which sums up to a non-negleglible load on the database server in Garching, because the whole NGAS system is writing its information into the same database. The Paranal and La Silla NGAS databases are being replicated to the Garching database as well. With 30 million archived files in total and up to many hundreds of thousands of files on a single volume, the queries have to be analysed and optimised in order to improve the transaction times. For safety reasons NGAS performs many consistency checks and holds up to three copies of the data during certain requests, for some type of requests this high safety level might not be necessary and could be lowered. This has been already implemented on the ALMA branch of the NG/AMS for the data retrieval command. The performance increase is about a factor of 25 and clearly shows the potential of such optimisation work.

Future of NGAS

NGAS has proven to be a reliable and fast system. It has managed many tens of millions of files, where the problems were mainly due to hardware/software interactions. Given the off-the-shelf inexpensive hardware used, the reliability in fact is quite remarkable and confirms the study of Schroeder and Gibson (2007) which essentially states that this kind of inexpensive hardware does not fail significantly more often than very expensive hardware. Since now the NGAS archive captures all data from the La Silla Paranal Observatory and almost all 'historic' ESO data has been migrated as well, NGAS really has become *the* persistent storage backend of the ESO archive. The flexibility of the NG/AMS software allows a fast customisation of the full system to other requirements, like ALMA and HST, or adjustments to different hardware. Quite new developments are the usage of NGAS for one of the reference implementations of the VOSpace standard of the International Virtual Observatory Alliance (Graham et al. 2007). As a side-product of this, a prototype WebDAV (Web Distributed Authoring and Versioning is a proposed standard of the Internet Engineering Task Force (IETF), see Dusseault 2007) interface on top of NGAS has been implemented, which exports NGAS as a mountable file system (Harrison et al. 2006).

Acknowledgements

We would like to thank especially the 2.2-m telescope team, Flavio Gutierrez and Jose Parra and the La Silla Paranal Data Handling Administrators (DHA) for their invaluable support during the installation and operational phase of NGAS. In addition we would like to thank the SOS and the EDAT teams and in particular Dieter Suchar for their support in the design, procurement, set-up and operation of the NGAS hardware. We would also like to thank Nathalie Fourniol and the SAO and SEG groups for their suggestions for improvement and many fruitful discussions.

References

More detailed information on NGAS is available at *http://www.eso.org/projetcs/ngas*

Dusseault L. (ed.) 2007, RFC 4918, *http://www.ietf.org/rfc/rfc4918.txt*

Graham M. et al. 2007, VOSpace service specification, Version 1.01, *http://www.ivoa.net/Documents/latest/VOSpace.html*

Harrison P. et al. 2006, in "Astronomical Data Analysis Software and Systems XV", ASP Conference Series 351, 402

Schroeder B. and Gibson G. A. 2007, presented at the 5th USENIX conference, *http://www.cs.cmu.edu/bianca/fast07.pdf*

Wicenec A. and Pirenne B. 2000, The Next Generation of Science Archive Storage, *http://www.eso.org/projects/ngas/ngas-whitepaper.pdf*

Wicenec A., Knudstrup J. and Johnston S. 2001, The Messenger 106, 11

Beam of the Laser Guide Star pointing out of the dome of VLT UT4 (Yepun) towards the Galactic Centre (ESO Press Photo 33/07).

Photo: Y. Beletsky, ESO

Status and Perspectives of Astroparticle Physics in Europe

Christian Spiering
(DESY – Deutsches Elektronen-Synchrotron, Zeuthen, Germany)

Astroparticle physics has evolved as an interdisciplinary field at the intersection of particle physics, astronomy and cosmology. Over the last two decades, it has moved from infancy to technological maturity and is now envisaging projects on the 100 M€ scale. This price tag requires international coordination, cooperation and convergence to a few flagship projects. The Roadmap Committee of ApPEC (Astroparticle Physics European Coordination) has recently released a roadmap covering the next ten years. ApPEC is a corporation of European funding agencies promoting astroparticle physics.

In 2002, Ray Davis and Masatoshi Koshiba were awarded the Nobel Prize in Physics for opening the neutrino window to the Universe, specifically for the detection of neutrinos from the Sun and the Supernova SN 1987A in the Large Magellanic Cloud. Their work was a unique synthesis of particle physics and astrophysics. Solar neutrinos also provided the first clear evidence that neutrinos have mass. It is this interdisciplinary field at the intersection of particle physics, astronomy and cosmology which has been christened *astroparticle physics*.

The detection of solar and supernova neutrinos is not the only new window to the Universe opened by astroparticle physics. Another one is that of high energetic gamma rays recorded by ground-based Cherenkov telescopes. From the first source detected in 1989, three sources known in 1996, to nearly 40 sources identified by the end of 2006, the high-energy sky has revealed a stunning richness of new phenomena and puzzling details (see Figure 1). Other branches of astroparticle physics have not yet provided such gold-plated discoveries, but have moved into unprecedented sensitivity regions with rapidly increasing discovery potential – like the search for dark matter particles, the search for decaying protons or the attempt to determine the absolute values of neutrino masses.

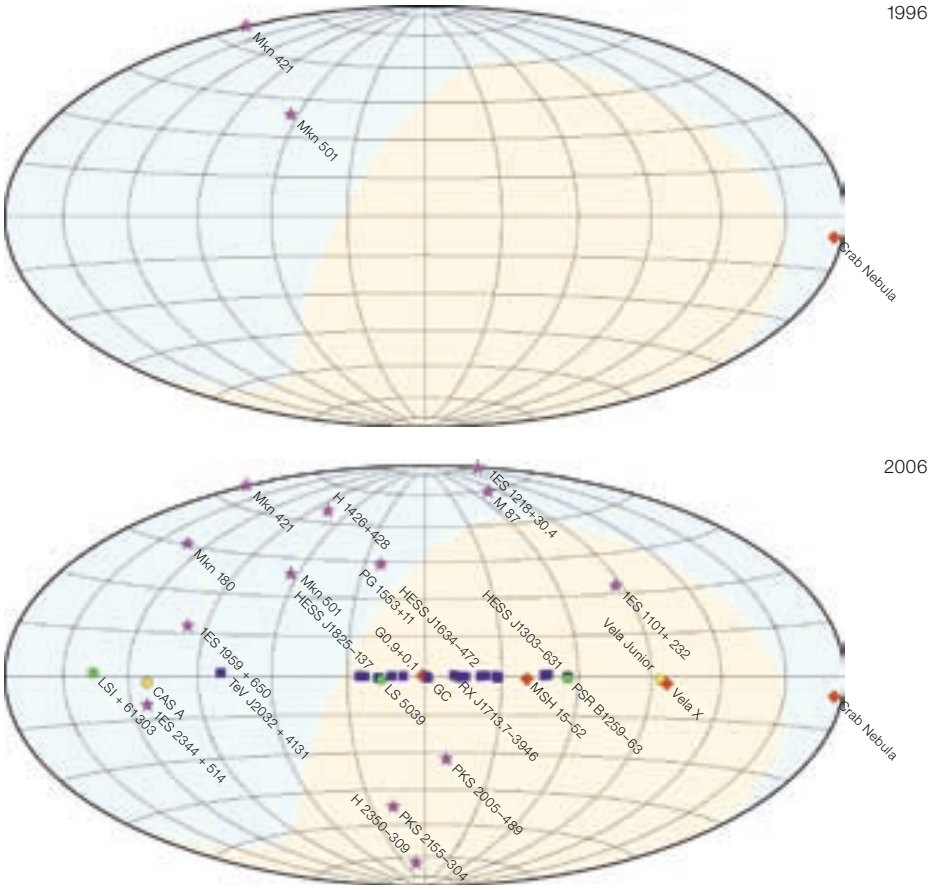

Figure 1: The TeV gamma-ray sky as seen in 1996 and 2006. (Graphic courtesy Konrad Bernlöhr, MPIfK) Background colours indicate northern (blue)/ southern (yellow) sky.

Basic questions

Recommendations of the Roadmap committee (*http://www.aspera-eu.org*) were formulated by addressing a set of basic questions:

1. What are the constituents of the Universe? In particular: What is dark matter?
2. Do protons have a finite life time?
3. What are the properties of neutrinos? What is their role in cosmic evolution?
4. What do neutrinos tell us about the interior of the Sun and the Earth, and about supernova explosions?
5. What is the origin of cosmic rays? What is the view of the sky at extreme energies?
6. What will gravitational waves tell us about violent cosmic processes and about the nature of gravity?

An answer to any of these questions would mark a major breakthrough in understanding the Universe and would open an entirely new field of research on its own.

Search for Dark Matter

The favoured solution to the Dark Matter mystery assumes Weakly Interacting Massive Particles (WIMPs) produced in the early Universe. A natural candidate for WIMPs is the lightest particle of Minimal SuperSymmetric Models (MSSM), the neutralino. WIMP searches focus on the detection of nuclear recoils from WIMPs interacting in underground detectors (Baudis 2005, Sadoulet 2007). No WIMP candidate has been found so far. Assuming that all Dark Matter is made of these exotic particles, present experi-

ments with a several kg target mass can therefore exclude WIMPS with interaction cross section larger than ~ 10^{-43} cm^2. MSSM predictions for neutralino cross sections range from 10^{-47} to 10^{-41} cm^2. Experimental sensitivities will be boosted to 10^{-44} cm^2 in about a year and may reach, with ton-scale detectors, 10^{-46} cm^2 in 7–8 years. Therefore, there is a fair chance to detect dark matter particles in the next decade – provided the progress in background rejection can be realised and provided Dark Matter is made of supersymmetric particles. Presently favoured candidate devices are 'bolometric' detectors operated at a temperature of 10–20 mK which detect the feeble heat, ionisation and scintillation signals from WIMP interactions, and noble liquid detectors (Xe or Ar) recording ionisation and scintillation. A variety of presently more than 20 Dark Matter experiments worldwide must, within several years, converge to two or three few ton-scale experiments with negligible background.

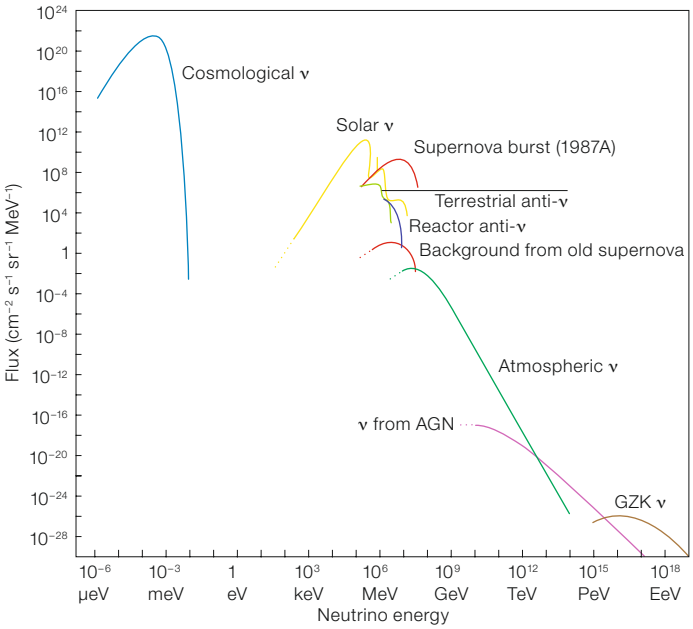

Figure 2: The 'grand unified' neutrino spectrum.

Proton decay and low-energy neutrino astronomy

Grand Unified Theories (GUTs) of particle physics predict that the proton has a finite lifetime. The related physics may be closely linked to the physics of the Big Bang and the cosmic matter-antimatter asymmetry. Data from the Super-Kamiokande detector in Japan constrain the proton lifetime to be larger than 10^{34} years, tantalisingly close to predictions of various GUT models. A sensitivity improvement of an order of magnitude requires detectors on the 10^5–10^6 ton scale.

Proton decay detectors do also detect cosmic neutrinos. Figure 2 shows a 'grand unified neutrino spectrum'. Solar neutrinos, burst neutrinos from SN 1987A, reactor neutrinos, terrestrial neutrinos and atmospheric neutrinos have been already detected. They would be also in the focus of a next-stage proton decay detector. Another guaranteed – although not yet detected – flux is that of neutrinos generated in collisions of ultra-energetic protons with the 3-K cosmic microwave background (CMB), the so-called GZK (Greisen-Zatsepin-Kuzmin) neutrinos. Whereas GZK neutrinos as well as neutrinos from active galactic nuclei (marked AGN) will likely be detected by neutrino telescopes in the next decade (see below), no practicable idea exists how to detect 1.9 K cosmological neutrinos, the analogue to the 2.7 K microwave radiation.

A next-generation proton decay detector could record neutrinos from a galactic supernova with unprecedented statistics: 10^4–10^5 events, compared to only 20 events for SN 1987A. It would also allow a precise study of the solar interior and of neutrinos generated deep in the Earth. Three detection techniques are currently studied: Water-Cherenkov detectors (like Super-Kamiokande, see de Bellefon et al. 2006), liquid scintillator detectors and liquid argon detectors. They will be evaluated in the context of a common design study which will also address the underground infrastructure and the possibility of detecting neutrinos from future accelerator beams. This design study should converge, on a time scale of 2010, to a common proposal. The total cost depends on the method and the actual size, and is estimated between 400 and 800 M€. With the start of civil engineering in 2012 or 2013, only a third of this amount might be due before 2016.

Neutrino properties: neutrino-less double beta decay

In the context of astroparticle physics, neutrinos – rather than being the subject of research – mainly play the role of messengers: from the Sun, from a supernova, from active galaxies. Still, some of their properties remain undetermined. From the oscillatory behaviour of neutrinos we can deduce that the masses of the three neutrino species differ from each other. But what are the absolute values of their masses? Further: are neutrinos their own antiparticles ('Majorana particles')? Specifically these two questions could be answered by the observation of a radioactive decay called neutrino-less double beta decay (Vogl 2006). To reach the sensitivity for a mass range of 20–50 meV, as suggested by various theoretical models, one needs detectors with an active mass of the order of one ton, good resolution and very low background. Construction of such detectors is envisaged to start in 2013–2015. Different nuclear isotopes and different experimental techniques are needed to establish the effect and extract a neutrino mass value. The price tag for one of these experiments is at the 50–200 M€ scale, with the large range in cost being due to the production cost for different isotopes.

The high-energy Universe

Cosmic rays have been discovered nearly a century ago. Some of these particles have breathtaking energies – a hundred million times above that of terrestrial accelerators (Olinto 2007; Watson 2005), see Figure 3. How can cosmic accelerators boost particles to these energies? What is the nature of the particles? The mystery of cosmic rays is going to be solved by an interplay of detectors for high-energy *gamma rays, charged cosmic rays and neutrinos*.

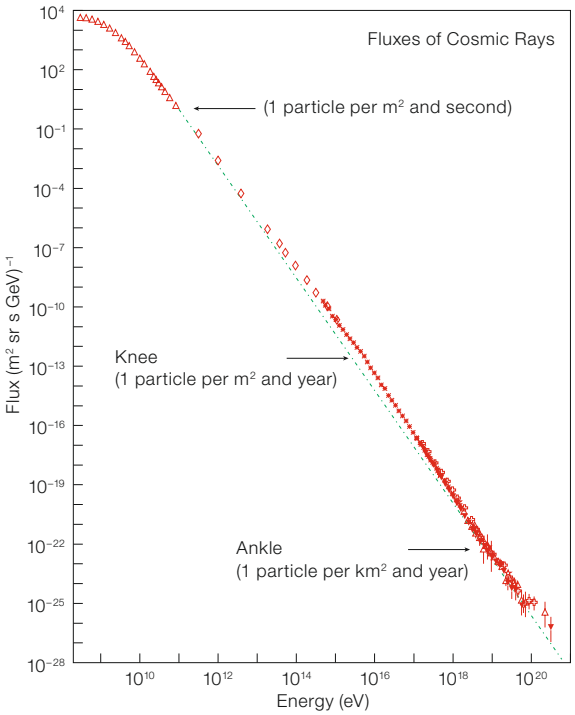

Figure 3: The spectrum of cosmic rays and the domains for various experimental methods. Highest observed energies dwarf the Large Hadron Collider at CERN which will accelerate protons to 10^{13} eV.

Charged cosmic rays

The present flagship in the search for sources of ultra-high energy cosmic rays is the Southern Pierre Auger Observatory in Argentina. This is a 1000-km^2 array of water tanks, flanked by air fluorescence telescopes, which measure direction and energy of giant air showers (see Figure 4). Full-sky coverage would be obtained by a Northern observation site. European groups will play a significant role to establish the scientific case, and after its consolidation make a significant contribution to the design and construction of Auger-North.

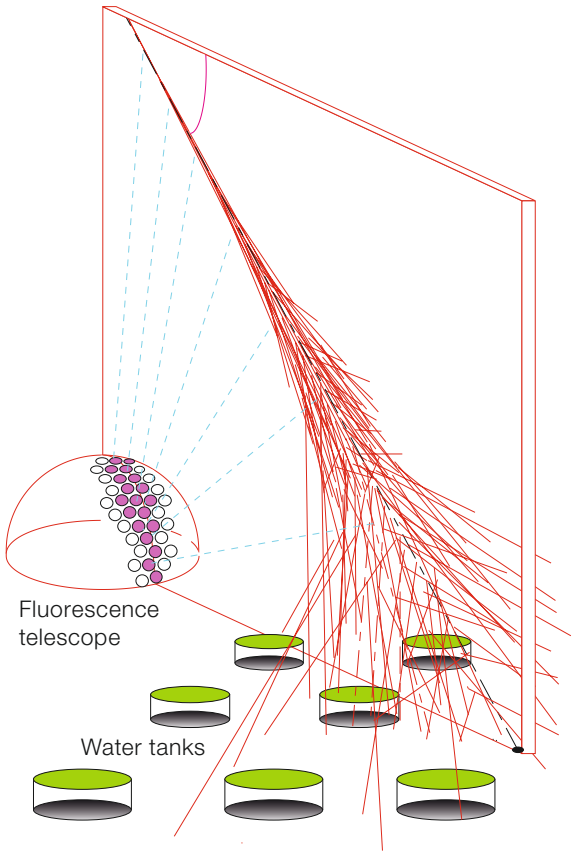

Figure 4: The Auger detection principles: fluorescence light from air showers is recorded by telescopes, particles at ground level are recorded by Cherenkov water tanks.

TeV gamma rays

European instruments are leading the field of ground-based high-energy gamma-ray astronomy. Most of the new sources in Figure 1 have been estalished by H.E.S.S., an array of four Cherenkov telescopes in Namibia, and MAGIC, a large twin telescope at La Palma. The rich results from current instruments (Aharonian 2007; Voelk 2006) show that high-energy phenomena are ubiquitous in the sky; in fact, some of the objects discovered emit most of their power in the gamma-ray range and are barely visible at other wavelengths ('dark accelerators'). The need for a next-generation instrument is obvious, and its required characteristics are well understood. CTA, the Cherenkov Telescope Array, could both boost the sensitivity by another order of magnitude and enlarge the usable energy range. CTA is conceived to cover both hemispheres, with one site in

each. The instruments will be prepared by a common European consortium.

High-energy neutrinos

The physics case for high-energy neutrino astronomy is obvious: neutrinos can provide an uncontroversial proof of the hadronic character of the source; moreover they can reach us from cosmic regions which are opaque to other types of radiation (Waxman 2007). European physicists have played a key role in construction and operation of the two pioneering large neutrino telescopes, NT200 in Lake Baikal and AMANDA at the South Pole, and are also strongly involved in AMANDA's successor, IceCube (Halzen 2007). A complete sky coverage, in particular of the central parts of the Galaxy with many promising source candidates, requires a cubic kilometre detector in the Northern hemisphere. Prototype installations of AMANDA size are presently installed at three different Mediterranean sites (Greece, France, Italy). An EU-funded three-year study (KM3NeT) is in progress to consolidate the scientific case and to work out the technical design of a single, optimised large future research infrastructure in the Mediterranean, with construction envisaged to start in 2011.

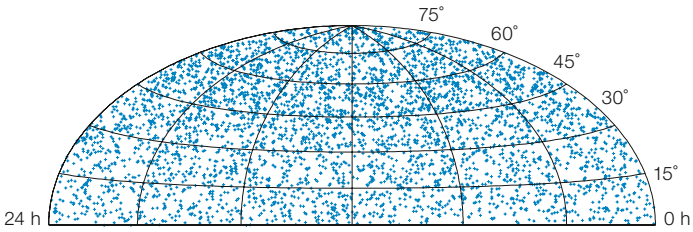

Figure 5: Sky map of 4282 events recorded by AMANDA in 2000–2004.

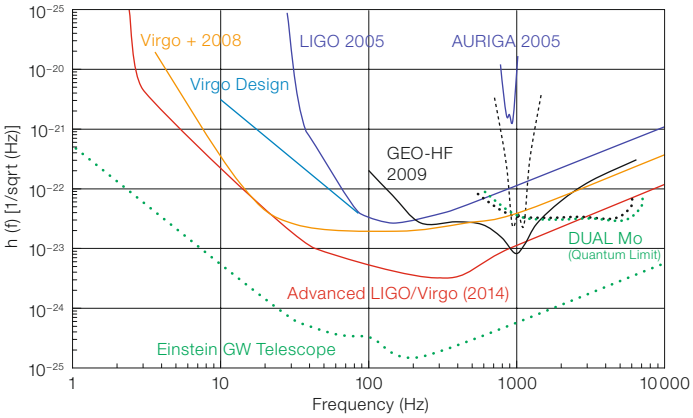

Figure 6: Current and expected sensitivities for ground-based gravitational wave detectors. The solid curves correspond to existing detectors and their expected upgrades. Dotted lines are for new projects.

Gravitational waves

Gravitational waves would provide us with information on strong field gravity through the study of immediate environments of black holes. The most advanced tools for gravitational wave detection are interferometers with kilometre-long arms. The passage of a gravitational wave differential contracts space along the two directions of the arms and influences the light travel time (Hong 2005). At present, the world's most sensitive interferometer is LIGO (USA), the others being GEO600 in Germany, TAMA in Japan and VIRGO in Italy. The research field of Gravitational Wave has a huge discovery potential but is still awaiting the first direct detection. In the short term, the European ground interferometers (GEO and VIRGO) should turn to observation mode with a fraction of their time dedicated to their improvement (GEO-HF, VIRGO+ and Advanced VIRGO). Predicted event rates, e.g. for mergers of neutron star/ black hole systems (BH-BH, NS-NS, NS-BH) are highly uncertain and range between 3 and 1000 for the 'advanced' detectors planned to start data taking in about five years (see Figure 6). This would change dramatically with a third-generation underground interferometer facility (Einstein Telescope, E.T.) which would have a guaranteed rate of many thousands of events per year and move gravitational wave detectors into the category of astronomical observatories. Civil engineering could start in 2012 or 2013.

The big picture

Table 1 is based on a scenario where the process of cooperation and coordination converges to a few major activities (cost > 50 M€) between 2010 and 2015. Naturally, there must be room for initiatives below the 50 M€ level. The Roadmap committee suggests that about 15–20 % of astroparticle funding should be reserved for smaller initiatives, for participation in overseas experiments with non-European dominance, and for R&D. Technological innovation has been a prerequisite of the enormous progress made over the last two decades and enabled maturity in most fields of astroparticle physics. It is also a prerequisite for future progress towards greater sensitivity and lower cost and must be supported with significant funds.

The present 'first stage' roadmap will be followed by a second stage which will be associated with a detailed census of existing budget and human resources available in the participating agencies.

References

Aharonian F. 2007, Science 315, 70
Baudis L. 2005, astro-ph/0511805
de Bellefon A. et al. 2006, hep-ex/0607026
Halzen F. 2007, Science 315, 66
Hong J., Rowan S. and Sathyaprkash B. 2005, gr-qc/0501007
Olinto A. 2007, Science 135, 68
Sadoulet B. 2007, Science 315, 61
Watson A. 2005, astro-ph/0511800
Voelk H. 2006, astro-ph/0603501
Vogl P. 2006, hep-ph/0611243
Waxman E. 2007, Science 315, 63

Field	Experiment	Cost scale per experiment (M€)	Desirable start of construction	Remarks
Dark Matter	Low background experiments with one-ton mass	60–100	2011–2013	two experiments (different nuclei and different techniques)
Proton decay and low-energy neutrino astronomy	Large infrastructure for p-decay and ν astronomy on the 100 kton–1 Mton scale	400–800	Civil engineering: 2012–2013	– needs huge excavation – most of expenditures likely after 2015 – worldwide sharing
Properties of neutrinos	Experiments on neutrinoless double beta decay with one-ton mass	50–200	2013–2015	two experiments with different nuclei (desirably more worldwide)
The high-energy Universe	*Gamma rays:* Cherenkov Telescope Array CTA	100 (South) 50 (North)	First site in 2011	Physics potential well defined by rich physics from present gamma ray experiments
	Charged Cosmic Rays: Auger North	85 (1/3 Europe)	2010	Confirmation of physics potential from Auger South results expected in 2007
	Neutrinos: KM3NeT	250	2011	Confirmation of physics potential expected from IceCube and gamma ray telescopes. Full Proposal expected in 2009.
Gravitational waves	Einstein Telescope	300	Civil engineering: 2012	Conceived as underground laboratory

Table 1: Future European projects with > 50 M€ estimated cost. Note that in most of the cases further R&D efforts, or further input from prototype devices, or final confirmation of the physics case, are required before arriving at a detailed technical proposal. Therefore the indicated starting dates are termed 'desirable'.

Photo: H.E.S.S. Collaboration

Two of the four H.E.S.S. Cherenkov telescopes for detection of very high energy gamma rays are shown. The H.E.S.S. observatory is situated in Namibia, southern Africa. Each telescope has a mirror diameter of 12 m with a camera consisting of 960 photomultipliers. The four telescopes are coupled and work in stereoscopic mode.

Hot Gas in High-Redshift Protogalaxies: Observations of High-Ion Absorption in Damped Lyman-Alpha Systems

Andrew J. Fox[1]
Patrick Petitjean[1,2]
Cédric Ledoux[3]
Raghunathan Srianand[4]

[1] Institut d'Astrophysique de Paris, Université Pierre et Marie Curie, Paris, France
[2] LERMA, Observatoire de Paris, France
[3] ESO
[4] Inter-University Centre for Astronomy and Astrophysics – IUCAA, Ganesh Khind, Pune, India

The neutral discs of high-redshift galaxies give rise to the Damped Lyman-α (DLA) systems seen in the spectra of background quasars. We show for the first time that a hot phase of gas is present in DLAs, observable in the absorption lines of five-times-ionised oxygen. This plasma phase, which could harbour a considerable fraction of all the metals produced by star formation at these epochs, can be explained as the feedback from star formation taking place in the neutral discs.

Studying galaxy halos at high redshift

To obtain observations of galaxies at high redshift, one can pursue deep imaging in the optical and infrared, or look for absorption-line signatures in the spectra of background QSOs. These two methods are complementary, but whereas direct imaging is biased towards bright objects, absorption lines select galaxies irrespective of brightness. If the sight line toward a particular QSO intersects the neutral disc of a galaxy, a Damped Lyman-α (DLA) absorption system will be observed in the quasar spectrum. This name reflects the strong damping wings of the Lyman-α transition seen in these systems. Observationally, DLAs are defined as those QSO absorbers with HI column densities $N(\mathrm{HI}) > 2 \times 10^{20}$ cm^{-2}. Those absorbers with slightly lower HI column densities (between 10^{19} and 2×10^{20} cm^{-2}) are referred to as sub-DLAs. DLAs represent the largest reservoirs of neutral gas (and hence fuel for star formation) in the redshift range 0–5 (see review by Wolfe et al. 2005). Since the advent of 10-m-class telescopes, the chemical content of DLAs and sub-DLAs at high redshift has been carefully studied, providing a means to trace the process of cosmic metal enrichment over a large fraction of the age of the Universe.

We recently began a programme to look for a hot ionised medium in DLAs and sub-DLAs. Two separate processes could create such a medium, we reasoned. If DLAs do represent high-redshift galaxies, then star formation and subsequent Type II supernova explosions will create super-bubbles of hot, shock-heated interstellar plasma. Sufficiently powerful supernovae can drive winds that enrich the surrounding intergalactic medium with metals. The separate process of accretion and shock-heating of infalling intergalactic gas could also lead to the production of a hot ionised medium, though this process is predicted to be less important at high redshift: hydrodynamical simulations have shown that the fraction of all baryons in the temperature range 10^5 to 10^7 K rises from a few per cent at $z = 3$ to ≈ 30 % at $z = 0$ (Davé et al. 2001).

The ultraviolet (UV) lines available for studying highly ionised interstellar plasma are the OVI λλ 1031, 1037, NV λλ 1238, 1242, CIV λλ 1548, 1550, and SiIV λλ 1393, 1402 Å doublets. OVI, which traces gas in the temperature range 10^{5-6} K, is of particular interest since it is the most highly ionised of all the species with UV lines. Furthermore, oxygen is the third most abundant element in the Universe (after hydrogen and helium), and the OVI lines are intrinsically strong, rendering them easy to observe. OVI systems are only accessible from the ground at $z > 2$, where the transitions become redshifted enough to pass the atmospheric cut-off near 300 nm.

Observations and sample selection

A large data set of DLA spectra has been built up using the Ultraviolet-Visual Echelle Spectrograph (UVES) on VLT UT2 in the years 2000 to 2006. The data set currently consists of 123 DLAs and sub-DLAs. We formed two subsamples from the data: all the DLAs with detections in the CIV line, and all the DLAs with detections in OVI. The CIV sample, containing 73 systems, is larger since the lines lie redward of the Lyman-α forest and so are subject to a much lower level of contamination. The OVI sample is much smaller (12 systems), since in many cases the OVI lines are blended with the Lyman-α forest, the series of intervening HI absorption lines found at wavelengths shortward of the quasar's Lyman-α emission line. We dealt with the confusion of separating OVI from HI interlopers by adopting a series of systematic steps to identify genuine DLA OVI absorbers. These steps included verifying the doublet ratio between the two OVI lines, and checking to see whether candidate OVI identifications could be caused by intervening Lyman-α, Lyman-β, or Lyman-γ forest absorbers, by looking in each case for corresponding absorption in the other Lyman series lines. We detect OVI in 12 of 35 DLAs (34 %) with OVI coverage. In the remaining 66 % of cases, we cannot tell whether OVI is present or not due to the blending. Thus a conservative estimate of the fraction of DLAs with OVI is > 34 %. NV is detected in 3/9 systems with data covering the appropriate wavelength range.

Example of DLA spectra

In Figure 1 we show the absorption line profiles of three example DLA systems with OVI detections. Within each column of this figure we show a SiII or FeII line chosen to trace the neutral gas, together with all the available high ionisation data. Our model fits are included on the plot in red. We do not include all the spectra here: the full spectra are available in Figure 1 in Fox et al. (2007a). There is considerable variation in the appearance of the highly ionised absorption lines in the DLAs. The OVI absorbers range from cases with a single, optically thin component to cases with a series of saturated components. The CIV profiles range from cases with one or two components spanning < 100 km s^{-1} to cases with over 15 components spanning several hundred km s^{-1}. It is interesting to note that the mean integrated OVI column density in our 12 detections, $\log N(\mathrm{OVI}) = 14.54$, is of similar order to the mean OVI column density seen in the halo of the Milky Way, even though the metallicities of the DLAs in our sample are typically only one-fortieth of the solar value. This implies that the total ionised hydrogen column densi-

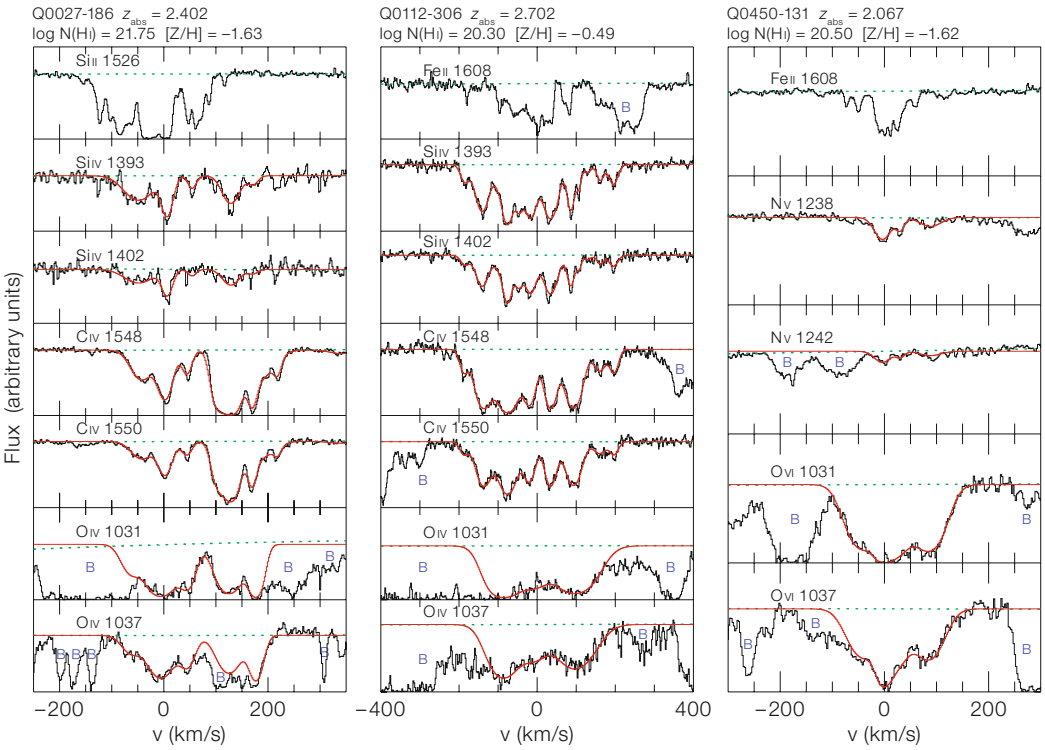

Figure 1: VLT/UVES absorption-line spectra of three example DLA systems with detections of OVI absorption. The tracer of the neutral gas is shown in the top panel, with the other panels showing all available high-ionisation data. In each DLA v = 0 km/s is defined by the redshift annotated at the top of the column, which corresponds to the strongest component of absorption in the neutral gas. The red line shows our VPFIT model of the absorption, and fitted continua are shown as light dashed lines. Blends are identified with the letter 'B'.

ties are much higher in DLAs than in the Milky Way.

Gas temperature

In each DLA, the absorption line profiles of each high-ionisation line usually consist of several individual components. Using the freely available VPFIT software package, we determined the properties of each individual component for the OVI sample. In Figure 2 we show the distributions of the component line width, and compare the results for OVI, CIV, and SiIV. These distributions offer information on the physical conditions in the absorbing gas.

Many of the CIV and SiIV components in DLAs have narrow line widths (b < 10 km s^{-1}) implying that the kinetic temperature in the gas is too low to produce the high ionisation by collisions with electrons. Instead, these components must be photoionised, by extreme-ultraviolet (EUV) photons in the extragalactic background radiation from quasars and galaxies, and potentially also from local sources of radiation. However, no individual narrow photoionised OVI components are found in the data; the narrowest OVI b-value is 14 km s^{-1}, with the majority of cases over 20 km s^{-1}. This suggests that the plasma has a multi-phase structure, with the OVI arising in a hot, collisionally ionised phase, and the narrow CIV components arising in cooler clouds, which may be embedded in the hot phase.

Evidence for star formation

We find that the bulk properties of the plasma depend strongly on the metallicity of the neutral gas. This is revealed by the detection of correlations between [Z/H] and: (1), CIV column density; (2) total CIV line width; and (3), maximum CIV velocity. These correlations are shown in Figure 3.

Similar trends are found with OVI, but we display the CIV results since the sample sizes are much larger and the correlations are more significant. We interpret these correlations as providing evidence for star formation in the DLA host galaxies. In this picture, star formation in the neutral DLA discs will lead to EUV radiation from hot stars that can photoionise carbon in the galaxy's interstellar medium (ISM) to the triply-ionised state, giving rise to the narrow CIV lines. Star formation also leads to supernovae, resulting in: (i) the release of metals generated by stellar nucleosynthesis; (ii) the production of superbubbles containing million-degree plasma, that can interact with cool or warm clouds to produce gas at temperatures where triply-ionised carbon and

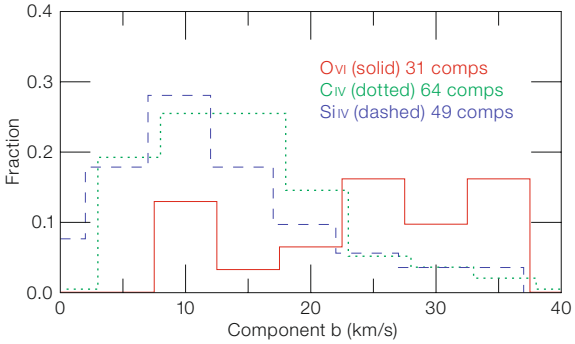

Figure 2: Normalised histograms of the widths of the high-ionisation components that comprise the DLA absorbers, as measured using the VPFIT component-fitting software package. The number of components in each sample is indicated on the plot. Note that $\overline{b}$ (SiIV) < $\overline{b}$ (CIV) < $\overline{b}$ (OVI), i.e. the average component width rises with ionisation potential.

five-times-ionised oxygen are created through electron collisions, giving rise to the broad C IV and O VI lines; and (iii) the deposition of mechanical energy into the surrounding ISM, that imparts the large velocity dispersion to the highly-ionised components.

Our C IV line width/metallicity correlation closely follows the observed correlation between the low-ionisation line width and metallicity (Ledoux et al. 2006) which has been taken to imply an underlying mass-metallicity relation. This is because the low-ionisation line width is thought to be dominated by gravity, and hence can be used to indicate the galaxy mass. If this is true, one expects that the more metal-rich galaxies will reside in deeper potential wells, so that their ionised outflows do not become winds and escape, but rather are decelerated and exist in gravitationally-bound halos. Indeed, this mechanism has been suggested to be the origin of the mass-metallicity relation. However, we detect C IV outflows in DLAs at all values of [Z/H], as shown in the bottom panel of Figure 3. The maximum outflow velocities reach over 500 km s^{-1} in eight high-metallicity systems. This indicates that some mechanism is capable of driving galactic winds even out of the deepest potential wells.

Total ionised column density

By making corrections for ionisation and for metallicity, we can convert, for each absorber, the measured O VI and C IV column densities to H II column densities. The ionisation corrections are derived from models, and the metallicities have been measured in Ledoux et al. (2006). We assume that the neutral, warm, and hot phases all share the same common metallicity, and further that the relative elemental abundances are in their solar ratios. When the hot hydrogen column densities are computed, the numbers are strikingly large. We find log N(H II) in the O VI phase ranges from > 19.5 to > 21.1, and log N(H II) in the C IV phase ranges from > 18.4 to > 20.9. These lower limits are typically on the same order as the H I column in the neutral gas, although we observe a considerable dispersion (over two orders of magnitude) in the value of N(H II)/N(H I).

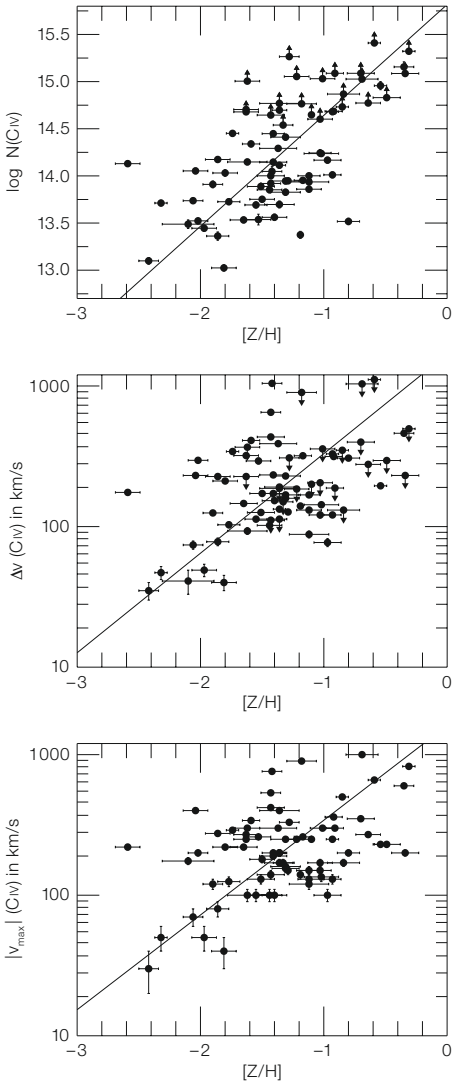

Figure 3: Correlations between metallicity and (1) high ionisation species column density (top panel, > 6 σ significance), (2) high ionisation line width (middle panel, at 3.4 σ significance), and (3) maximum outflow velocity (bottom panel, at 3.1 σ significance), in a sample of 73 DLAs and sub-DLAs. The metallicity is measured in the neutral phase of the gas. The solid lines show linear least-squares bisector fits to the data.

Contribution to Ω

The contribution of H I in DLAs to the cosmic density has been calculated as ≈ 1 × 10^{-3}, fairly flat with redshift (Prochaska et al. 2005). By making use of our new estimates for the amount of ionised gas that accompanies the neutral gas in DLAs, we can compute the contribution of the hot gas in DLAs to the closure density. This calculation has the advantage of not depending on the distribution of gas within the DLA halos. When using our median values N(H II, Hot)/N(H I) > 0.4 and N(H II, Warm)/N(H I) > 0.1, we find that the contribution from the hot and warm ionised phases in DLAs to Ω is > 4 × 10^{-4} and > 1 × 10^{-4}, respectively. These numbers are small compared to the total density of baryons, since at $z > 2$ the majority of the baryons are thought to lie in the diffuse Lyman-α forest (Rauch et al. 1998).

Missing metals

Although the DLAs are unimportant in the baryon budget at high redshift, they may play a significant role in the metal budget. The total amount of metals released by $z = 2$ can be calculated by integrating the observed star-formation history of the Universe, and using the metal yields from models of stellar nucleosynthesis. Using the star-formation rate from Bouwens et al. (2004), the resulting number expressed in units of the critical density is $\Omega_Z^{SFH} \approx 3 \times 10^{-5}$. Stars in galaxies appear to contain ≈ 20 % of the total, the contribution from the ISM in galaxies (H I in DLAs) is ~ 1 %, and the IGM contains a further ≈ 5–25 %. The remaining metals (≈ 50 % of the total) are yet to be found, leading to a situation referred to as the "missing metal problem" (Bouché et al. 2007, and references therein). Hot, low-metallicity, low-density gas is a possible solution to the missing metals problem. For plasma with a density of 10^{-3} cm^{-3}, a metallicity of 0.01 solar, and a temperature of 10^6 K, we calculate the cooling time to be ≈ 12 billion years, i.e. approximately the Hubble time, showing that gas and metals can become essentially locked up in hot halos.

If f (O VI) in the DLA plasma were as low as 3 × 10^{-3}, which is the case for plasma in collisional ionisation equilibrium at 10^6 K (Gnat and Sternberg 2007), then the O VI-bearing plasma around DLAs would contain enough metals to solve the missing metals problem. The widths of the broader O VI lines in our sample are consistent with the thermal broadening expected at 10^6 K. However, since metals will also be found in both the neutral and ionised phases of other categories of quasar absorption line system, it is unlikely that f (O VI) will take a value as low

as 3×10^{-3}. These other categories include the low HI column density absorbers known as Lyman Limit Systems, which may probe the remotest regions of galactic halos. Further studies are needed to search for and characterise the OVI phase in QSO absorbers over all ranges of N(HI), in order to fully measure the quantity of baryons and metals hidden in hot galactic halos at high redshift.

We conclude by noting that if 10^6 K gas is present in DLAs, the majority of oxygen atoms will be ionised up to OVII and OVIII. The resonance lines of these ions are in the X-ray, but unfortunately searches for OVII and OVIII absorption in DLAs to confirm the presence of 10^6 K plasma are beyond the capabilities of current X-ray satellites, and must wait for a new generation of X-ray satellites (*XEUS, Constellation-X*).

Acknowledgements

Andrew J. Fox gratefully acknowledges support from a Marie Curie Intra-European Fellowship awarded by the European Union Sixth Framework Programme. We have made use of the VPFIT software package, written by Bob Carswell and available at *http://www.ast.cam.ac.uk/rfc/vpfit.html*. Patrick Petitjean and Raghunathan Srianand gratefully acknowledge support from the Indo-French Centre for the Promotion of Advanced Research (Centre Franco-Indien pour la Promotion de la Recherche Avancée) under contract No. 3004-3. For complete details on the work discussed in this letter, see Fox et al. (2007a, b).

References

Bouché N. et al. 2007, MNRAS 378, 525
Bouwens R. J. et al. 2004, ApJ 616, L79
Davé R. et al. 2001, ApJ 552, 473
Fox A. et al. 2007a, A&A 465, 171
Fox A. et al. 2007b, A&A, in press, astro-ph/0707.4065
Gnat O. and Sternberg A. 2007, ApJS 168, 213
Ledoux C. et al. 2006, A&A 457, 71
Prochaska J. X. et al. 2005, ApJ 635, 123
Rauch M. 1998, ARA&A 36, 267
Wolfe A. M. et al. 2005, ARA&A 43, 861

The diffuse HII region N158 in the Large Magellanic Cloud, first classified by Henize in 1956, is shown in this ESO 2.2 WFI image taken from the 256 M pixel colour image which appeared as ESO PR 50/06. The image size is 13 by 14.5 arcminutes and north is up, east to the left. The superbubble nebula to the north-west (NGC 2081) surrounds the early-type star cluster LH104, identified by Luck and Hodge in 1970. The more compact nebula to the south-west is NGC 2074, also referred to as N158C, which shows signs of recent star formation. There are many young hot stars and Wolf-Rayet stars found across the N158 nebula.

The Redshift of BL Lacertae Objects from High Signal-to-Noise VLT Spectra

Renato Falomo[1]
Aldo Treves[2]

[1] INAF – Osservatorio Astronomico di Padova, Italy
[2] Università dell'Insubria, Como, Italy

BL Lacertae objects are active galactic nuclei dominated by non-thermal continuum emission and characterised by absence or extreme weakness of emission lines. These properties in several cases hinder the determination of their distance and thus the assessment of the properties of the class. High signal-to-noise optical spectra of these sources obtained with the VLT help to overcome these difficulties and allow one to obtain new redshifts and set stringent limits on the distance for pure lineless objects.

The class of BL Lac objects

The absence or weakness of emission lines in the optical spectra is one of the defining characteristics of BL Lac objects, together with the high polarisation, large amplitude and rapid flux variability. The standard interpretation of these properties, originating from Blandford and Rees back in 1968, is that BL Lacs are radio loud active galactic nuclei (AGN) where the relativistic jet is pointing close to the observer direction, so that the continuum emission is significantly enhanced and the line equivalent width is depressed. BL Lacs therefore offer one of the best opportunities to study relativistic jets, which are manifest from the radio-band to 100 MeV gamma-rays. The atmospheric Cherenkov technique has demonstrated that BL Lacs may emit also in the TeV band. These extremely energetic photons interact with the Extragalactic Background Light (EBL), producing electron/positron pairs. This effect limits the direct detection of such photons to relatively nearby objects ($z < 0.5$).

In the picture of the dominance of relativistic jet emission, though weak, various types of lines are expected: (1) fluorescence emission typical of AGN; (2) stellar absorption of the host galaxy; (3) absorption in the haloes of intervening galaxies.

The first two effects may yield directly a redshift z of the object, while the third gives only a lower limit to z.

Because of the difficulty of observing spectral features, alternative procedures for distance estimates have been proposed. One is based on the observed properties of the host galaxy (imaging redshift). This follows from the fact that, at least locally, the host galaxies are all giant ellipticals with a rather narrow distribution in absolute luminosity (Sbarufatti et al. 2005b). Recently the absorption in the TeV band due to EBL has been also used as a redshift probe (Aharonian et al. 2006; Albert et al. 2007).

Because of the imminent launch of the gamma-ray satellites AGILE and GLAST, and of the flourishing of TeV astronomy (HESS, MAGIC, CANGAROO, VERITAS), one expects a substantial increase in the number of BL Lac object candidates. The measurement of their redshift becomes mandatory, since it is not only an important step for the study of the cosmological evolution of the class, but also for tracing the interaction with the host galaxy, and for probing of the EBL.

Motivated by the above considerations we have undertaken a programme of spectroscopic observations of BL Lac objects using the capabilities of the VLT. The main advantage of these observations with respect to previous programmes is the significant improvement in terms of the signal-to-noise (S/N) of the spectra that directly translates into a better capability to detect very weak spectral features, and largely overcomes the results obtained with four-metre-class instruments. This programme makes feasible the redshift detection of faint sources at $z \sim 1$ and beyond, and of relatively nearbyand bright ones, where the beaming effect on the continuum emission is such that spectral lines can be unobservable.

Observations and data analysis

Optical spectra were collected in service mode with FORS1 on the VLT. The observations were obtained in service mode from April 2003 to March 2004 with UT1 and from April to October 2004 with UT2. We used the 300 V + I grism combined with a 2″ slit, yielding a dispersion of 110 ˚A/mm (corresponding to 2.64 Å/pixel) and a spectral resolution of 15–20 Å covering the 3 800–8 000 Å interval. The seeing during observations was in the range 0.5–2.5″, with an average of 1″. Detailed information on the observations and the sample objects are given in Sbarufatti et al. (2005a, 2006).

The detection and the measurement of very weak spectral features are difficult to assess because they depend on the choice of the parameters used to define the spectral line and the continuum. In order to apply an objective method for any given spectrum, we evaluate the minimum measurable equivalent width (EW_{min}) defined as twice the rms of the distribution of the EW values measured in 30 Å wide bins from the normalised spectrum (avoiding all strong spectral features).

The procedure for calculating EW_{min} was applied to all featureless or quasi-featureless spectra to find faint spectral lines. All features above the EW_{min} threshold, ranging from 1 Å to 0.1 Å, were considered as line candidates and were carefully visually inspected and measured. Based on the detected lines and the shape of the continuum it is possible to characterise the spectroscopic properties of the objects, confirm or dispute the BL Lac classification and derive new redshifts.

Examples of high S/N spectra of BL Lacs at the VLT

As a direct consequence of the improved signal-to-noise of the optical spectra collected at the VLT, we are able to detect a number of spectral features, either emission from the gas surrounding the nuclear region or absorption lines of the host galaxy. Examples of high S/N VLT spectra are shown in Figures 1 and 2. In the first case (PKS 0808+019) the high S/N spectrum shows clearly two weak emission lines (EW = 3–5 Å) of a moderately

high (z = 1.148) redshift object. In the second case (EXO 00556.4-3838) the spectrum allows us to detect the faint absorption features of the host galaxy.

In a third case we show the spectrum of the BL Lac object PG 1553+11. This is a bright (V = 14) object, which, although studied with the most advanced instrumentation, remains line-less (e.g. Falomo and Treves 1990). No signature of its host galaxy is apparent from the high-resolution HST image (Urry et al. 2000 and Scarpa et al. 2000). In this case the spectrum (see Figure 2) obtained with the VLT, in spite of the high (S/N ~ 300), does not allow to detect either faint emission from the nucleus or absorption from the host galaxy.

Analysis of the BL Lac spectra

The observed spectrum of a BL Lac object is given by the contribution of two main components: (1) a non-thermal emission from the nucleus that can be described by a power law; (2) a thermal component due to the host galaxy. In some cases weak emission lines from the nucleus can be also present. Depending on the relative contribution of the two components, the optical spectrum will be dominated by the non-thermal (featureless) emission or by the spectral signature of the host galaxy. In Figure 3 the combination of the two components is compared with the observed spectra for six objects. The host galaxy magnitude deduced from this decomposition is in good agreement with that deduced directly from the image (Sbarufatti et al. 2005b).

Under the assumption that the host galaxy luminosity is confined in a narrow range (e.g. Sbarufatti et al. 2005b) from the EW limits of spectral features, it is possible to constrain the position of the source on the nucleus-to-host flux ratio (ρ) vs redshift plane. This is illustrated in Figure 4. Using this approach it becomes possible therefore to obtain a lower limit to the redshift for objects with featureless spectra (Sbarufatti et al. 2006). For example in the case of PG 1553+11 (Figure 2) the redshift must be $z > 0.1$.

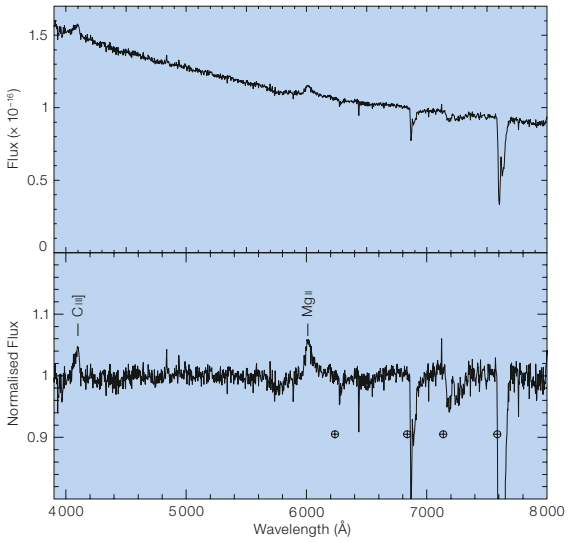

Figure 1a: Optical spectrum of the BL Lac object PKS 0808+019 (z = 1.148). **Top:** Flux-calibrated and dereddened spectra. **Bottom:** Normalised spectrum. Telluric bands are indicated by circled plus signs.

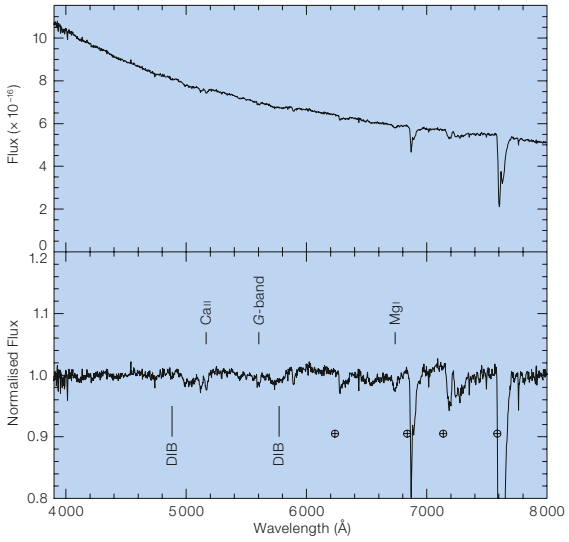

Figure 1b: EXO 00556.4-3838: In this case the spectrum clearly shows the host galaxy spectral features (Ca II 3 934, 3 968, *G*-band 4 305, and Mg I 5 175 Å absorption lines) at z = 0.302. Absorption features in our Galaxy are labelled by DIB (diffuse interstellar band).

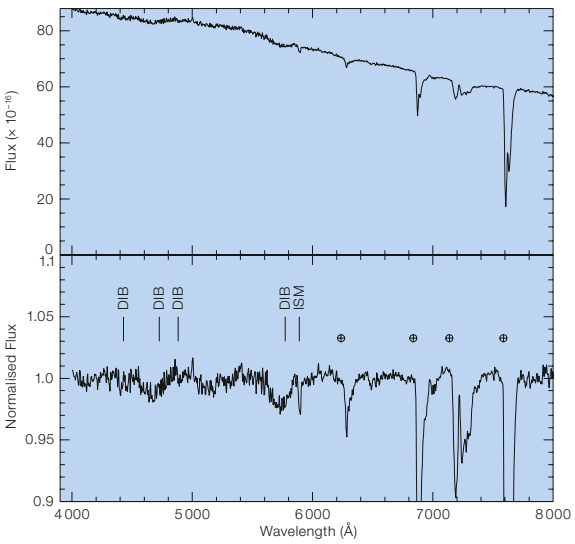

Figure 2: Optical spectrum of the featureless BL Lac object PG 1553+11. **Top:** Flux-calibrated spectra. **Bottom:** Normalised spectra. Telluric bands are indicated by circled plus signs. The other absorption features are identified as interstellar medium (ISM) spectral lines and diffuse interstellar bands (DIB) from gas in our Galaxy.

ZBLLAC – a web page for the spectra of BL Lac objects

The optical spectra of BL Lacs obtained at the VLT have been made available to the astronomical community through a spectroscopic library at the web page: *http://www.oapd.inaf.it/zbllac/index.html*. This includes most of the objects observed at the VLT and others with good quality spectra. For each object in the database we give basic data (coordinates, *V*-band magnitude, the redshift or a lower limit to it), the optical spectrum (in PDF and ASCII table format) and details on the references to the target. In general the best available optical spectrum is linked in the main page of the database, while additional spectra are appended and linked in separate pages. These web pages are also open to external contributions (see *http://www.oapd.inaf.it/zbllac/intro.html* for details).

Acknowledgements

This work was undertaken in collaboration with Boris Sbarufatti (Insubria University, Como), Jari K. Kotilainen (Turku Observatory, Finland) and Riccardo Scarpa (ESO; GTC, Spain).

References

Aharonian F. et al. 2006, A&A 448, L19
Albert J. et al. 2007, ApJ 654, L119
Blandford R. D. and Rees M. J. 1978, in Pittsburgh Conference on BL Lac Objects, ed. A. M. Wolfe, University Pittsburgh Press, 328
Falomo R. and Treves A. 1990, PASP 102, 1120
Sbarufatti B. et al. 2005a, AJ 129, 599
Sbarufatti B., Treves A. and Falomo R. 2005b, ApJ 635, 173
Sbarufatti B. et al. 2006, AJ 132, 1
Scarpa R. et al. 2000, ApJ 532, 740
Urry C. M. et al. 2000, ApJ 532, 816

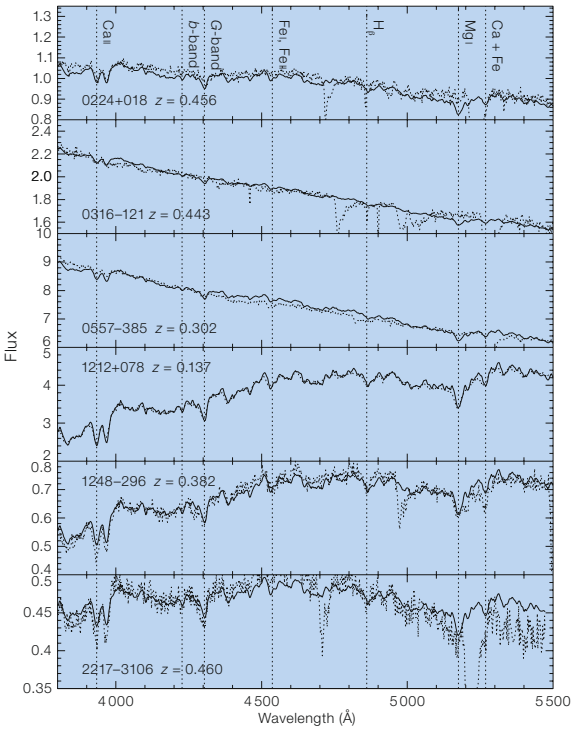

Figure 3: Comparison of the observed optical spectra (dotted line) of BL Lac objects with a best fit model (solid line) composed by a template host galaxy spectrum plus a non-thermal continuum component described by a power law. The figure clearly illustrates the effect on the observed spectrum of the different contributions from the nucleus that occur in 0316–121 and 0557–385.

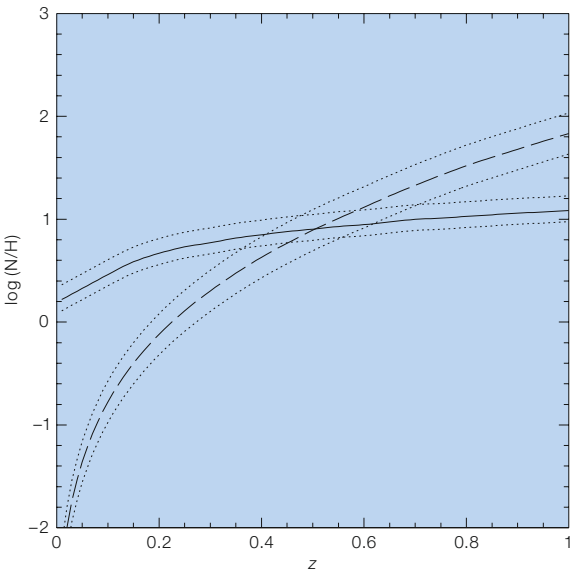

Figure 4: The *R*-band nucleus-to-host ratio (ρ) versus redshift for the BL Lac object 1RXS J150343.0–154107. The solid line represents the limit in this plane obtained from the minimum equivalent width (EW_{min}) that was derived from the VLT spectrum. The bending of this curve at low *z* is due to aperture effects. Dotted curves correspond to a 0.1-Å uncertainty on the EW. The dashed line gives ρ *versus z* for the object with nuclear apparent magnitude R = 17.7 assuming a standard host galaxy ($M_R = -22.9$; Sbarufatti et al. 2005b). Dotted lines encompassing this curve correspond to a variation of 0.5 mag. The intersection of the two solid lines gives the lower limit: $z > 0.5$. Full details on the method are described in Sbarufatti et al. (2006).

Results from the Multiwavelength Survey by Yale-Chile (MUSYC)

Ezequiel Treister[1]
Eric Gawiser[2]
Pieter Van Dokkum[3]
Paulina Lira[4]
Meg Urry[3]
and the MUSYC Collaboration

[1] ESO
[2] Rutgers, State University of New Jersey, Piscataway, New Jersey, USA
3 Yale University, New Haven, Connecticut, USA
4 Universidad de Chile, Santiago de Chile, Chile

We present results from the MUSYC survey, which images a total of 1.2 square degrees spread over four fields in *UBVRIz'K* down to the spectroscopic limit, $R \sim 25$, $K \sim 22$ (AB). A significant fraction of the survey area has also been imaged by Chandra, XMM, GALEX, HST-ACS, near-infrared (JH), Spitzer-IRAC+MIPS, VLA, and ATCA. The main goals of this survey include the study of galaxy formation and evolution, Active Galactic Nuclei (AGN) and Galactic structure.

The MUSYC survey

In recent years, extragalactic astronomy at high redshift has been dominated by deep multi-wavelength surveys. Examples of these surveys are the Hubble Deep Fields and the Great Observatories Origins Deep Survey (GOODS). These are very deep surveys over a relatively narrow area of the sky, ~ 0.2 square degrees or less. These surveys allow us to study sources dimmer than the spectroscopic limit but suffer from significant sample variance, motivating a new generation of wider-area deep surveys that bridge the gap between HDF/GOODS and the shallower wide coverage of the Sloan Digital Sky Survey. The wide/deep surveys allow us to study a fair sample of the Universe at all redshifts $z > 0.5$ and to detect a statistically significant population of the brighter, and thus rarer, sources. Examples include Galaxy Evolution from Morphology and SEDs (GEMS), the VLT-VIRMOS Deep Survey (VVDS), the Cosmic Evolution Survey (COSMOS), the Deep Extragalactic Evolutionary Probe (DEEP-2), the NOAO Deep-Wide Field Survey (NDWFS), and the Multiwavelength Survey by Yale-Chile (MUSYC).

MUSYC is unique among the current generation of wide-deep surveys in having been optimised for the study of the high-redshift ($z > 3$) Universe. This is achieved by imaging 1.2 square degrees spread over four fields down to the spectroscopic limit for modern 8-metre telescopes with coverage from *U*-band through *K*-band, in order to trace both the Lyman and Balmer/4 000 Å breaks at $z \sim 3$ and prioritise high-redshift candidates for spectroscopy. The fields were chosen to have the lowest possible Galactic reddening, HI column density and dust emission at 100 microns. Fields with existing multi-wavelength data were strongly preferred. Additionally, these fields had to be accessible from Chile, as they will be a natural choice for follow-up studies with ALMA.

This programme started as a collaboration between astronomers from Universidad de Chile and Yale University and now includes a total of 30 investigators from Chile, Europe and USA, plus seven Ph.D. students. The first data for this survey were obtained in October 2002 and the primary optical and near-IR imaging programmes are now finished, with follow-up spectroscopy and imaging (medium-band optical, Spitzer, sub-mm) ongoing. All data from this survey will be made public, with reduced images and catalogues already available from the broad-band optical and near-IR imaging. Instructions for download of the data and more information about the survey can be found at the webpage *http://www.astro.yale.edu/MUSYC*.

Optical imaging

Optical imaging was performed mostly using the Blanco 4-metre telescope at Cerro Tololo with the MOSAIC-II camera, which provides a field of view of ~ 36′ × 36′. Images were taken in the *UBVRIz'* filters. This filter set was chosen in order to maximise the number of independent flux measurements and the wavelength coverage. Most of the imaging in the ECDF-S field (except the *z'*-band) and the *U*-band imaging on the SDSS1030 field were done using the Wide Field Imager (WFI) on the 2.2-metre telescope at La Silla. Images in a narrow band filter centred at 500 nanometers were also obtained in each field in order to look for Lyman Alpha Emitters at $z \sim 3$. The ECDF-S imaging was made public by the ESO Deep Public Survey, COMBO-17, and GaBODS teams.

The location of each field together with the magnitude limits on each band is presented in Table 1. Colour images of each field combining data in the *U*, *B* and *R* filters are presented in Figure 1. A detailed description of the data-reduction techniques for the EHDF-S, which were also used for the other fields, was provided by Gawiser et al. (2006a). The 1.2 square degree optical catalogue contains 277 341 sources with a 50 % completeness limit of $R \sim 26.5$.

IR imaging

Information at near-IR wavelengths is very important as these bands provide useful information for photometric redshifts and at the same time trace the rest-frame optical light at high redshift. The near-IR coverage of the MUSYC fields follows two complementary approaches. Each 30′ × 30′ field was covered up to a magnitude limit of $K \sim 22$; this is called the 'wide' survey. Additionally, four 10′ × 10′ regions were observed for longer periods in *JHK* and Spitzer IRAC [3.6, 4.5, 5.8, 8.0 and 24] microns as part of the 'deep'

Field	RA	Dec	*U*	*B*	*v*	*R*	*I*	*z′*	NB500	*J*	*H*	*K*
ECDF-S	03:32:29.0	−27:48:47	26.0	26.9	26.4	26.4	24.6	23.6	25.5	24.3	23.8	23.4
SDSS1030	10:30:27.1	05:24:55	25.7	26.0	26.2	26.0	25.4	23.7	24.8	24.1	23.9	23.3
CW1255+01	12:55:40.0	01:07:00	26.0	26.2	26.1	26.0	25.0	24.1	24.4	24.0	22.8	23.0
EHDF-S	22:32:35.6	−60:47:12	26.0	26.1	26.0	25.8	24.7	23.6	24.1	24.3	23.4	23.4

Table 1: Optical positions and magnitude limits for each of the MUSYC fields. RA is in hours, while Dec is in degrees. Depths are 5σ AB magnitude limits for point sources. Except in ECDF-S, the near-IR depths correspond to the 'deep' survey regions.

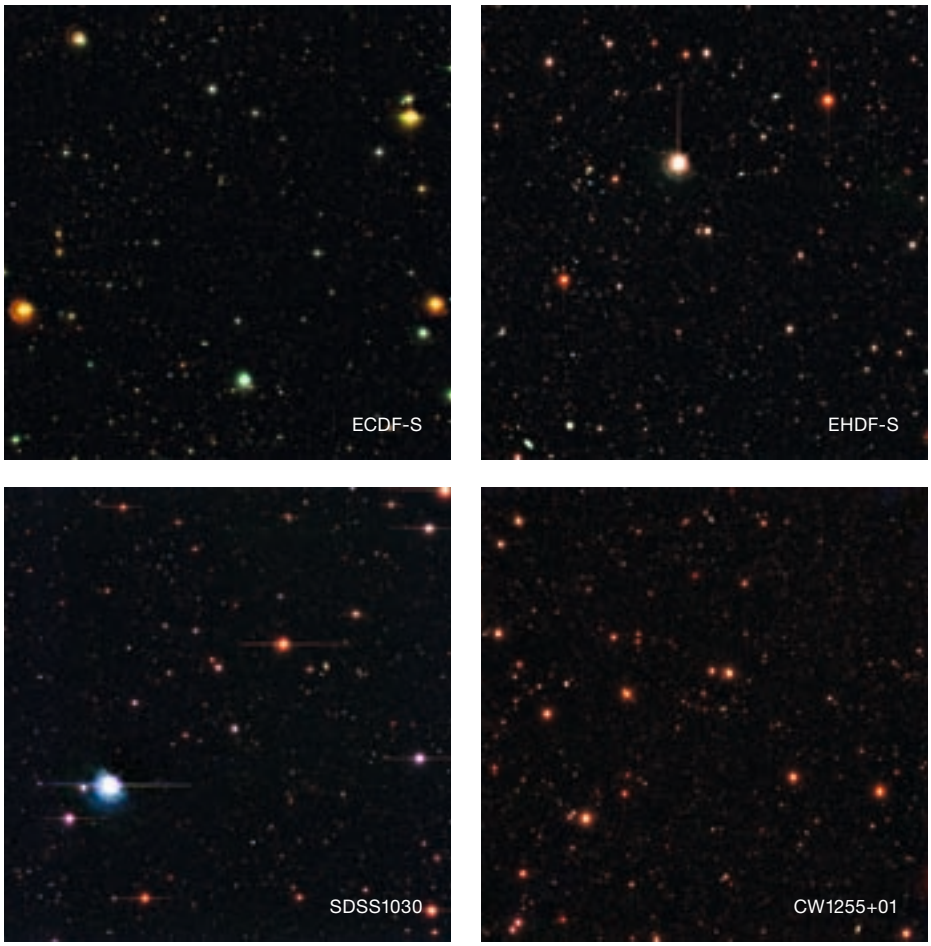

Figure 1: Optical images of the four 30′ × 30′ fields in the MUSYC survey.

survey. Spitzer magnitude limits are AB ~ 23–24 (5σ) at 3.6 and 4.5 microns and ~ 21–22 at 5.7 and 8 microns, while the exposure time in the MIPS 24 micron band is ~ 0.5–1 hour per field. In ECDF-S these data were taken over the full 31′ × 31′ field, with the Spitzer-IRAC coverage comprising a Cycle 2 Legacy Survey (SIMPLE, PI van Dokkum) and the MIPS 24 micron coverage from GTO observations (PI Riecke). The near-IR imaging was obtained using the Infrared Sideport Imager (ISPI) on the CTIO Blanco 4-metre telescope. This detector provides a field of view of 10.5′ × 10.5′, one of the widest field cameras available in the near-IR. In the particular case of the ECDF-S, deep NIR coverage is provided by the GOODS survey, from data obtained using ISAAC at the VLT to depths of *J* ~ 25, *H* ~ 25 and *K* ~ 24. In the EHDF-S, two adjacent deep fields were taken in order to obtain a combined deep field of 19.5′ × 10′. A composite *RJK* image of one of the EHDF-S deep fields is shown in Figure 2. Additional information and a description of the data reduction can be found in Quadri et al. (2007b).

X-ray, UV, and radio imaging

One of our fields is the Extended Chandra Deep Field-South, which includes Chandra imaging over 1 Ms of the famous CDF-S and 250 ks over the 30′ × 30′ region surrounding it. The ECDF-S was also observed with XMM (~ 500 ks), with GALEX in the ultraviolet as part of their deep imaging programme, by the Hubble space telescope Advanced Camera for Surveys (ACS) as part of the GEMS and GOODS surveys, and has received deep radio coverage from VLA and ATCA. The EHDF-S is the region surrounding the Hubble Deep Field South, a well-studied region of the sky including multi-frequency radio imaging by ATCA. The SDSS1030 field was observed by XMM in X-rays for a total of ~ 100 ksec.

Spectroscopic data

An extensive spectroscopic follow-up programme is underway. Optical spectroscopy uses the multiobject spectrographs on 8-metre-class telescopes in order to efficiently reach depths comparable to our photometry. This part of the project uses the Visible Multiobject Spectrograph (VIMOS) at the VLT and the Inamori Magellan Areal Camera and Spectrograph (IMACS) on the Baade telescope at the Las Campanas Observatory. The general MUSYC spectroscopic programme uses medium-resolution grisms, *R* ~ 500 for VIMOS and ~ 1000 for IMACS, since the main goal is to provide redshifts and basic identifications. As it is not possible to obtain spectra for all sources in our fields, only a small fraction, ~ 5 %, of the sources will be targeted. Each mask contains ~ 100 objects selected for specific science goals and is observed for ~ 3–6 hours in order to reach a magnitude limit of *R* ~ 24 in the continuum. Near-IR spectroscopy has been obtained for a sample of ~ 30 high-redshift galaxies using VLT+SINFONI and Gemini-S+GNIRS.

Figure 2: *RJK* composite of one of the 10′ × 10′ deep regions in the EHDF-S. These deep near-IR observations allow for the detection of high-redshift galaxies and highly obscured sources.

Galaxy formation and evolution

Our rich multi-wavelength data set has yielded significant advances in understanding the nature of Lyman-Alpha-Emitting galaxies (LAEs). Our narrowband imaging was used to select a sample of 162 LAEs at $3.08 < z < 3.12$; spectroscopic follow-up determined precise redshifts for 60 of these objects and showed no evidence for contamination from lower-redshift emission-line galaxies (Gawiser et al. 2006b). We measured the continuum and emission-line luminosity functions and found that the LAEs have a median continuum magnitude of $R = 27$ and very blue continuum colours, similar to those of Lyman break galaxies (LBG; see Figure 3). These blue colours and the relative strength of Lyman alpha and ultraviolet continuum emission imply very little or no dust content, consistent with these galaxies being found in the early stages of a burst of star formation. Our full SED analysis (see Figure 4) found rapid star-formation rates (~ 6 $M_\odot$/yr), low stellar masses (~ 10^9 $M_\odot$), and no evidence for a substantial AGN component (only 3/162 LAEs are detected in X-rays). The lack of ultra-high equivalent-widths, as found in $z > 4$ LAEs, argues that the $z \sim 3$ LAEs do not represent primordial Pop III objects.

We have also applied our multi-wavelength data to construct a stellar mass-selected sample of 294 galaxies with $M > 10^{11}$ $M_\odot$ at $2 < z < 3$ (van Dokkum et al. 2006). 70 % of this sample is comprised of the recently-discovered population of Distant Red Galaxies (DRGs) having $J–K > 2.3$ (Vega), and only 20 % have the right rest-frame UV colours to be selected as LBGs. The DRGs represent a mix of passive galaxies, with low star-formation rates (Kriek et al. 2006), and dusty active galaxies, whose 24-micron Spitzer detections imply an average star-formation rate of ~ 130 $M_\odot$/yr (Webb et al. 2006). We measured the rest-frame optical luminosity functions of *K*-selected galaxies at $2 < z < 3.5$ and found a characteristic magnitude ~ 1.2 mags brighter than in the local Universe, but a space density ~ 5 times smaller (Marchesini et al. 2007). The DRGs dominate the stellar mass density of the Universe in this redshift range. A clustering analysis of galaxies with $K < 21$ (Vega) found that they reside in massive dark matter halos of ~ 5×10^{12} $M_\odot$, while the subset of galaxies qualifying as DRGs reside in even more massive halos of ~ 2×10^{13} $M_\odot$ (Quadri et al. 2007a). These halos are sufficiently massive that the typical descendants of *K*-selected galaxies at $z > 2$ will reside in groups and clusters at $z = 0$. Several of the *K*-selected galaxies have been identified as potential AGN hosts based upon their [N II]/H-alpha emission line ratio, and it appears that AGN are preferentially found in the most massive galaxies at $z > 2$ (Kriek et al. 2007).

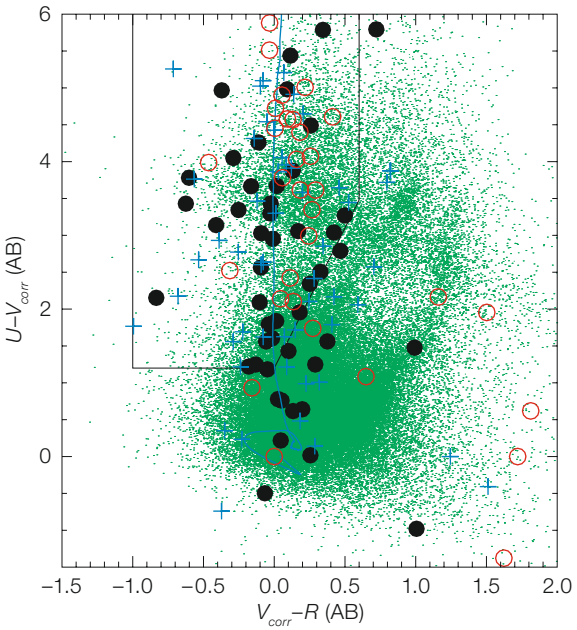

Figure 3: The *U–V versus V–R* colours of LAEs at $z = 3.1$, showing spectroscopically confirmed LAEs (solid circles), objects with insufficient signal-to-noise for spectroscopic classification (open circles), and objects without spectroscopy (crosses). The green dots show the entire 84 410 objects in the optically-selected catalogue of ECDF-S. The polygon is the LBG selection region. The solid blue curve shows the track of an LBG template spectrum, which falls within this selection region at $2.8 < z < 3.4$. The contribution of each LAE's emission line to its *V*-band flux has been subtracted.

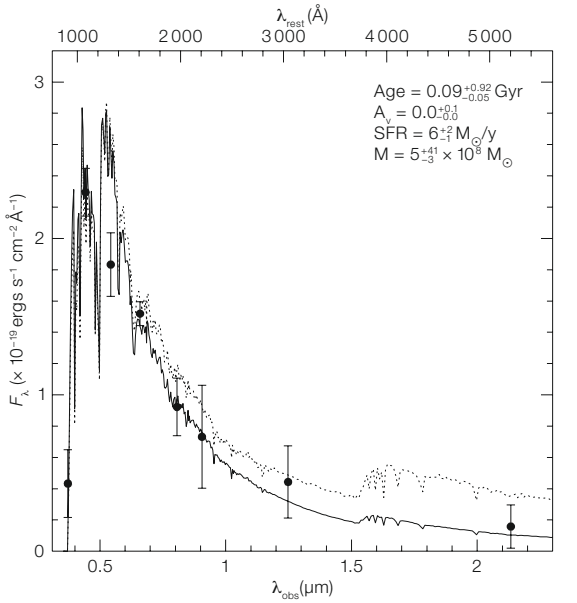

Figure 4: Average *UBVRIzJK* broadband photometry of LAEs from Gawiser et al. (2006b) along with best-fit model from SED fitting (solid), with model parameters listed. The dotted curve shows a maximally old model with stellar population age fixed to 2 Gyr (the age of the Universe at $z = 3.1$).

Given the over 100 000 galaxies at $z < 1$ on the MUSYC fields, all of them with accurate photometric redshifts and many of them with spectroscopic identifications, it is possible to study them in a statistical sense. Using data from three MUSYC fields we have found that the clustering length increases slightly from $z \approx 0.3$ to $z = 0.9$ while the mass of the galaxy host halos are roughly constant at a value of $M_h = 10^{13.5 \pm 1.2}$ $M_\odot$ for galaxies with $M_R < -17$ in the same redshift range. From the GALEX ultraviolet data in the ECDF-S, we can conclude that elliptical galaxies

at $z > 0.5$ still show a significant recent star formation, more than what was originally expected. This amount of star formation remains constant up to $z \sim 1$, contrary to late-type galaxies, which show an increase in the star-formation rate with increasing redshift.

Active Galactic Nuclei (AGN)

In order to correlate the AGN activity with the properties of the supermassive black holes found in the centres of the most massive galaxies, a large unbiased sample of AGN to high redshifts is required. Surveys that rely on the optical properties of AGN (blue continuum, broad emission lines) often miss a large number of sources, those in which obscuration in the line of sight is present. In order to obtain a more complete AGN sample, X-ray and IR observations are critical, as the effects of obscuration are less important at these wavelengths. One of the MUSYC fields, the ECDF-S, was completely covered by Chandra observations. Based on the data analysis and reduction of Virani et al. (2006), 651 unique X-ray sources were found in that field. An identification programme is ongoing using IMACS and VIMOS. So far, ~ 250 X-ray sources have been observed.

Combining the spectroscopic redshifts with the optical, near-IR and X-ray fluxes provides important clues about the AGN population. In Figure 5, we show the hard X-ray luminosity (in the 2–8 keV band) versus 'Hardness ratio' diagram. The hardness ratio, defined as (H–S)/(H+S) where H and S are the count rates in the hard and soft, 0.5–2 keV, bands, is a measure of how hard the observed X-ray spectrum is. As can be seen in that figure, the most luminous sources are in general also harder, and are also classified as unobscured AGN based on their optical properties (presence of broad emission lines). This shows that there are relatively more unobscured AGN at higher luminosities, and, as expected, these sources have softer X-ray spectra, as obscuration makes the observed X-ray spectra harder.

One very interesting class of objects are the Extreme X-ray to Optical sources (EXOs), which are defined as sources with clear X-ray and near-IR detections, but no detectable optical counterpart. Two competing hypotheses have been proposed to explain these sources: either they are at very high redshift, $z > 6$ so that the Lyman break is moved beyond the optical bands; or they are highly obscured AGN at $z \sim 2$–3 with underluminous host galaxies. In either case, given their X-ray fluxes, these sources should host an AGN. In the ECDF-S we found 12 X-ray sources not detected in the combined *BVR* image, but clearly detected in the *K*-band image. Contrary to the sources in the CDF-S proper/GOODS-S field, which are very faint even in the near-IR bands ($K > 21$ mag), our sources are on average brighter, with four of them having $K < 20$ and thus follow-up studies are possible. In particular, our ongoing near-IR spectroscopy programme using Gemini-S+GNIRS and SINFONI at the VLT will provide secure redshifts and confirm the nature of these sources. Currently, no EXO has a measured spectroscopic redshift.

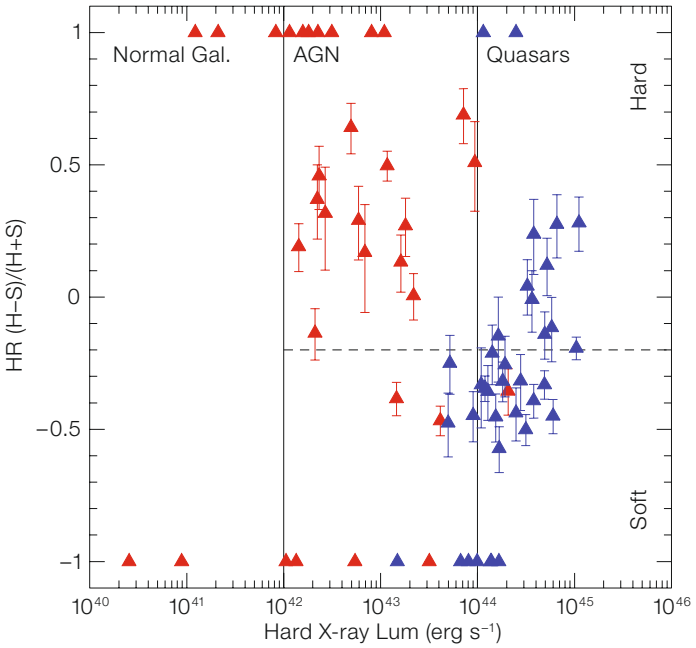

Figure 5: Hardness ratio *versus* hard X-ray luminosity for the sources with measured redshift in the ECDF-S. Blue symbols show the location of the sources classified as unobscured AGN based on their optical spectra (presence of broad emission lines).

The structure of our Galaxy

Unlike most deep surveys, MUSYC has been designed with Galactic science in mind. Multiple epochs of optical imaging are being used to conduct a proper-motion survey to find white dwarfs and brown dwarfs in order to study Galactic structure and the local Initial Mass Function. The Galactic programme also includes the study of stellar statistics. One of the first results was the measurement of the Galactic scale height from a sample of M and K stars selected on the basis of their photometric properties. The Galactic thick disc has a scale height of ~ 900 parsecs, while the halo, which does not have an exponential distribution, has a power law fall-off coefficient of –3.5 to –4.5.

References

Gawiser E. et al. 2006a, ApJS 162, 1
Gawiser E. et al. 2006b, ApJ 642, L13
Kriek M. et al. 2006, ApJ 649, L71
Kriek M. et al. 2007, ApJ, in press, astro-ph/0611724
Marchesini D. et al. 2007, ApJ 656, 45
Quadri R. et al. 2007a, ApJ 654, 138
Quadri R. et al. 2007b, AJ, in press, astro-ph/0612612
Van Dokkum P. G. et al. 2006, ApJ 638, L59
Virani S. et al. 2006, AJ 131, 2373
Webb T. M. A. et al. 2006, ApJ 636, L17

Weighing Ultracompact Dwarf Galaxies in the Fornax Cluster

Michael Hilker[1]
Holger Baumgardt[2]
Leopoldo Infante[3]
Michael Drinkwater[4]
Ekaterina Evstigneeva[4]
Michael Gregg[5]

[1] ESO
[2] Argelander-Institut für Astronomie, Universität Bonn, Germany
[3] Departamento de Astronomía y Astrofísica, Pontificia Universidad Católica de Chile, Santiago de Chile, Chile
[4] Department of Physics, University of Queensland, Brisbane, Australia
[5] Department of Physics, University of California, Davis, California, USA

High-resolution spectra from the Ultraviolet and Visual Echelle Spectrograph (UVES) were used to derive internal velocity dispersions of Ultracompact Dwarf galaxies (UCDs) in the Fornax cluster of galaxies. The velocity dispersions, together with highly spatially resolved luminosity profiles from Hubble Space Telescope imaging (ACS camera), allowed us to derive the dynamical masses of the UCDs. We show that the mass-to-light ratios of UCDs in Fornax are consistent with those expected for pure stellar populations. No dark matter contribution is needed. Thus, these UCDs seem to be the result of star-cluster formation processes within galaxies, rather than being compact dwarf galaxies formed in dark-matter halos.

Dwarf galaxies have only been extensively studied in the last three decades. Dwarf spheroidals are considered to be the faintest galaxies, having baryonic masses comparable to those of bright globular clusters (~ 10^6 $M_\odot$), but are 50–200 times more extended. It has been believed that dwarf galaxies are diffuse structures, with the exception of the compact elliptical M32, a companion of the Andromeda galaxy, which is ~ 8–10 times smaller than dwarf ellipticals of comparable luminosities, but about 150 times more luminous than the brightest globular clusters of the Local Group. The gap in luminosity between globular clusters and compact dwarf galaxies has started to be filled in observationally over the last decade, thanks to several large spectroscopic surveys in nearby galaxy clusters.

Compact objects with masses greater than those of normal globular clusters were only discovered about 10 years ago. In 1999, two bright compact objects were confirmed as members of the Fornax cluster in a spectroscopic survey that was designed as a follow-up of a photometric investigation of dwarf ellipticals in the Fornax cluster (Hilker et al. 1999). One year later, in 2000, a systematic spectroscopic survey within a two-degree field centred on Fornax revealed five compact members in the magnitude range $-13.5 < M_V < -12.0$ (Drinkwater et al. 2000) which were one year later dubbed 'Ultracompact Dwarf Galaxies' (UCDs) by Phillipps et al. (2001). In Figure 1 we show the location of the seven brightest UCDs in the Fornax cluster.

We now know several physical properties of UCDs thanks to significant growth in this research field. After the first discovery of UCDs in the Fornax cluster (summarised in a Nature article by Drinkwater et al. in 2003), many surveys were developed to search for UCDs in different environments and at fainter magnitudes. Bright UCDs were also found in the Virgo cluster, and fainter ones in both clusters. With absolute magnitudes in the range $M_V = -13.5$ to -11.0 they are up to 3 mag brighter than ω Centauri, the most massive globular cluster (GC) of the Milky Way, but about 3 mag fainter than M32. Their sizes are related to their luminosities. Unlike globular clusters which are characterised by a more or less constant size (~ 3 pc half-light radius), the sizes of UCDs increase with luminosity reaching half-light radii of ~ 100 pc. Some of the brighter UCDs exhibit a small low-surface-brightness envelope with extensions up to several hundred parsecs. Most of the brightest UCDs have slightly subsolar metallicities ([Fe/H] ~ −0.5 dex), similar to the 'red', metal-rich bulge GCs of giant galaxies.

In summary, one might say that the name 'ultracompact dwarf galaxies' (UCDs) applies to old stellar systems in the transition region between globular clusters and compact dwarf galaxies.

Formation scenarios for UCDs

An important question that is keeping UCD researchers busy is whether UCDs should be regarded as galaxies or whether they are more closely linked to globular clusters. Various formation scenarios have been suggested that reflect the different viewpoints. The four most promising are:

1. UCDs are the remnant nuclei of galaxies that have been significantly stripped in the cluster environment ('threshing' scenario, e.g. Bekki et al. 2003). Good candidates for isolated nuclei in the local environment are the Galactic globular clusters ω Centauri and the giant star cluster G1 in Andromeda.

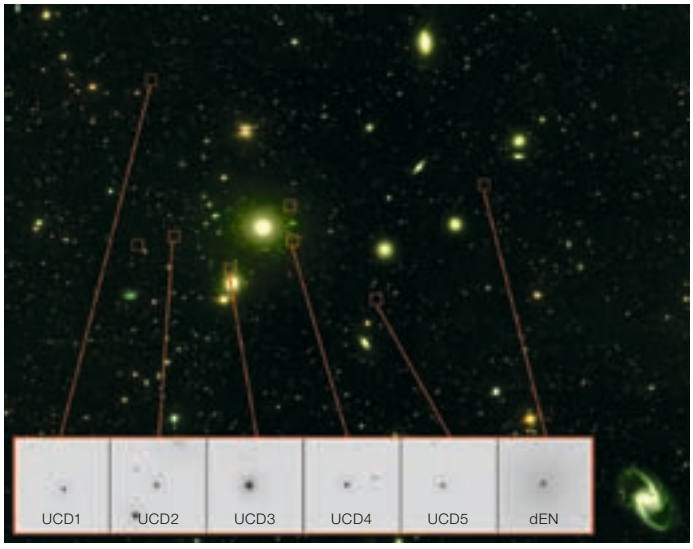

Figure 1: Panoramic view of the Fornax cluster with its population of UCDs. The background image was taken with the Michigan Curtis Schmidt Telescope at the Cerro Tololo Observatory. Insets are HST/STIS images of five UCDs in Fornax and a nucleated dwarf elliptical galaxy in Fornax (far right).

If this formation channel is viable one would not expect a dark matter component in UCDs since 'threshing' simulations show that the dark matter halo of dwarf galaxies is completely stripped within a few Gyrs. In Figure 2 we show a UCD and a nucleated dwarf elliptical in comparison. Both are located in the very heart of the Fornax cluster.

2. UCDs were formed from the agglomeration of many young, massive star clusters that were created during merger events (e.g. Fellhauer and Kroupa 2002). Such super-star cluster complexes are observed in interacting galaxies like the Antennae. In this formation process no dark matter would be involved.

3. UCDs are the brightest globular clusters and were formed in the same GC formation event as their less massive counterparts (e.g. Mieske et al. 2004). The most massive GCs then supposedly formed from the most massive molecular clouds (MCs) of their host galaxy. The luminosity-size relation of the most massive clusters suggests that there is a break of the formation/collapse physics at a critical MC mass. Also in this case no dark matter in UCDs is expected.

4. UCDs are genuine compact dwarf galaxies, formed in small dark-matter halos at the low mass end of cosmological substructure. This scenario has the advantage that no external processes, like mergers or tidal disruption, are needed. A considerable dark-matter component is expected if this formation channel applies.

How can a massive *star cluster* be discerned from a low-mass compact *galaxy*? The answer may be hidden in the seen and unseen mass of UCDs. Dwarf galaxies are expected to be dark matter dominated, globular clusters are not. Thus, the best way to distinguish between these two possibilities is to measure the masses of UCDs. In order to do so we need to measure the motion of stars within UCDs with high-resolution spectroscopy. The faster their motion, the larger the UCD mass. The Ultraviolet and Visual Echelle Spectrograph (UVES) at the VLT is an ideal instrument to solve the UCD riddle.

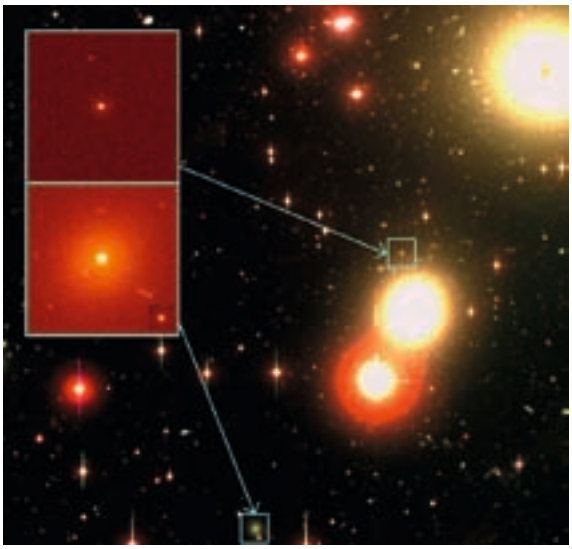

Figure 2: A composite image of the central region of the Fornax cluster based on data acquired at the 2.5-m DuPont telescope at the Las Campanas Observatory. Images in the filters *B*, *V*, *I* and were combined to make the colour composite. The insets show HST/STIS images of a UCD (upper) and a nucleated dwarf elliptical galaxy (lower).

UVES spectroscopy

High-resolution spectra were obtained for four Fornax UCDs, one nucleus of a dwarf elliptical and several reference stars (mostly red giant stars) in service mode at the VLT in 2000/2001. The integration times were between one and six hours, depending on the brightness of the UCD. For the reduction of the spectra, the UVES pipeline, provided by ESO, was used with some slight modifications. The spectral resolution of the final, reduced spectra was ~ 8 km s^{-1}. The signal-to-noise ranged between 10 and 20 at 5900 Å. In Figure 3 we show spectra of the four UCDs and four reference stars in the wavelength region of the Sodium (Na) doublet absorption lines. Such absorption lines are important features to measure the internal velocity dispersion of the UCDs. One can clearly see that UCD absorption lines are broadened with respect to the ones of the reference stars. This broadening is caused by the internal velocity dispersion of stars populating the UCDs.

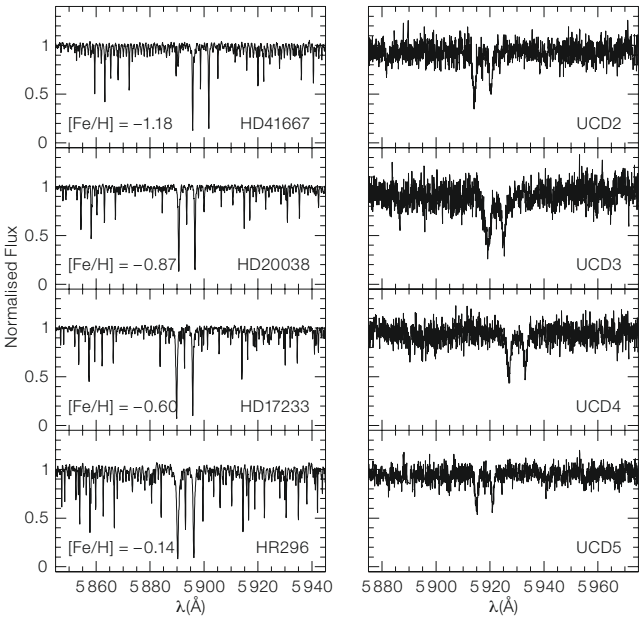

Figure 3: UVES spectra of four standard stars (left) and four UCDs (right) around the wavelength region of the Na doublet.

Internal velocity dispersions

The kinematic analysis of the spectra was performed using a direct-fitting method (van der Marel and Franx 1993). First, the spectra were placed on a logarithmic wavelength scale and normalised. Then, the reference star spectra were convolved with Gaussian velocity dispersion profiles in the range 2 to 60 km s^{-1}. All UCD spectra were fitted with all sets of smoothed 'template' spectra. In this process the template spectra are shifted in wavelength and scaled to match the redshifts and absorption strengths of the UCD spectra. The best-fitting Gaussian velocity dispersion profile is determined by χ^2 minimisation in pixel space. Figure 4 illustrates the fitting method for the brightest UCD in the Na doublet region. The reference spectrum (middle panel) is shifted, broadened and scaled to match the target spectrum (lower panel).

The velocity dispersions of the Fornax UCDs, derived from this method, range between 22 and 30 km s^{-1}, with errors of 1–3 km s^{-1}. These velocity dispersions are larger than those of 'normal' globular clusters (~ 5–15 km s^{-1}).

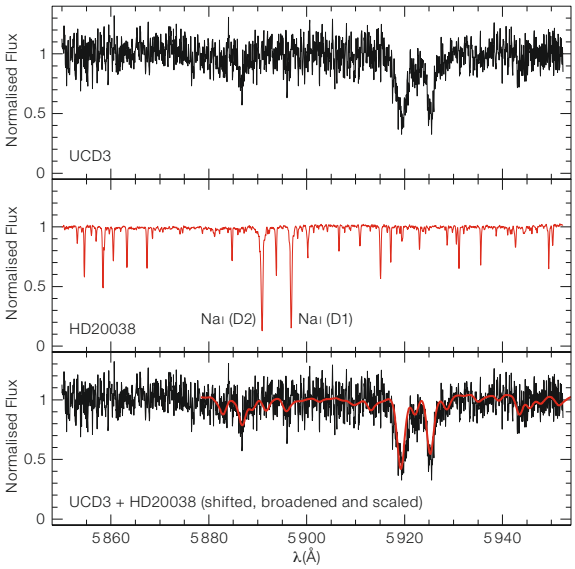

Figure 4: Illustration of velocity dispersion measurement for UCD3.

Mass modelling

As outlined above, the masses and mass-to-light ratios of the UCDs are important physical parameters for understanding their origin. In particular, the mass-to-light ratio (M/L) can be used as an indicator for the presence of dark matter and/or the violation of dynamical equilibrium. If UCDs were the counterparts of globular clusters – thus a single stellar population without significant amounts of dark matter – one would expect M/L values as predicted by standard single stellar population models (e.g. Maraston 2005). If UCDs are of cosmological origin – formed in small, compact dark-matter halos – they might be dominated by dark matter and show a high M/L value. Mass-to-light ratios that are larger than expected from single stellar populations can, however, also be caused by objects that are out of dynamical equilibrium, e.g. tidally disturbed stellar systems.

To derive the masses of the UCDs a new modelling program has been developed that allows to choose between different representations of the surface brightness profile of UCDs (i.e. Nuker, Sersic or King laws) and corrects the observed velocity dispersions for observational parameters (i.e. seeing, slit size). The light-profile parameters of the UCDs were obtained from Hubble Space Telescope imaging (Evstigneeva et al. 2007). In general, King models are good representations of globular cluster light profiles. UCDs, however, are better fitted by Nuker or generalised King laws, especially in the outer parts. Figure 5 illustrates the model output of our program. The three-dimensional density distribution, the cumulative mass distribution and the projected velocity dispersion profile that simultaneously fit the observed velocity dispersion and the light profile of UCD2 are shown.

Figure 5: Model output for UCD2. Grey dots represent 100 000 test particles. Blue dots are those 'stars' whose centres fall into the analysed slit area. The red circle (and red dashed line on the right) indicates the projected half-light radius of UCD2. The right panels show, from top to bottom, the three-dimensional density distribution, the cumulative mass distribution and the projected velocity dispersion profile for three different light-profile representations of UCD2. The vertical short dashed line indicates the radius of 1 ACS pixel and the dotted line half the slit width.

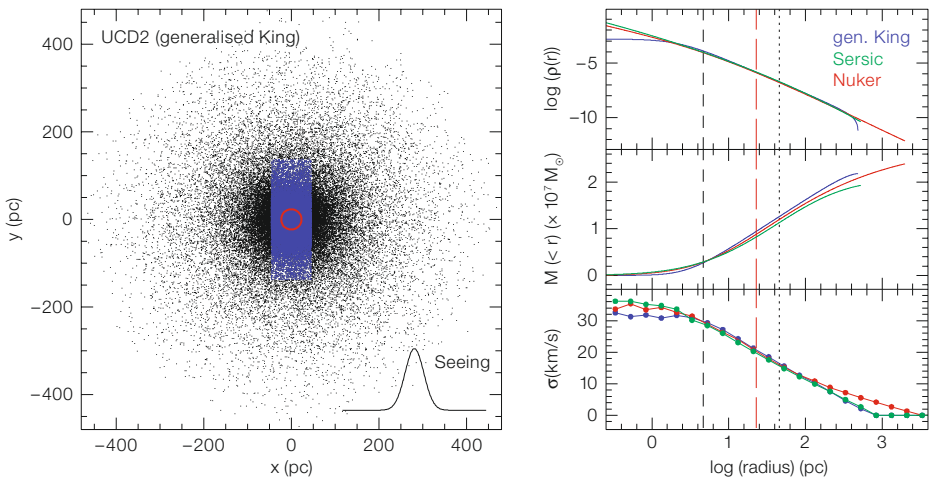

The masses of the UCDs derived in this way range between 1.8 and 9.5 × 10^7 $M_\odot$. For comparison, the mass of the most massive Galactic globular cluster, ω Centauri is ~ 0.5 × 10^7 $M_\odot$. The baryonic mass of Local Group dwarf spheroidals is comparable to that of UCDs.

Dynamical *versus* stellar masses

Knowing the age and the metal content of a stellar population, one can, in principle, predict its total mass. This is the task of stellar population models. A non-trivial ingredient of these models is the initial mass function (IMF) of the stars in the stellar population. The shape of the IMF, i.e. whether there are more or less low-mass stars as compared to high-mass stars, influences the total M/L ratio of a stellar population.

We have compared the derived dynamical masses of UCDs in Fornax to those expected from stellar population models. The dynamical M/L_V of the UCDs range between 3 and 5 $M_\odot/L_{\odot,V}$. In Figure 6 we show these M/L_V values as a function of metallicity [Z/H] and as a function of (V–I) colour (taken from Mieske at al. 2006). Results for the dwarf elliptical nucleus (FCC303) and a fifth UCD in Fornax (Drinkwater et al. 2003) are also shown in this figure. The difference between assuming a Kroupa or Salpeter IMF is that a Salpeter IMF implies that two of five Fornax UCDs would be dominated by intermediate-age populations of ~ 5 Gyr. Using a Kroupa IMF all UCDs are compatible with old, galactic globular cluster-like ages. Figure 6 suggests that the M/L_V values of the UCDs can, in principle, be explained by pure stellar populations. Dark matter is not mandatory for any of the objects. This conclusion, however, applies to the central region, where we have the data covered by our spectroscopic observations (within 1–3 half-mass radii). It cannot be ruled out that UCDs are dominated by dark matter at large radii where high signal-to-noise spectra cannot easily be obtained due to the very low surface brightness. Also, high-quality (high signal-to-noise) spectroscopic data are needed to better constrain the Fornax UCD metallicities and to determine their ages and abundances for a reliable comparison with stellar population models.

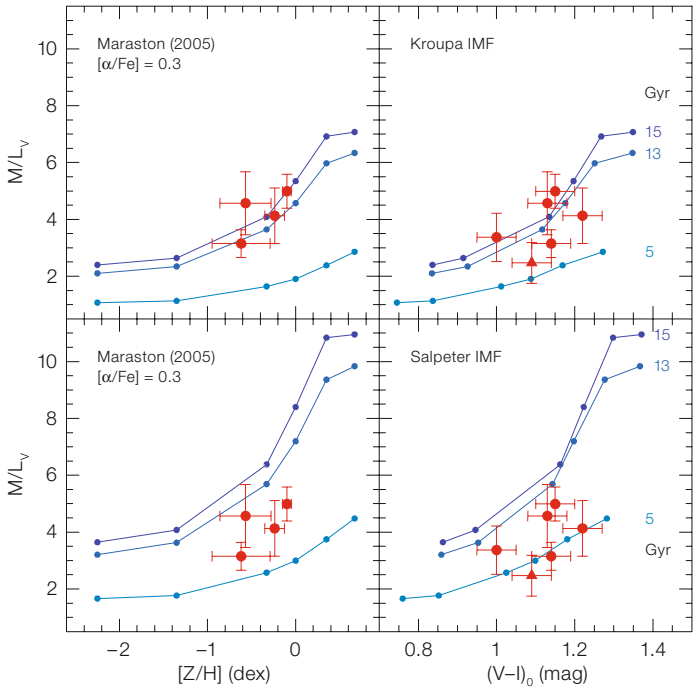

Figure 6: Dynamical M/L_V ratios of Fornax UCDs (red circles) and the nucleus of FCC303 (red triangle) are compared to expected M/L_V values from stellar population models of various ages (blue lines). On the left, M/L_V is plotted versus metallicity [Z/H], on the right versus the colour $(V-I)_0$. The adopted IMFs are indicated in the right panels.

We conclude that ultracompact dwarf galaxies are most probably the result of star cluster formation processes within galaxies – i.e. large globular clusters, assembled star cluster complexes, nuclear star clusters – rather than being genuine cosmological substructures themselves – i.e. compact galaxies formed in small, compact dark-matter halos. No dark-matter component is needed for UCDs within 1–3 half-mass radii.

Future prospects

While we have good ideas about the possible origin of UCDs, there are many questions left to answer concerning their nature. Some important ones include: Do UCDs have multiple stellar populations? What is the chemical abundance pattern of UCDs? What is their luminosity weighted age? Why do some UCDs have quite high M/L ratios? Is this due to tidal disturbances? Or do they contain dark matter? Do UCDs harbour black holes?

Some of these questions will be answered in the next years with the help of ongoing and future observing programmes (in particular with the VLT).

References

Bekki K. et al. 2003, MNRAS 344, 399
Drinkwater M. J. et al. 2003, Nature 423, 519
Evstigneeva E. A. et al. 2007, AJ 133, 1722
Fellhauer M. and Kroupa P. 2006, MNRAS 367, 1577
Hilker M. et al. 2007, A&A 463, 119
Hilker M. et al. 1999, A&AS 134, 75
Maraston C. 2005, MNRAS 362, 799
Mieske S., Hilker M. and Infante L. 2004, A&A 418, 445
Mieske S. et al. 2006, AJ 131, 2442
Phillipps S. et al. 2001, ApJ 560, 201
van der Marel R. P. and Franx M. 1993, ApJ 407, 525

VLT/FORS Surveys of Wolf-Rayet Stars beyond the Local Group: Type Ib/c Supernova Progenitors?

Paul A. Crowther, Lucy J. Hadfield
(University of Sheffield, United Kingdom)

Wolf-Rayet (WR) stars are the chemically evolved descendents of O stars, such that they trace massive star formation. Here we present results of recent VLT/FORS surveys of WR stars in nearby spiral and irregular galaxies and consider individual WR stars as progenitors of Type Ib/c core-collapse supernovae. Young massive clusters hosting large WR populations may be used as templates for high-redshift Lyman break galaxies.

Massive stellar evolution

Massive stars form in star clusters within star-forming galaxies, pollute the interstellar medium, injecting energy and momentum via powerful stellar winds and core-collapse supernovae (SNe). The detection of massive stars within Lyman-break galaxies at high redshift, either directly via their UV continua or indirectly via ionised HII regions, provides some of the most stringent constraints upon their physical properties.

The Initial Mass Function favours the formation of low- and intermediate-mass stars with respect to high-mass stars, for which the boundary is conventionally set at 8 $M_{\odot}$ – the division between stars ultimately forming a CO white dwarf or an iron core, the latter subsequently undergoing a core-collapse SN. Spectroscopically, stars with initial masses of 8–20 $M_{\odot}$ are B-type dwarfs on the main sequence, or O-type dwarfs at higher initial mass. Such high-mass stars possess convective cores, and radiative envelopes, a situation reversed in the Sun and other low-mass stars. Although there is energy transport from the convective and radiative regions, only the convective core participates in nuclear reactions, unless hydrogen-rich material is mixed downwards from the outer zones.

Once the core hydrogen is exhausted, the star leaves the main sequence and becomes a blue supergiant, and ultimately a red supergiant (RSG) for stars with initial mass up to perhaps 20–30 $M_{\odot}$. Observationally, there is an absence of luminous RSGs, known as the Humphreys-Davidson limit, such that initially more massive stars circumvent the RSG phase, pass through a Luminous Blue Variable stage, before ending their life as Wolf-Rayet (WR) stars, exhibiting either the products of core-H burning (WN subtypes) or subsequent core-He burning (WC, WO subtypes).

Consequently, the prime candidates for core-collapse SN are RSG and WR stars for H-rich (Type II) and H-poor (Type Ib/c) cases, respectively. Indeed, within the past few years a direct connection has been established between certain Type Ic SNe and gamma-ray bursts (GRBs), supporting the collapsar model in which the GRB results from the death throes of a rapidly rotating WR star.

Relative to lower-mass stars, the evolution of high-mass stars is complicated by: (a) the metallicity dependence of their radiatively line-driven stellar winds, producing weaker winds at low metallicity; and (b) their initial rotational velocities, providing rotationally-induced mixing within their interiors. It is only within the past decade that allowance for both effects has been considered within evolutionary models, most recently implemented into spectral synthesis models (Vazquez et al. 2007).

Surveys of Wolf-Rayet stars in star-forming spiral galaxies

WR stars exhibit a unique, broad emission line spectral appearance which provides the basis for their detection in external galaxies. Notably, narrowband interference filter techniques have been independently developed by Moffat and Massey that permit their detection from their strong emission lines at HeII λ 4686 (WN stars) and CIII λ 4650 (WC stars) with respect to their nearby continuum. Such techniques have been applied to regions of the Milky Way disc, the Magellanic Clouds and other Local Group galaxies.

It is well established that the absolute number of WR stars and their subtype distribution are metallicity dependent. N(WR)/N(O) ~ 0.15 in the relatively metal-rich Solar Neighbourhood, yet N(WR)/N(O) ~ 0.01 in the metal-deficient SMC on the basis of only 12 WR stars *versus* ~ 1000 O stars (Crowther 2007). This observational dependence follows since the hydrogen-rich envelopes of O stars are more easily removed at high metallicity. O-type stars possess strong winds that are driven by metallic lines (primarily CNO and Fe-peak elements), for which the empirical dependence upon metallicity Z is $\dot{M} \propto Z^{0.8}$ for stars between SMC and Milky Way metallicities (Mokiem et al. 2007).

Attempts have been made with 4-m telescopes to extend the interference filter technique to star-forming galaxies beyond the Local Group, although this proved to be challenging (e.g. Testor and Schild 1993). The advent of efficient multi-object spectrographs such as FORS1/2 at the Very Large Telescope has permitted surveys of WR populations in galaxies at distances beyond 2 Mpc (Table 1). An example of our FORS1 imaging approach is presented in Figure 1 for the barred spiral galaxy NGC 1313 (see also the cover page of the current Messenger). The boxed region 60 × 60 arcsec in size within NGC 1313 hosts in excess of twenty WR stars, most of which are within a large giant HII region. Overall, the success rate of identifying WR stars from

Galaxy	D (Mpc)	log (O/H)+12	N (O7V)	N(WN)	N(WC)	Reference
NGC 300	1.9	8.6:	800	≥ 16	~ 15:	Schild et al. 2003; Crowther et al. 2007
NGC 1313	4.1	8.2	6500	≥ 51:	~ 33:	Hadfield and Crowther 2007
M83	4.5	9.0?	40000	≥ 470	≥ 560	Hadfield et al. 2005
NGC 3125	11.5	8.4	3600	200	40	Hadfield and Crowther 2006

Table 1: Summary of southern star-forming galaxies whose WR populations have been surveyed with FORS1/2 to date. The O star contents are based upon a SFR for an assumed O7V Lyman continuum flux of 10^{49} per second, omitting regions excluded from our WR surveys, i.e. the outer disc of NGC 300 and the nuclear starburst of M83.

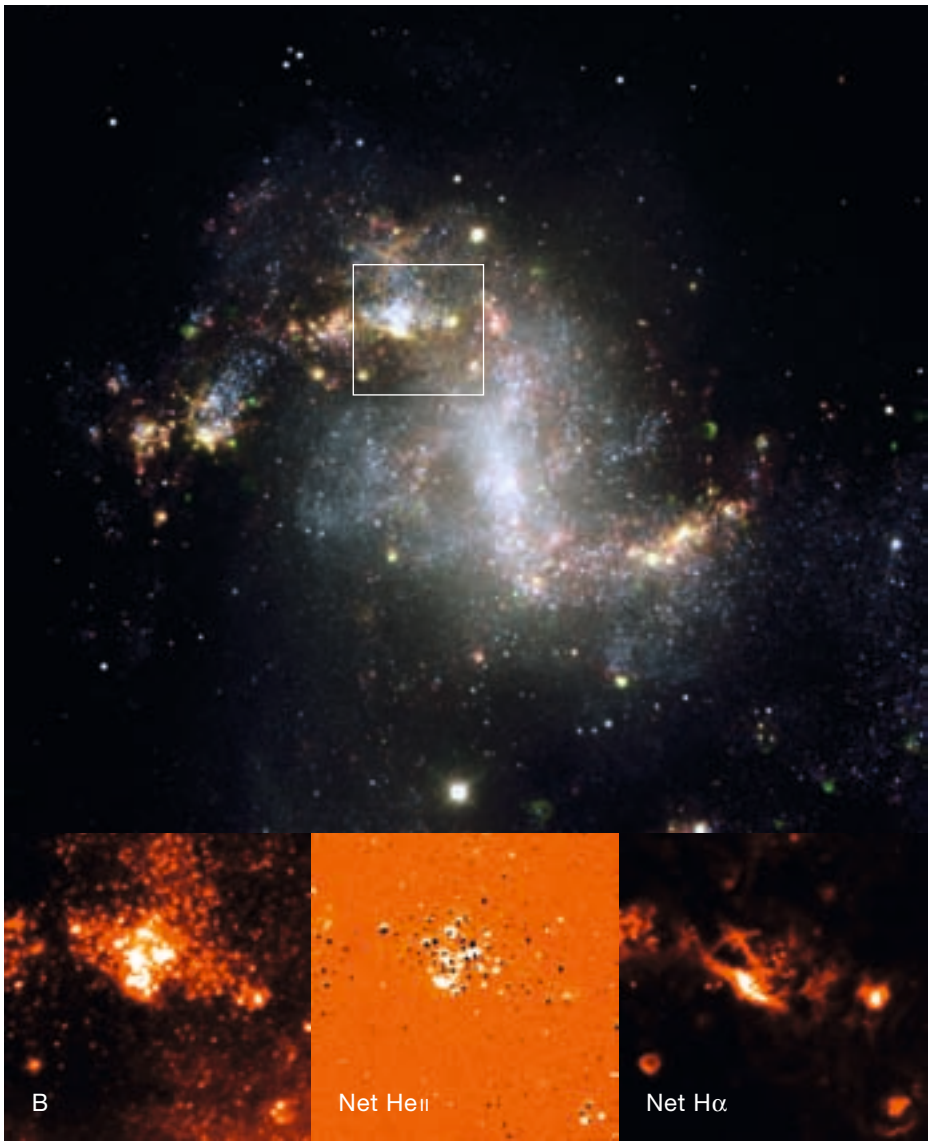

Figure 1: The upper panel shows a composite FORS1 image of NGC 1313 (ESO Press Photo 43a/06) showing a 60 × 60 arcsec box, for which the lower panels show FORS1 images of broadband B, continuum subtracted HeII 4686 (excesses are shown in white), continuum subtracted Hα, from left to right.

our FORS surveys is high. For the case of NGC 1313 we have identified 94 candidate WR stars, for which a subset of 83 % have been spectroscopically observed. Within this subset, 90 % of the sources have been spectroscopically confirmed as WR stars, as indicated in Figure 2 (Hadfield and Crowther 2007).

Regarding WN and WC subtype distributions, similar numbers are observed in the Solar Neighbourhood. In contrast, WN stars exceed WC stars by a factor of ~ 5 and ~ 10 for the LMC and SMC, respectively (Crowther 2007). At low metallicity the reduced WR population and the relative dominance of WN subtypes most likely results from the metallicity dependence of winds from their evolutionary precursors. Consequently, only the most massive single stars reach the WR phase in metal-poor environments.

Not all WR subtypes are observed in all environments. Early-type WN and WC subtypes dominate in metal-poor galaxies, such as the SMC, while late WC stars are more common at super-Solar metallicities, such as M83 (Hadfield et al. 2005). This observational trend led to suggestions that early-type WC stars are richer in carbon than late-type WC stars. However, quantitative analysis of WC subtypes, allowing for radiative transfer effects, do not support a subtype dependence of elemental abundances in WC stars.

In contrast, Crowther et al. (2002) proposed that late spectral types follow in metal-rich environments, and early types at low metallicity due to metallicity dependent WR winds. Indeed, WO stars (extreme WC early types) are preferentially seen at low metallicity. Consequently, the representative WC subtype of a galaxy permits an estimate of its metallicity. Metal-poor WR stars possess harder Lyman continuum ionising flux distributions than high-metallicity counterparts, in agreement with the association of nebular HeII λ 4686 with low-metallicity WR stars (e.g. Hadfield and Crowther 2007).

Evolutionary models for the Wolf-Rayet stage have typically assumed metallicity independent mass-loss rates, which both observational and theoretical evidence now challenges. The metallicity dependence of WN winds appears to be similar to O stars, with a somewhat weaker dependence for WC stars due to their high carbon and oxygen abundances; the latter is of relevance to the observed ratio of WC to WN stars predicted by evolutionary models (Eldridge and Vink 2006).

One related topic involves the search for Wolf-Rayet stars in close binary systems with neutron-star or black-hole companions. Such systems represent a natural, though rare, end state for close binary evolution, for which Cyg X-3 in the Milky Way has been the sole example up until recently. The combination of high spatial resolution X-ray surveys plus our WR surveys of nearby galaxies has increased this number to three, IC 10 X-1 in the northern sky, and NGC 300 X-1 in the south, both of which are probable WR plus black-hole systems (e.g. Crowther et al. 2007).

Type Ib/c supernova and gamma-ray burst progenitors?

At solar metallicity, stars initially more massive than ~ 25 $M_{\odot}$ apparently end their lives as either a nitrogen-rich (WN) or carbon-rich (WC) WR star. WN and WC stars are believed to be the immediate progenitors for a subset of Type Ib (H-poor) and Type Ic (H and He-poor) supernovae, respectively. Alternatively, lower-mass binaries may produce Type Ib (Type Ic) SN in which H (both H and He) has been stripped away due to Roche lobe overflow and/or common envelope evolution. Some Type Ib/c SN do occur in elliptical/S0 host galaxies – explicitly 4 from 50 Type Ib/c SNe within the last decade within 50 Mpc – in favour of such lower-mass progenitors. Nevertheless, the vast majority are preferentially in actively star-forming galaxies. So are most Type Ib/c SN from massive WR stars or lower-mass interacting binaries?

To date, broadband surveys of local ($\leq$ 10 Mpc) star-forming galaxies have been undertaken with Hubble Space Telescope and ground-based 8-m telescopes by groups in the UK and US. These have been successful in identifying RSG progenitors of the most common core-collapse SN (Type II-P, Smartt et al. 2004). Unfortunately, WR stars are visually much fainter than RSG and may not be distinguished from blue supergiants on the basis of existing broadband surveys alone. Observationally, SN 2002ap (Type Ic) in M74 so far provides the most stringent constraints upon a potential WR progenitor, revealing an upper limit of $M_B = -4.2$ mag (Crockett et al. 2007). The precursor of SN 2002ap was either a relatively faint WC star, or more likely a lower-mass binary system.

One application of our WR surveys with the VLT would be to establish whether a WR star was the progenitor of a future Type Ib/c SN, if it occurred in one of our surveyed galaxies. For the case of M83, we have identified in excess of 1000 WR stars within the galactic disc. The star-formation rate (SFR) in M83 may be estimated from its global Hα flux of 7 × 10^{-11} erg s^{-1} cm^{-2} (Kennicutt, priv. comm.), corrected for average extinction (E_{B-V} ~ 0.5 mag), i.e. a SFR of 4.3 $M_{\odot}$ yr^{-1} (Kennicutt 1998) for an adopted distance of 4.5 Mpc. If we are able to study ~ 10 nearby galaxies with such a high SFR, we would sample in excess of 10^4 WR stars. Statistically one of those stars would be expected to collapse to a Type Ib/c SN within the next decade, given that WR lifetimes are ~ 10^5 yr. Indeed, we have already come close to success. Our FORS1 narrowband imaging of the merging 'Antennae' galaxies (NGC 4038/9) for WR stars was obtained in June 2005, sadly six months *after* the Type Ic SN 2004gt.

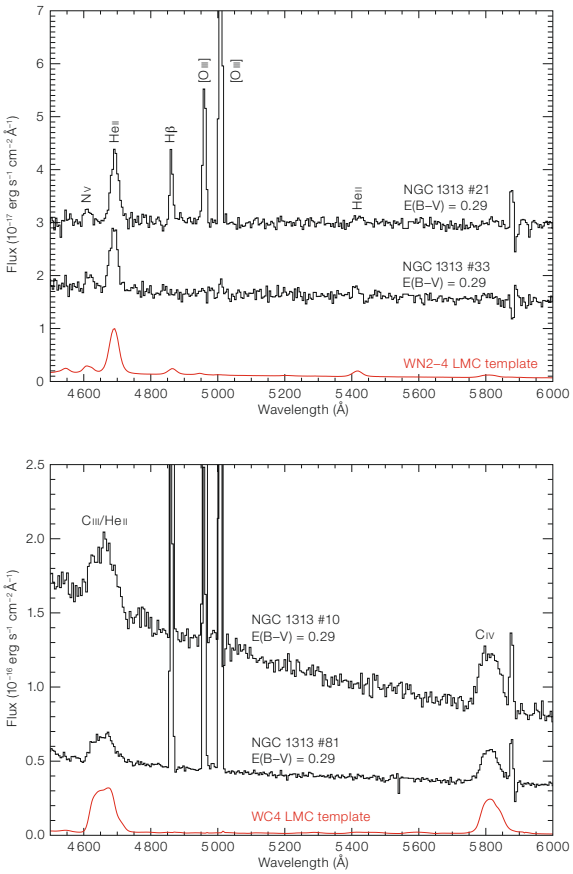

Figure 2: Representative early-type WN (upper panel) and WC (lower panel) stars identified in our NGC 1313 survey (Hadfield and Crowther 2007), together with average LMC template spectra (shown in red) from Crowther and Hadfield (2006).

Of course, astrometry is rather challenging from ground-based imaging. High spatial resolution imaging helps greatly, as indicated in Figure 3 where we compare the location of a (rare) WO star in NGC 1313, identified from FORS1 narrowband imaging and spectroscopic follow-up, to HST/ACS broadband imaging.

This general topic has received renewed interest since a number of nearby, bright Type Ic SNe have been observationally associated with several nearby GRBs (e.g. SN 2003dh = GRB 030329 Hjorth et al. 2003). These favour the 'collapsar' scenario, involving the core collapse of a rotating Wolf-Rayet star to a black hole via an accretion disc, in which the rotational axis provides a preferred direction for the jet (MacFadyen and Woosley 1999). Hammer et al. (2006) identify WR stars within a giant HII region of ESO 184–G82 several hundred pc from the location of SN 1998bw = GRB 980425, and propose that the GRB progenitor was ejected from the WR cluster.

Rotation is critically important since the collapsar model involves highly collimated jets produced along the polar axes, due to a dense, equatorial accretion disc feeding the central black hole. At low metallicity, the spin-down induced by mechanical mass-loss during the Wolf-Rayet phase may be avoided due to the relatively weak winds, resulting in sufficient angular momentum in the core upon core collapse. Of course, only a tiny fraction of SNe produce a GRB, with an apparent bias towards metal-poor environments (Modjaz et al. submitted) with respect to

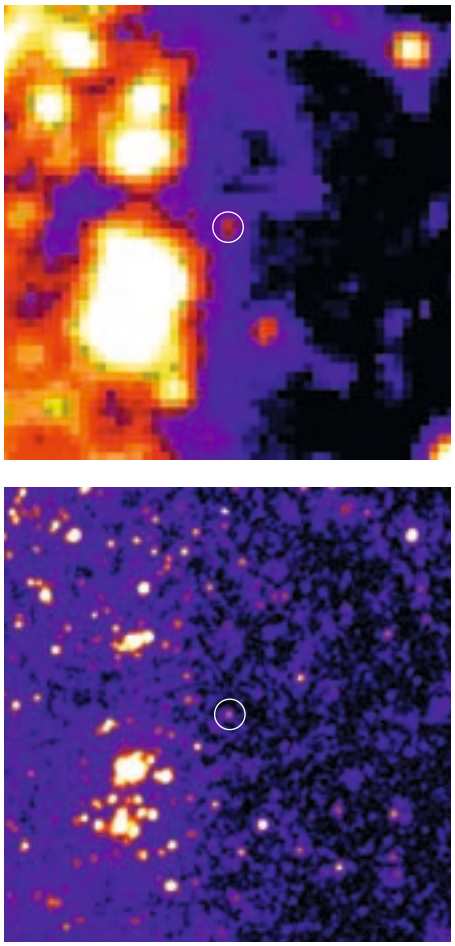

Figure 3: Comparison of a 10 × 10 arcsec (200 × 200 pc) region of NGC 1313 centred upon a WO star imaged by FORS1 (He II λ 4686 filter, top) and HST/ACS (F435W/WFC, bottom). The WO has a F435W magnitude of 23.4 mag, suggesting M_{F435W} ~ −5.2 mag for a distance modulus of 28.0 mag (4.1 Mpc) and A_{F435W} ~ 0.6 mag.

non-GRB Type Ic SN. As such, GRBs would trace the low-metallicity star-formation history of the Universe. The low metallicity bias favours the single star scenario, with respect to alternative close binary models.

WR clusters as templates for Lyman break galaxies

Individual WR stars may, in general, be resolved in Local Group galaxies from ground-based observations, whilst the likelihood of contamination by nearby sources increases at larger distances. For example, a typical slit width of 1″ at the 2 Mpc distance of NGC 300 corresponds to a spatial scale of ~ 10 pc. Relatively isolated WR stars have been identified, albeit in the minority (recall Figure 3). This is even more problematic for more distant galaxies such as M83 where the great majority of WR stars are observed in clusters or associations (Hadfield et al. 2005).

So-called 'WR galaxies' are typically starburst regions exhibiting spectral features from tens, hundreds, or even thousands of WR stars. Indeed, such knots of star formation, hosting young massive clusters (~ 10^6 $M_\odot$) often reveal significant WR populations, seen at UV or visual wavelengths. Their appearance is reminiscent of the composite rest-frame UV spectrum of z ~ 3 star-forming galaxies (~ $10^{10–11}$ $M_\odot$) which also show broad He II λ 1640 emission (Shapley et al. 2003).

A recent ultraviolet HST/STIS survey of local starburst galaxies also revealed strong He II λ 1640 emission in a few cases, most notably a young massive cluster within NGC 3125, alias Tol 3 (Chandar et al. 2004). This LMC-metallicity galaxy is dominated by a central starburst region which consists of two main emission knots, NGC 3125-A and -B, shown in Figure 4. From UV spectroscopy, Chandar et al. (2004) estimated 5 000 WR stars for a cluster within knot A, with a remarkable N(WR)/N(O) ≥ 1. In contrast, optical studies of NGC 3125-A infer a WR population that is an order of magnitude lower, in better agreement with the relative massive star content of other local starburst galaxies. If NGC

Figure 4: Composite *B*, *V*, *Hα* HST/ACS image of NGC 3125 (20 × 20 arcsec = 1 × 1 kpc) in which young massive clusters within knot A (upper right) and knot B (lower left) host significant WR populations (Hadfield and Crowther 2006). Insets are composite *U*, *V* and *I* ACS images for the central 1 × 1 arcsec for each knot, revealing clusters A1-2 and B1-2. Our study, based upon VLT/FORS1 imaging and spectroscopy resolves previously inconsistent massive stellar populations for cluster A1 from UV (HST/STIS) versus optical diagnostics.

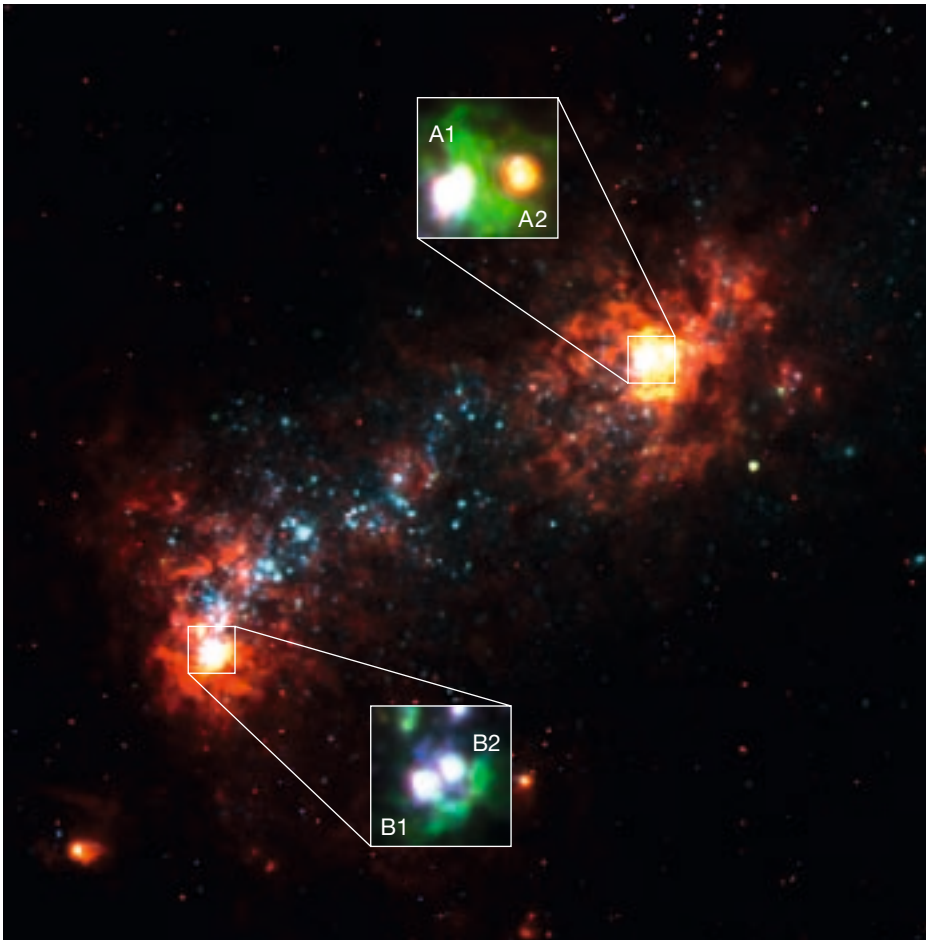

3125-A is an analogue for Lyman-break galaxies, one must be able to reconcile optical and UV diagnostics for this starburst galaxy.

Hadfield and Crowther (2006) re-investigated the massive stellar content of NGC 3125 from FORS1 imaging and spectroscopy, supplemented by archival HST imaging and spectroscopy. FORS1 narrowband imaging confirms that the NGC 3125-A and -B knots represent the primary sites of WR stars. HST imaging resolves each knot into two young massive clusters, as shown in Figure 4. Our FORS1 imaging reveals that both clusters within knot A host WR stars (A1 and A2), for which the visually fainter cluster A2 is heavily reddened. From ground-based imaging is not clear whether B1 or B2 (or both) host WR stars, since their separation is ~ 0.2 arcsec (10 pc).

LMC template WN and WC spectra from Crowther and Hadfield (2006) were matched to the FORS1 visual WR features in A1 and B1+B2, permitting their relative contributions to be determined. From Figure 5, we derive N(WN) ~ 105 in cluster A1, a factor of ~ 3 lower than previous optical studies, owing to a lower nebular-derived interstellar reddening. Using Starburst99 theoretical energy distributions to estimate O star populations for each cluster, we find N(WR)/N(O) = 0.1–0.2 for clusters A1-A2 (each 2×10^5 $M_\odot$), in broad agreement with evolutionary models.

Archival HST/STIS UV spectroscopy confirms the low interstellar extinction towards A1, assuming an SMC-like reddening law. We obtain N(WN) = 110 from the slit loss corrected HeII λ 1640 line flux, in excellent agreement with optical results. Our HST/STIS result is however a factor of 35(!) times lower than that inferred from the same data set by Chandar et al. (2004). The discrepancy is primarily due to an anomalously high far-UV-derived extinction from their use of the generic starburst law. Consequently, far-UV-based results for other nearby starburst knots should be treated with caution.

In conclusion, our ongoing WR surveys of nearby galaxies permit studies of young massive stellar populations across a range of ambient metallicities, with influence on evolutionary synthesis models for massive stars, WR stars, enable Type Ib/c supernova and GRB progenitors, and local young massive clusters as templates for high-redshift star-forming galaxies. In the near future we aim to extend our surveys to other galaxies with high SFRs in the southern hemisphere with the VLT and in the northern hemisphere with other facilities. Indeed, WFPC2 (until SM4) and WF3 (after SM4) aboard HST possess a narrow HeII filter. These may be used with broadband continuum filters to identifty WR candiates at high spatial resolution.

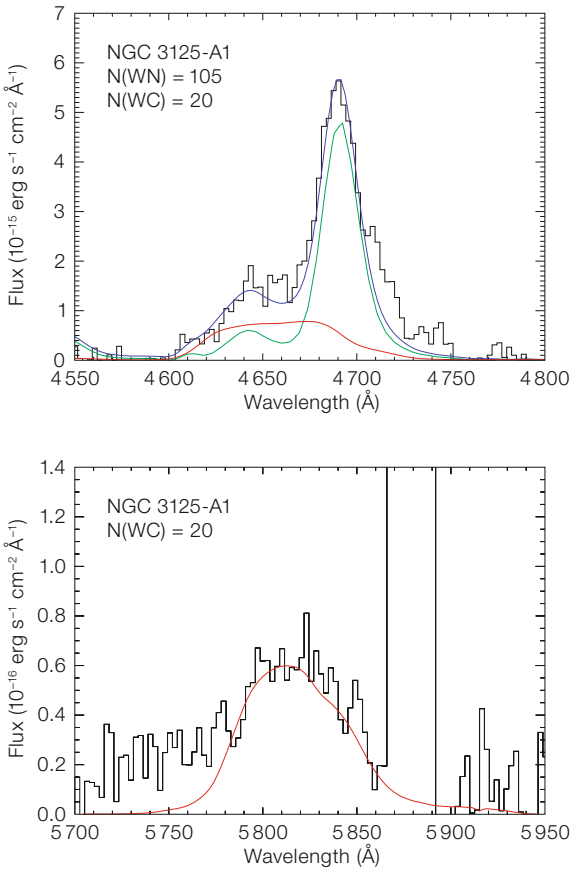

Figure 5: De-reddened, continuum subtracted VLT/FORS1 spectroscopy of NGC 3125-A1 (black, Hadfield and Crowther 2006), together with scaled LMC-metallicity templates for WN (green) and WC (red) stars, plus their sum (blue).

Acknowledgements

Thanks to Hans Schild for the introduction to WR surveys beyond the Local Group, ESO for including HeII filters within the standard filter set of FORS, and the support of the OPC sub-panels since Period 65.

References

Chandar R. et al. 2004, ApJ 604, 153
Crockett R. M. et al. 2007, MNRAS, in press, arXiv:0706.0500
Crowther P. A. 2007, ARA&A 45, 177
Crowther P. A. and Hadfield L. J. 2006, A&A 449, 711
Crowther P. A. et al. 2002, A&A 392, 653
Crowther P. A. et al. 2007, A&A 469, L31
Eldridge J. and Vink J. 2006, A&A 452, 295
Hadfield L. J. and Crowther P. A. 2006, MNRAS 368, 1822
Hadfield L. J. and Crowther P. A. 2007, MNRAS, in press, arXiv:0708.2039
Hadfield L. J. et al. 2005, A&A 439, 265
Hammer F. et al. 2006, A&A 454, 103
Hjorth J. et al. 2003, Nature 423, 847
Kennicutt R. C. 1998, ARA&A 36, 189
MacFadyen A. and Woosley S. 1999, ApJ 524, 262
Mokiem M. R. et al. 2007, A&A, in press, arXiv:0708.2042
Schild H. et al. 2003, A&A 397, 859
Shapley A. et al. 2003, ApJ 347, 127
Smartt S. et al. 2004, Sci 303, 499
Testor G. and Schild H. 1993, The Messenger 72, 31
Vazquez G. A. et al. 2007, ApJ 663, 995

Surface Ice Spectroscopy of Pluto, Charon and Triton

Silvia Protopapa[1]
Tom Herbst[2]
Hermann Böhnhardt[1]

[1] Max-Planck Institute for Solar System Research, Lindau, Germany
[2] Max-Planck Institute for Astronomy, Heidelberg, Germany

We present new reflectance spectra of Pluto and Triton taken with the ESO adaptive optics instrument NACO at the VLT and covering the wavelength range 1–5 μm. Apart from known and expected absorption bands from methane ice, our data reveal new absorption bands centred around 4.0 μm and 4.6 μm never detected before. The latter absorption could be related to the presence of CO ice at the body surfaces. Charon's spectrum is also measured in the wavelength range 1–4 μm, for the first time simultaneously with, but isolated from, that of Pluto. The non-detection of Pluto's moonlets (unknown at the time of observation) in acquisition images of Pluto-Charon provides a lower limit of 18.8 mag for the *K*-band brightness of Hydra and Nix.

Dwarf planets and New Horizons

Things are changing in the outer Solar System: Pluto got 'degraded' by the IAU from a 'real' planet to a dwarf one. Shortly before this terrestrial decision, NASA launched the New Horizons spacecraft to approach Pluto and Charon in 2015 – and possibly one or two, yet undetected, Kuiper Belt objects thereafter. Also, recently, two new small moons, Nix and Hydra, were discovered around Pluto. Despite all these changes, Pluto and Charon, remain of high scientific interest, in particular since they can be considered – together with Neptune's moon Triton – as the best prototypes for the ice worlds in the outer Solar System and the Kuiper Belt. Best, because these three objects are bright and thus accessible for Earth-based observations not easily possible for other bodies of that kind. Here, we present new IR observations of Pluto, Charon and Triton performed with the VLT in order to characterise the ice content of the surfaces and to search for similarities and differences.

Pluto, Charon and Triton with NACO at the VLT

Scientific aim

The observations of the Pluto-Charon binary and of Triton were obtained with the adaptive optics instrument NACO at the ESO VLT during 3–7 August 2005. For Pluto-Charon the aim was to resolve the binary system and to measure spectra of the two objects, for the first time individually. So far, such type of spectra could only be obtained from disentangling unresolved and occultation (Charon occulted by Pluto) measurements of the system. Moreover, and even more important, we intended to extend the wavelength coverage of the surface spectroscopy beyond *K*-band, i.e. we were aiming for Pluto spectra up to 5 μm and for Charon at least up to 4 μm, with the goal to detect further surface ice absorption bands predicted from models of the available *JHK* spectra and to search for signatures of yet unknown ices. Triton, visible from the VLT at the same time, was a welcome object for comparison, since its *JHK* spectrum is similar to that of Pluto (but different from Charon), and at least as well known as the former. Like Pluto, the 3–5 μm region of Triton is still unexplored for this object, considered to be a Kuiper Belt object captured by Neptune.

Telescope and instrument set-up

NACO at the VLT Unit Telescope 4 (Yepun) was our first choice for this programme since it combines the high spatial resolution of adaptive optics, needed to resolve Pluto-Charon (variable along the orbit from 0.5–0.9″), and at the same time benefits from considerable signal-to-noise improvements for the spectroscopy. Moreover, NACO allowed to cover the full wavelength range from 1–5 μm at once with the intended spectral resolution using the prism L27_P1. Nevertheless, the NACO exposure time calculator indicated that, even with the great advantages of adaptive optics and low-dispersion prism, it would be difficult to measure the signal of Pluto and Triton in *M*-band and of Charon in *L*-band in three nights.

Observing procedure

The Pluto-Charon binary and Triton were used in the visible as the reference sources for the adaptive optics corrections. For Pluto-Charon the NACO slit (width 172 mas) was set along the orbital position angle of the binary, to acquire them both simultaneously. For Triton the slit was placed at the parallactic angle. The acquisition of the targets was performed in *K*-band and a suitable offset correction, depending on the zenith distance, was applied to achieve the optimum slit position of the objects in *L*- and *M*-band (though sacrificing slightly the *JHK* signal – at least for higher airmasses – by slit losses due to wavelength-dependent atmospheric refraction). The usual A-B-B-A nodding (with some jitter) was applied for the observations. In order to remove at once the telluric and solar features from Pluto/Charon and Triton's spectra, observations of the nearby solar analogue star HD 162341, recorded approximately once per 1.5 hour, were performed. In this way every Pluto-Charon and Triton observation had an associated 'before' and 'after' set of calibration star observations, made with similar sky conditions and identical instrument and AO settings.

Data reduction

Besides the usual data reduction for IR spectroscopy, special attention was paid to the wavelength calibration and the spectrum curvature correction of the NACO data. The former applies because no arc lamp spectra for *L*- and *M*-band are available in NACO; hence, atmospheric emission and absorption features were used as wavelength reference instead. The latter results from differential atmospheric refraction over the large wavelength range and was corrected by pixel shifts of the spectra applying the atmospheric refraction formula. Thereafter, we used optimum extraction to improve signal-to-noise ratio over aperture extraction. In order to recover from the unavoidable slit losses in the short wavelength region, we combined the extracted

L- and *M*-band spectra, combined over all nights, with selected object spectra in the *JHK* wavelength region and taken at low airmasses. The extracted spectra were normalised to published values for the albedo at fixed wavelengths and thereafter median averaged. This way we were able to reconstruct global spectra of the three targets – flux permitting – over the full wavelength range from 1–5 μm.

Pluto and Triton spectra from 1 to 5 μm

In Figures 1 and 2 we present the reflectance spectra of Pluto and Triton, obtained with NACO in the 1–5 μm wavelength range at a S/N in *J*-*K* and *L*-band equal to 50 and 11, respectively. For Pluto, it is the first time that the *L*-band is measured without contamination by light from Charon, and for both objects *M*-band spectra were never measured before.

Known compounds

The published spectra of the two objects have established that there is solid CH_4 on Pluto and Triton's surface (Douté et al. 1999; Quirico et al. 1999; Grundy et al. 2002), easily noticed from various absorption features in the *JHKL* bands. This is confirmed – in particular also for *L*-band – by our new NACO results. Indeed, in the range of wavelength 1.0–2.5 μm, the most prominent features evident in Pluto and Triton's spectra are strong CH_4 absorption bands near 1.16, 1.38, 1.66, 1.79, 2.20, 2.31 and 2.37 μm (Figures 1 and 2). Because of the low spectral resolution of the NACO prism, it is not possible to detect in both object spectra the absorption bands of N_2 at 2.148 μm and CO at 2.35 μm already found by Owen et al. (1993) and Cruikshank et al. (1993) for Pluto and Triton, respectively. The low resolution in *JHK* bands also does not allow us to detect CO_2 in Triton's spectrum.

In the range of wavelengths 2.8–4.1 μm, our spectra of Pluto and Triton show strong absorptions near 3.3, 3.5 and 3.8 μm, corresponding to methane's ν_3, $\nu_2 + \nu_4$ and 2 ν_4 vibrational transitions (Grundy et al. 2002; Olkin et al. 2007). It is important to note that the slope of

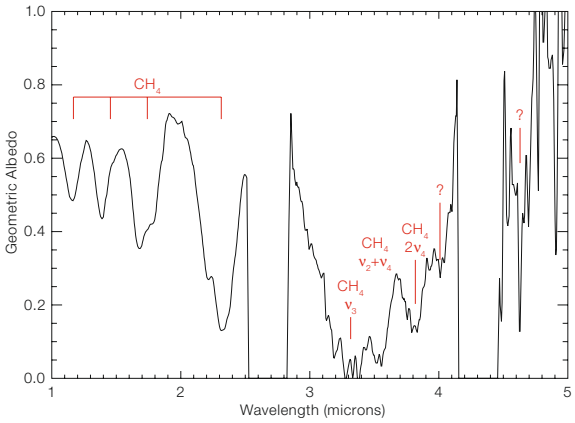

Figure 1: Pluto's spectrum in the range of wavelengths 1–5 μm. The species responsible for the absorption bands detected in our spectrum are marked in the figure. No object flux is measured in the atmospheric absorption bands at 2.5–2.8 and 4.1–4.4 μm.

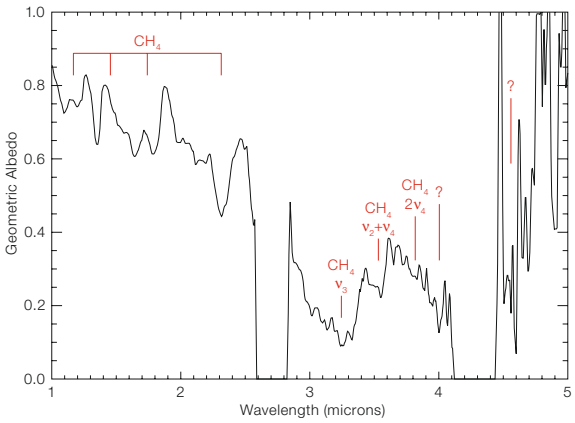

Figure 2: Triton's spectrum in the range of wavelengths 1–5 μm. The species responsible for the absorption bands detected in our spectrum are marked in the figure. No object flux is measured in the atmospheric absorption bands at 2.6–2.8 and 4.1–4.4 μm.

Pluto's spectrum from 2.8 to 3.1 μm, considered to be a diagnostic for the ratio of areas with pure CH_4 ice and CH_4 ice diluted in N_2 (Olkin et al. 2007), is different from the one of Triton. Since the spectrum of pure methane has a steeper slope in this region, this finding suggests that the percentage of diluted methane is higher in Triton than in Pluto. Another difference between Pluto and Triton's spectra is the albedo around the ν_3 band of CH_4 from 3.1 to 3.6 μm. As observed by Olkin et al. (2007), this constrains the fraction of pure N_2 on the surface. Hence, concluding from our NACO spectra, the presence of pure N_2 is greater in Triton than in Pluto.

Unknown features

By modelling Pluto's surface spectrum by geographical mixtures of pure methane, methane diluted in nitrogen and pure nitrogen (Douté et al. 1999), or pure methane, methane diluted in nitrogen and tholin (Olkin et al. 2007), it is not possible to reproduce the absorption band centred around 4.0 μm in our NACO data and indicated in Figure 1 by a question mark. This absorption band is also present in Triton's spectrum (Figure 2). Another question mark can be found in the figures at an absorption band centred around 4.6 μm, visible in both Pluto and Triton's spectra. This signature was found unexpectedly. A first interpretation assigns it to CO ice. In fact, CO ice has a strong absorption band at 4.67 μm (Palumbo and Strazzulla 1993).

Charon's spectrum from 1 to 4 μm

Our NACO spectrum of Charon in the wavelength range between 1 and 4 μm is shown in Figure 3. Charon's spectrum has previously been studied in some detail in the *JHK* wavelength region (Buie and Grundy 2000), but was never measured above 2.5 μm.

As expected, our Charon spectrum is dominated by the 1.5 and 2.0 μm absorption bands of water ice. The spectrum shows the 1.65 μm spectral feature characteristic of crystalline water ice, for the first time identified by Brown and Calvin (2000). Because of the low prism resolution, it is not possible to detect the absorption band at 2.21 μm related to the presence of ammonia hydrate NH_3H_2O, that should exist uniformly distributed on Charon's surface.

A narrow absorption band is found around 3.7 μm, indicated by a question mark in Figure 3. It cannot be reproduced by models of Charon's spectrum with pure H_2O ice darkened by a spectrally neutral continuum absorber (Olkin et al. 2007). Hence, it remains unidentified for the time being.

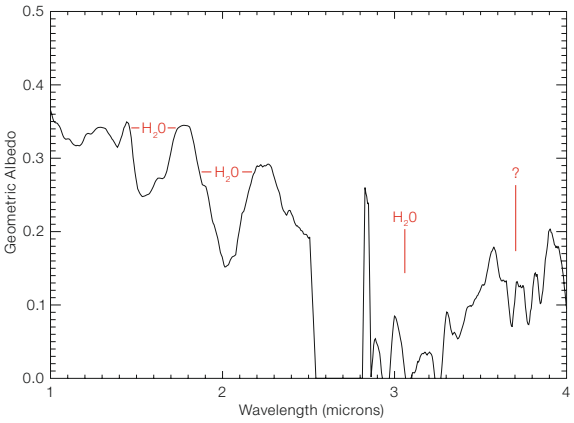

Figure 3: Charon's spectrum in the range of wavelengths 1–4 μm. The species responsible for the absorption bands detected in our NACO spectrum are marked in the figure. No object flux is measured in the atmospheric band between 2.5 and 2.8 μm.

A brief search for Pluto's moonlets

At the time of our NACO observations, Pluto's satellites, Hydra and Nix, had yet to be discovered (Weaver et al. 2006). Although the direct images of the Pluto-Charon system, taken with NACO for the slit acquisition of the binary, were never meant to be searched for the very faint new moonlets, we made an attempt to detect them in our few short (3 sec) exposures (see Figure 4). Unfortunately, we didn't find Pluto's new moons in our frames. Given the limiting magnitude of about 18.8 mag determined for our acquisition images, this detection is not surprising since both objects should have *K*-band magnitudes well beyond 21 mag. Longer integrations would have certainly displayed the moons in the NACO images, but would have resulted in a reduction of exposure time for our prime – and only – programme at that time, the spectral analysis of the surface ices on Pluto, Charon, and Triton.

Figure 4: Median average of the slit acquisition images of Pluto and Charon in the night 4 August 2005. The expected positions of the moons Hydra and Nix are indicated by crosses.

References

Brown M. E. and Calvin W. M. 2000, Science 287, 107
Buie M. W. and Grundy W. M. 2000, Icarus 148, 324
Cruikshank D. P. et al. 1993, Science 261, 742
Douté S. et al. 1999, Icarus 142, 421
Grundy W. M., Buie M. W. and Spencer J. R. 2002, AJ 124, 2273
Olkin C. B. et al. 2007, AJ 133, 420
Owen T. C. et al. 1993, Science 261, 745
Palumbo M. E. and Strazzulla G. 1993, A&A 269, 568
Quirico E. et al. 1999, Icarus 139, 159
Weaver H. A. et al. 2006, Nature 439, 943

Arrival of the first Japanese ALMA antenna at the Operations Support Facility (OSF) in July 2007.

Photo: F. Mac Auliffe, ESO

BACHES – A Compact Light-Weight Echelle Spectrograph for Amateur Astronomy

Gerardo Avila[1]
Vadim Burwitz[2]
Carlos Guirao[1]
Jesus Rodriguez[1]
Raquel Shida[1,3]
Dietrich Baade[1]

[1] ESO
[2] Max-Planck-Institut für Extraterrestrische Physik, Garching, Germany
[3] ST-ECF

BACHES is a low-cost, light-weight echelle spectrograph suitable for observations of bright stars coupled with small telescopes up to 35 cm (14″) in diameter. The resolving power reaches 19 000 in a continuous spectral range between 390 and 750 nm. The throughput of the instrument including the telescope and detector is 11 % peak at 500 nm. With this efficiency spectra of stars of visual magnitude 5 can be obtained in 15 min exposure with a S/N of 50. One of the goals of the instrument is to monitor the spectral variability of Balmer emission lines in Be stars.

The availability of key components such as diffraction gratings and high-sensitivity CCD cameras at affordable prices now allows the construction of inexpensive but fairly high-performance spectrographs. A large number of amateur astronomers routinely take spectra of planets, stars, comets and bright extended objects. Thus some years ago we started building low-resolution spectrographs for small telescopes. These models were rather heavy and cumbersome and therefore had to use optical fibres to link to the telescope. FIASCO (FIbre Amateur Spectrograph Casually Organised) was our first prototype. Using a 200 µm fibre linked to a 25-cm telescope, a Peltier-cooled CCD camera and a 600 l/mm grating, we obtained spectra with a resolving power of 600. However, even with this spectrograph we were able to detect the sodium lines in comets Hyakutake and Hale-Bopp in 1996 and 1997 respectively (Avila 1999). Nowadays, the amateur spectroscopy community is moving towards higher resolving power in order to include more ambitious scientific goals, such as surveys of the spectral variability of Balmer emission lines in Be stars and even detection of exoplanets (Kaye 2006).

Following this evolution, we therefore designed an echelle spectrograph light enough to be attached directly to small telescopes. The weight should not exceed 2 kg (without the CCD camera) and the size should be reasonably commensurate with that of typical amateur telescopes. Thanks to the availability of low-cost echelle gratings and light-weight (but still relatively bulky) CCD cameras, we could achieve these objectives. The development of the instrument was a collaboration between a group from ESO and the mechanical workshop for apprentices of the Max-Planck-Institut für extraterrestrische Physik in Garching.

The first light of BACHES took place in September 2006 with observations of bright stars like Albireo and Deneb with a 35-cm Celestron telescope. In March 2007 we initiated observations of Be stars (primarily ζ Tau).

The instrument

BACHES ('pothole' in Spanish) stands for BAsic eCHElle Spectrograph. Figure 1 shows the instrument attached to a 25-cm telescope. A 25 × 100 µm slit engraved in a reflective nickel plate is used to check the position of the star in front of the slit. A Phillips ToUcam webcam monitors the image of the star on the slit plate. A doublet collimates the telescope beam to a 79 l/mm, 63° echelle grating. Then the diffracted beam reaches a diffraction grating acting as cross-disperser. Finally an objective is used to project the spectrum on the CCD. The camera is an SBIG ST-1603ME with an array of 1530 × 1020 pixels of 9 µm. The spectrum is composed of 29 complete orders covering a range between 390 and 750 nm. The instrument has been designed to match F/10 apertures and the slit width projects on to 2.4 pixels. Figure 2 shows the spectrum of a thorium lamp. The measured resolving power ($\lambda/\Delta\lambda$) is between 18 000 and 19 000 over the entire spectral range.

The data reduction is carried out with an adapted version of the ECHELLE package in MIDAS. The process performs the following steps: bias level and dark current subtraction; removal of hot pixels; wavelength calibration with a thorium-argon lamp; extraction of the 1D spectrum; rebinning to wavelength units. MIDAS scripts are used to automate the identification of the thorium-argon lines for

Figure 1: BACHES attached to a Celestron CGE 11″ telescope with a Losmandy Equatorial G-11 mount.

Photo: C. Guirao, ESO

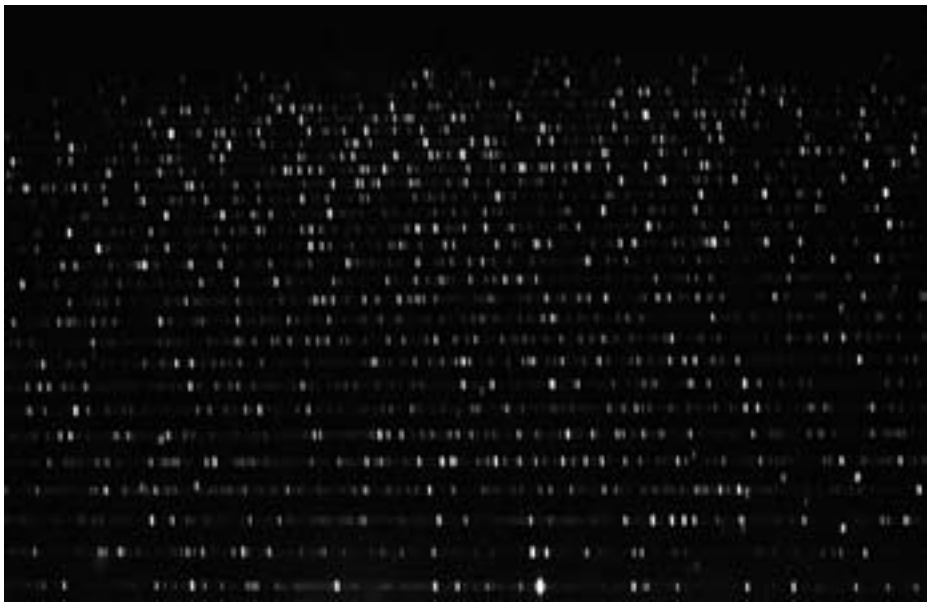

Figure 2: Spectrum of a thorium-argon calibration lamp with a 5 s exposure. 1500 lines are detected and 80 % are typically identified (calibrated) with the MIDAS/ECHELLE calibration procedure.

wavelength calibration and for executing a kind of pipeline. The data reduction package and a demonstration can be found at *www.eso.org/projects/caos/spectrograph/baches.html*. Since MIDAS can run under Windows through the Linux emulator Cygwin/CygwinX, a single computer can be used for both acquisition and reduction of the spectra.

The measured peak throughput of BACHES is 27 % at 504 nm. The quantum efficiency (QE) of the CCD at this wavelength is 52 % according to the data sheet. Assuming a throughput of 81 % for the telescope (corrector plate and 2 Al mirrors), the total throughput from the atmosphere to the detector is 11 %. For comparison the peak efficiency for the red arm of UVES under the same conditions is around 17 %. But for an instrument thousands of times cheaper than UVES, the efficiency is not bad, especially since most of the difference is due to the difference in both the QE of the CCDs used and the echelle grating. On the sky, with our equipment, we can observe stars down to $m_v = 5$ with an exposure time of 900 s and a measured signal-to-noise ratio of around 50 per pixel.

The main problem encountered with this prototype was the relatively poor mechanical stability. In the worst conditions (telescope very low and rotation of the spectrograph through 180 degrees) we observed a shift of the spectrum on the CCD by up to 3 pixels (27 µm). However, the main sources of instability have been identified and will be improved in the next model.

A first step towards scientific application: Variability of Hα and Hβ emission lines in the Be star ζ Tauri

About 10 % of all B-type stars exhibit Balmer (and other) emission lines, which arise from a disc-like circumstellar envelope, composed of material lost by the central B star. How such discs are formed is at most partly understood. But all Be stars are rotating at 90 % or more of their break-up velocity, which must be an important factor. The interplay between ejection mechanisms and dissipative processes in the disc (involving also stellar radiation pressure) often leads to the cyclic build-up and dispersal of the disc, which manifests itself in the appearance and disappearance of the Balmer emission. The spectroscopic monitoring of this variability can reveal important details about the ejection geometry, the circularisation of the ejecta, the geometry and dynamics of the disc, etc., provided the S/N and spectral resolution are sufficient. The nominal performance of BACHES should fully satisfy these requirements. Moreover, there are enough bright Be stars so that at almost any time and location one or more of them are within reach of BACHES. Therefore, the good match between BACHES and Be stars is bidirectional.

In order to verify the suitability of BACHES for such studies, we initiated a series of observations of ζ Tau (HD 37202) with our telescopes. Figure 3 shows the variability of the Hα and Hβ emission lines between 12 March and 25 April 2007. The first spectrum was taken in Garching with our AGAPE telescope, a 35-cm Celestron. At the time of these observations ζ Tau was quite low in the West at an Hour Angle of about 4 hr and the air mass correspondingly high. The spectrum shown is the average of three exposures of five minutes each. The second observation took place on 31 March 2007 in Paranal. Finally, the last two spectra were made in Garching with the AGAPE 35-cm telescope. This time we increased the number of exposures to five (300 s each). As revealed by the extracted spectra, the signal-to-noise ratio is not considerably improved, but 3 × 300 s exposures is enough for an accurate analysis of the hydrogen Balmer lines.

The spectral variability that can be seen in Figure 3 is rather complex. It is different from the variability seen in most other Be stars in that the Hα emission has a triple-peaked profile. ζ Tau is a single-lined spectroscopic binary with an orbital period of 132.97 days, and it is thought that the rich structure of the emission profiles is due to this circumstance. One of the objectives of monitoring ζ Tau in the forthcoming observing season is to search for a relation between the spectral variability and the orbital phase.

These few reconnaissance spectra are already sufficient to demonstrate convincingly that, with bright enough targets and/or large enough (but still small) telescopes, BACHES can satisfy the needs even of relatively demanding scientific research projects.

In summary, BACHES is a light-weight, low-cost, medium-resolution echelle spectrograph suitable for science-driven observations of bright stars and especially for the monitoring of time-dependent phenomena. A spectral resolving power of 18 000 is fully adequate for many scientific purposes. Its simplicity and low manufacturing cost make BACHES affordable for student training courses at universities and for advanced amateur observatories alike. We will continue to quantitatively characterise the properties of BACHES, e.g. the stability of the wavelength calibration, the homogeneity and stability of the point-spread function, the correctability of spectra for the echelle ripple function, etc.

Acknowledgements

We want to thank Marc Sarazin for use of the 28-cm Celestron telescope at Paranal. We also thank ESO PAD who kindly purchased the optics for the spectrograph.

References

Avila G. et al. 1999, Proc. IAU Coll. 173, 235
Kaye T. et al. 2006, J. Br. Astron. Assoc. 116, 2
Pollmann E. 2007, IAU Inf. Bull. Var. Stars, 5778
For a list of spectroscopy amateur web sites see for example: *http://www.astroman.fsnet.co.uk/players.htm*

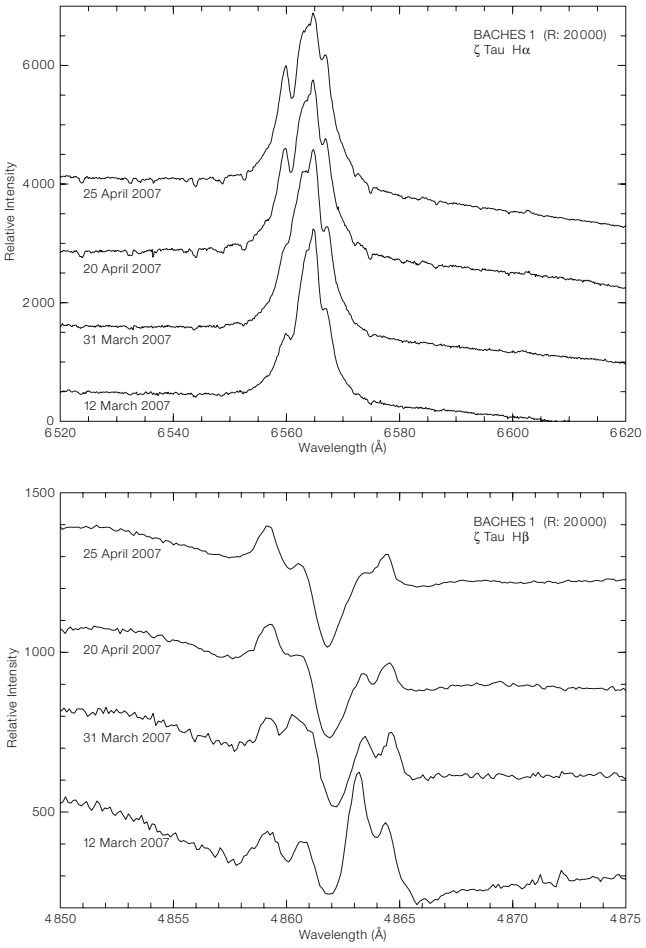

Figure 3: Evolution of Hα and Hβ lines in ζ Tau over 44 days.

Report on the ESO Workshop on

Obscured AGN across Cosmic Time

held at Kloster Seeon, Bavaria, Germany, 5–8 June 2007

Robert A. E. Fosbury[1]
Carlos De Breuck[2]
Vincenzo Mainieri[2]
Gordon Robertson[2,3]
Joël Vernet[2]

[1] ST-ECF, ESO
[2] ESO
[3] University of Sydney, Australia

While the radio-loud, obscured quasars (the radio galaxies) have been known and studied for decades, new and sensitive X-ray and mid-infrared surveys are now beginning to reveal large numbers of their radio-quiet counterparts beyond the local Universe. Consequently, we are approaching the compilation of a relatively complete census of AGN of all types covering a large fraction of cosmic time. This is revealing a remarkably intimate connection between the supermassive black hole and its host galaxy. The workshop reported here was designed to explore the results of these rapid observational developments and the nature of the relationships between the stellar and AGN components.

Introduction

Research areas in astronomy occasionally experience a period of rapid growth due either to the development of some new observational capability or to the si-

multaneous ripening of several related threads of understanding. In the case of the relationship between supermassive black holes (SMBH) and the growth of their host galaxies, we are in the midst of such a revolution triggered by the combination of both of these effects. While the close connection between the black-hole mass and the mass (velocity dispersion) of a galaxy bulge – the 'M-σ' relation – has been known since the late 90's, the mapping out of a comprehensive picture of black-hole demographics had to await the deep surveys that were capable of detecting both the obscured and the unobscured flavours of active galaxies: the type 2 and type 1 Active Galactic Nuclei (AGN) respectively. The combination of sensitive X-ray and mid-infrared (MIR) observatories in space is now providing just this service by penetrating and/or revealing the obscuration that in type 2 sources hides the nuclear regions in the UV to the near-IR spectrum (see Figure 1 for an example of the X-ray-to-radio SED of a radio galaxy). The results are exciting.

The completion of such a census has substantial cosmological significance since it is providing the foundation for identifying the role of AGN feedback in the galaxy formation process. The type 2 sources are of particular value here since, by acting as their own coronographs, they facilitate the study of the star-formation activity and the investigation of the correlated growth of the black hole and the host galaxy.

While radio galaxies – which are being used to trace the massive galaxy population at all epochs – have been studied intensively for the past 40 years, their more numerous radio-quiet counterparts beyond the local Universe are only now being discovered in substantial numbers. One of the workshop's aims was to bring together the established radio galaxy community with those studying the radio-quiet sources, and so help to elucidate the effects of the (possibly) different host galaxies and environment on the manifestation of the AGN phenomenon.

Advances in capability

Advances in observational capability have been crucial for the rapid development in

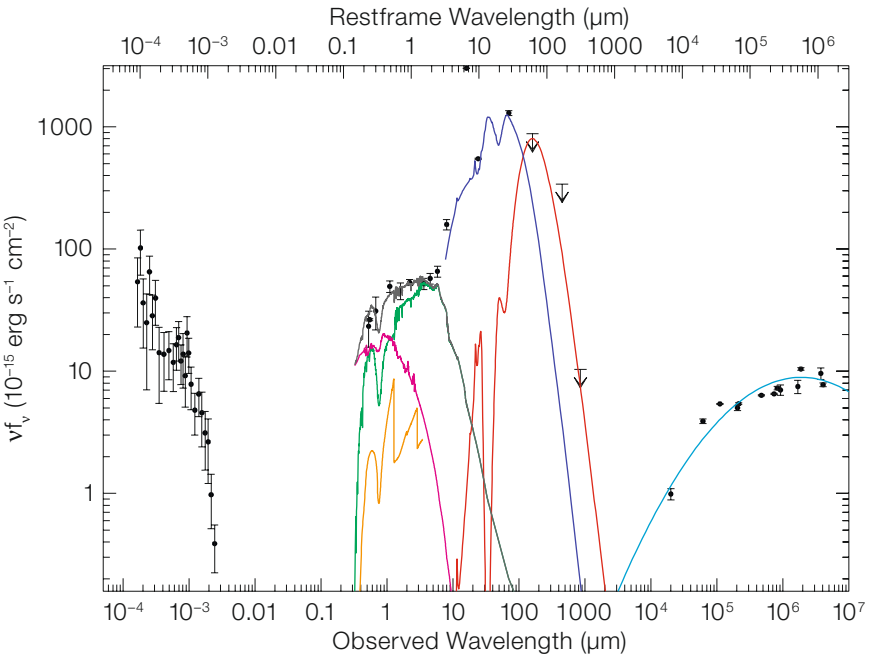

Figure 1: X-ray-to-radio spectral energy distribution (SED) of the z = 2.483 radio galaxy 4C+23.56 (De Breuck et al. in preparation). All data points are observed flux densities, except for the *J*, *H* and *K*-band fluxes, which have been corrected for strong emission lines. Coloured lines show the decomposition of the SED into different intimately-related components. The accretion onto the supermassive black hole creates very energetic X-ray and UV emission and powerful synchrotron radio jets and lobes. In this typical radio-loud, type 2 AGN, the direct view to the nucleus is blocked by an obscuring torus absorbing the soft X-ray radiation that is re-emitted as hot thermal dust emission (blue). Radiation escaping through the torus opening is scattered toward the observer providing a unique periscopic view of the nucleus (magenta). It also ionises the ISM producing nebular continuum emission (orange) and, of course, line emission (which is not shown). The massive stellar host galaxy is seen directly in the rest-frame near-IR (green), while an obscured starburst is revealed by sub-mm cool dust re-emission (red). The radio synchrotron fit is in cyan. The bolometric contributions from the accretion onto the supermassive black hole and the stellar nucleosynthesis are remarkably similar.

understanding that we are witnessing. The ability to locate and identify the radio-quiet type 2 objects has depended on the concerted use of both the X-ray and the MIR emissions that derive their energy from the AGN either directly or through re-emission. We have known for a long time that optical and near-infrared (NIR) radiations emerge from the AGN in a highly anisotropic manner. However, the X-rays – especially at higher energies – and the MIR are believed to emerge in a more isotropic manner. This enables surveys using these wavebands to find a much more complete set of AGN, regardless of their orientation in space or distribution of their obscuring material.

The sensitivity of the spaceborne instruments is such that active galaxies, at least the more luminous examples, can be seen out to the highest redshifts. The wide field, sensitive ground-based surveys are playing their part as well. The SDSS has revealed very large numbers of AGN (see, for example, Figure 4), including the few QSOs with the highest known redshifts. The deep, narrower field, multi-wavelength surveys such as HUDF, GOODS, GEMS, COSMOS, etc. are mapping relatively small areas at unprecedented depth and producing samples of fainter AGN. The deepest X-ray surveys are reaching AGN source densities of 7000/deg^2, with more than half of these being partially obscured in X-rays. These surveys are allowing, now more than 40 years after its discovery, a huge step forward in the understanding of the origin of the X-ray background (XRB). They confirm the prediction of the population synthesis models which explain the XRB spectrum as the emission, integrated over cosmic time, of obscured and unobscured AGN. Most of the XRB emission below 10 keV is resolved into unobscured

and Compton-thin AGN. These sources, however, fall short of matching the XRB peak intensity at 30 keV, which can instead be accounted for by a large (as numerous as that of Compton-thin AGN) population of heavily obscured, Compton-thick objects.

At the very limits of detection, the stacking of sources detected in one waveband in order to characterise the average behaviour in another can be remarkably illuminating. For instance, the stacking of faint MIR sources reveals a hard X-ray spectrum indicative of large absorbing columns.

One obvious question which arises from this new survey capability is whether we discover any qualitatively new type of source? The answer seems to be not really, although there are certainly objects turning up with AGN characteristics in some wavebands that appear rather boring in some of the more traditional windows.

Studies of individual sources benefit from the sheer power of the large ground-based telescopes, more recently coupled to Integral-Field Spectrographs (IFS) fed with AO. The astonishing detail with which the hosts are now being studied was one of the clear highlights of the workshop. Kinematic maps, analyses of stellar populations and element abundances from the spatially resolved ISM emission lines are all active new fields. Particularly exciting was the application of the VLTI to imaging the obscuring torus in nearby sources.

Nature of obscuration

The type 2 (obscured) AGN were always recognised as being a heterogeneous bunch, even after the orientation-dependent unification scheme had become firmly established following the detection, in the 'true' type 2s, of the hidden type 1s in polarised light. Observers in different wavebands contributed to the confusion by using their own set of selection criteria. It was clear that the 'true' type 2s were obscured by some coherent structure that was identified as an equatorial 'torus' that would absorb UV/optical/NIR light over more than half the sky as seen from the central BH. There was always a suspicion however – now amply confirmed by observations – that, lurking within the class, some objects were being obscured instead by larger-scale structures within the host galaxy. Distinguishing these pseudo type 2s is being done using an arsenal of techniques. In contrast to the torus, the extended obscuration usually has a rather small A_V (a few, but enough to hide the BLR). It is also Compton-thin, unlike some (parts) of the tori. A clear indicator of a proper torus, however, is provided by a MIR signature of hot dust over a range of temperatures up to that of dust sublimation. But perhaps the most striking recent result is the spatial resolution in the MIR – using MIDI on the VLTI – of structures that can be identified with the warm torus material in Circinus (Figure 2) and NGC 1068. As expected, these are oriented perpendicular to the ionisation cones and outflows. In Centaurus A, however, the MIR emission is unresolved and can probably be associated with synchrotron emission from the footprint of the jet.

Another fascinating observation, illustrated with X-ray monitoring observations of NGC 1365, involves watching a Compton-thin cloud moving at about 10^4 km/s eclipsing the nuclear X-ray source – having a size of less than ~ 10^{14} cm – over a period of about two days. During the eclipse, the broad iron emission line disappears while strong iron absorption lines are seen. This source size corresponds to about 10 Schwarzschild radii for a BH with a mass ~ 3×10^7 $M_\odot$.

Our conception of the form of the torus has been derived from many artist's impressions, but what really shapes it? Even a sub-Eddington AGN can produce a radiative force that is comparable to gravity in the material that would comprise a torus. The opacity in the MIR can be some 10 to 30 times that from Thompson scattering, making it possible to support a geometrically thick obscuration. In addition to regular doughnuts, clumpy or otherwise, with radial temperature gradients and gradients within clumps, the old idea of warped discs is still there in the running. We know that such structures exist because we see them, albeit on larger scales, in a number of galaxies.

So what fraction of the type 2s are simply type 1s which happen to be pointing away from us? Well, the prevailing opinion seems to be that about half of them are really of the 'host-obscured' variety that will reveal their AGN to an observer with only a modest degree of determination. There are, however, powerful, deeply obscured sources – ULIRGs – that can fight hard not to reveal their power sources. The debate always used to be: "Are they AGN or Starburst powered?" Now we are more likely to ask about the current balance between these two intimately-related processes.

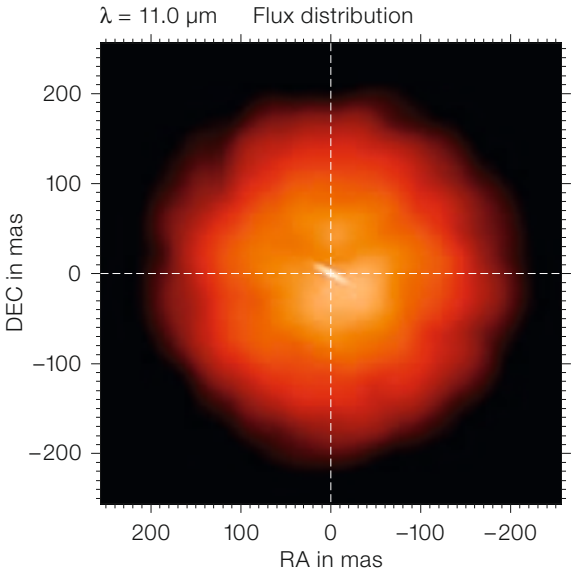

Figure 2: Flux distribution of the emission from warm dust in the nucleus of the Circinus galaxy. The emission was modelled according to interferometric data obtained with MIDI at the VLTI using two elliptical, Gaussian blackbody emitters with silicate absorption. The dust is distributed in two components: (1) a small, disc-like component which is oriented perpendicularly to the ionisation cone and outflow and coincides with the orientation and size of a maser disc; (2) a larger torus which surrounds the disc component and which shows strong evidence for clumpiness. This finding strongly supports the unified scheme of AGN. (Courtesy Konrad Tristram, MPIA)

The astrophysics of all this obscured and obscuring material deep within galaxies has been given a tremendous boost by the availability of exquisite MIR spectroscopy, first with ISO and now with Spitzer (Figure 3). There are many diagnostics in this spectral region, from the permitted and forbidden ionic lines, familiar from their shorter wavelength counterparts, gas-phase molecules like CO, C_2H_2, HCN, etc., water ice, hydrocarbons (both aromatic and aliphatic) and silicates in dense molecular clouds. Whole new families of 'diagnostic-diagrams' can be constructed in this playground. One example, with silicate absorption/emission strength plotted against the PAH equivalent width, nicely separates different types of AGN and star-bursting regions.

Examinations of orientation-based unification, e.g. the 'Jackson-Browne' test which compares the isotropic emissions from types 1 and 2 sources in matched samples, have been given fresh impetus by the availability of new candidate isotropic AGN emissions in the MIR. By using forbidden line ratios, such as [Nev]/[Neii] and [Nev] to low-frequency radio power for a matched sample of FRII radio galaxies and quasars, the test is passed with flying colours. This confirms that these types 1 and 2 objects are indeed from the same parent population and also, incidentally, that the [Oiii] 5007 Å line that was used in the original test is partially obscured in the type 2 objects – as has been suspected for a long time.

Environments

One of the historical values of AGN has been their utility as 'markers' of distant galaxies and (proto-)clusters. Due to their high visibility, the powerful radio galaxies have long served such a purpose. It is hypothesised, on the basis of their position in the observed *K*-band Hubble diagram, that these sources indicate the presence of massive hosts. The availability of sensitive MIR measurements from Spitzer has now made it possible to confirm this hypothesis using measurements of the restframe *H*-band luminosity which is relatively insensitive to AGN contamination and can be easily corrected for its small residuals. These sources are also serving as signposts to protoclusters

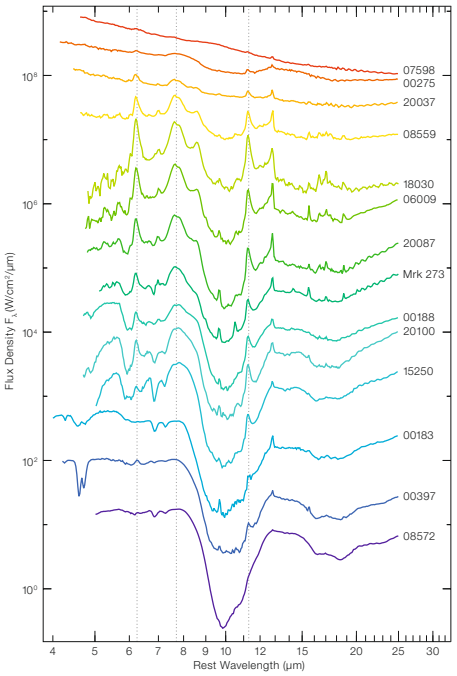

Figure 3: This collage of low-resolution Spitzer-IRS spectra offers a striking illustration of the diverse nature of the galaxies classified as ultraluminous infrared galaxies (ULIRGs). The reddish spectra at the top are nearly featureless, typical of AGN-heated hot dust. Further down, the family of PAH emission features at 6.2, 7.7, 8.6 and 11.3 microns start to appear, indicating an increased contribution of star-forming regions to the ULIRG spectrum. The PAH emission starts to dominate in the greenish spectra, while silicate absorption at both 10 and 18 microns becomes apparent. In the spectrum of IRAS 20087, the characteristic absorption edge of water ice at 5.7 microns starts to appear as well, indicating the presence of shielded cold molecular clouds along the line of sight. The water ice feature deepens and the importance of PAH emission decreases moving down to the spectra shown in glacial blue. At the same time, the depth of the 10 and 18 micron silicate features increases and hydrocarbon absorption bands at 6.85 and 7.25 microns become apparent, indicating that the power sources of these ULIRGs are deeply embedded. The bottom three spectra differ from those directly above by the presence of a strong near-infrared continuum and by the relative weakness of the 5.5 to 8.0 micron absorption features. Note how, due to the appreciable redshifts of IRAS 00183 and IRAS 00397, the IRS spectral coverage extends all the way down to rest frame wavelength of 4 microns, facilitating the discovery of wide absorption features due to warm CO gas at 4.6 microns in their spectra. (Spoon et al. 2006; Spoon et al. 2007).

at redshifts beyond the reach of other cluster-finding methods. Multi-band photometry can then enable searches for overdensities of sources showing the characteristics, e.g. SED shapes and/or Ly-α emission, expected for 'cluster' members.

Very extended Ly-α halos (≳ 100 kpc) indeed appear to be ubiquitous attendants of such objects and they provide information about sources of ionising radiation and about large-scale gas flows in galaxies early in their evolutionary histories. In addition to those seen around the radio galaxies, Ly-α emission is now being detected around some of the radio-quiet sources, especially those seen at sub-mm wavelengths.

Feedback

The natural theme of the workshop – and indeed the reason for the resurgence of interest in AGN in general – is the rapidly growing evidence for the intimate relationship between the SMBH and the host galaxy, first evinced from the 'M-σ' relationship. That such a relationship exists was perhaps hinted at by the similarity of the bolometric luminosities originating from nucleosynthesis and from collapse onto black holes through the history of the Universe. The actual ratio of these two contributors as a function of cosmic time is something that will be derived as a result of the complete AGN census which we have been describing, but we have known for quite a while that the numbers are roughly comparable. Why should that be so? The physics of energy generation in these two cases is, after all, quite different.

The answer must be that the processes know about one another and are able to communicate by some kind of feedback mechanism. Now, while 'feedback' may be a euphemism for all the physics that we do not understand, we can at least see the results of its operation. AGN seem to be able to switch off cooling flows in clusters and stop star formation in galaxies with the result that the BH mass is tied to that of the host bulge (or vice versa). Indeed, it is remarkable that the cosmic evolution of the star-formation-rate density is so closely mirrored by that of the BH accretion-rate density. This conclusion has been strengthened recently by several observations. One is the use of a simple, but apparently effective, proxy for BH bolometric luminosity, name-

ly the 'relatively-raw' [O III] 5007 Å luminosity AGN from the Sloan survey (see Figure 4 for an example of a line-ratio diagnostic (BPT) diagram from Sloan data). Another comes from deep X-ray surveys showing that the space density of the less luminous AGN peaks at lower redshifts than that of high X-ray luminosity QSOs. This behaviour is driven by a decrease in the characteristic mass scale of actively accreting black holes as shown by the SDSS data.

So the 'downsizing' seen in the growth of galaxies is seen also in the accretion rate onto black holes. There are two parts to this problem: one is the question of accretion rate and the associated growth of the BH; the other is the effect of the AGN on the host galaxy and its environment.

But how does the feedback actually work? Understanding this is a demanding problem for both observers and theorists. The feedback can be either negative – by the driving of outflows – or positive – from jet- or supernova-driven star formation arising as a result of gas compression. There is evidence from several different wavebands for outflows on various scales. The Ly-α halo kinematics also present evidence for inflowing gas. The powerful radio sources appear to be very effective at large (cluster) scales by preventing cooling flows. With their huge mechanical energies, comparable to the bolometric luminosity, these jets can do more than just prevent cooling, they can remove gas entirely: we can see them excavating huge, buoyant cavities within the surrounding halos of hot, X-ray emitting gas. For the lower luminosity AGN, the influence is felt on smaller scales but the BH seem to be able do a good job of controlling the growth of the bulge.

How to grow massive enough BHs at early enough times – the Sloan $z \sim 6$ QSOs contain SMBHs – is not easy to understand. It seems to be possible, just. But there is little room for inefficiency. The wonderfully detailed studies of our own Galactic BH show just how difficult it is to get mass accretion working. Mergers clearly can play a part in getting mass down to the nucleus but this is certainly not the only mechanism. Local AGN

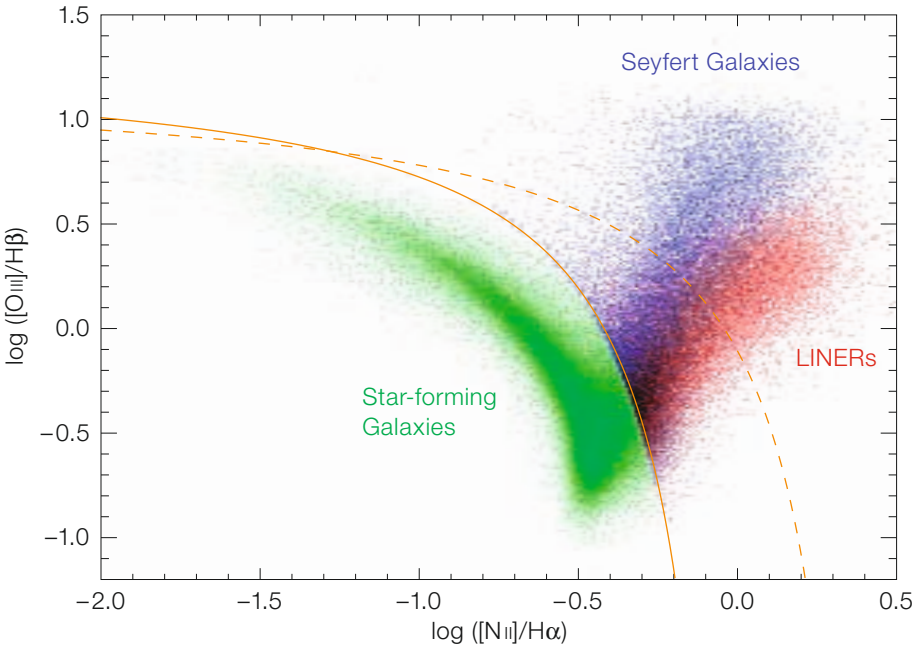

Figure 4: This figure reveals the spread of emission-line galaxies from the Sloan Digital Sky Survey (SDSS) on the line ratio diagnostic diagram of Baldwin, Phillips and Terlevich (1981). This diagram uses four strong optical emission lines, [O III] 5007 Å, [N II] 6583 Å, Hα 6563 Å, and Hβ 4861 Å, to distinguish galaxies that are dominated by ionisation from young stars (labelled "Star-forming Galaxies"), from those that are ionised by an accreting supermassive black hole in the nucleus (Seyfert and LINER galaxies). The SDSS galaxies not only enable us to see the possible extent of emission line galaxies but also to distinguish the dominant ionisation mechanism for this observed spread (Kewley et al. 2006). The curves indicate empirical (solid) and theoretical (dashed) dividing lines between active galactic nuclei (AGN) and star-forming galaxies, based upon the SDSS observations (Kauffmann et al. 2003) and MAPPINGS III photoionisation models (Kewley et al. 2002).

appear to be fed routinely from massive discs containing rich reservoirs of cold gas.

Future

How do we expect the field to develop in the near future? This is always a risky thing to predict. It is safe to say that the surveys will continue to pay a big dividend towards the understanding of the BH demographics over the entire history of the Universe. Detailed, sensitive and high-resolution observations with the large telescopes will flesh out our primitive understanding of the feedback mechanisms that maintain the balance between stars and BH. We may even reach the point of being able to replace the famous Padovani/Urry AGN cartoon with a real image of the torus and the associated components of the SMBH environment! We also await the capabilities of ALMA to map the cold gas and its motions at small spatial scales to see if this gives insights into the flows of material to the nucleus. Finally, we note that this report is being written just as the observation of the first directly observed (20 year) stellar orbit around our Galactic BH nucleus is being completed.

References

Baldwin J., Phillips M. and Terlevich R. 1981, PASP 93, 5
Kauffmann G. et al. 2003, MNRAS 341, 54
Kewley L. et al. 2002, ApJS 142, 35
Kewley L. et al. 2006, MNRAS 372, 961
Spoon H. et al. 2006, in "Astrochemistry: Recent Successes and Current Challenges", eds. D. C. Lis, G. A. Blake and E. Herbst, IAU Symposium 231, 281
Spoon H. et al. 2007, ApJ 654, L49

Conference web site: *http://www.eso.org/agnii2007*

Report on the ESO Workshop on

12 Questions on Star and Massive Star Cluster Formation

held at ESO Headquarters, Garching, Germany, 3–6 July 2007

Markus Kissler-Patig[1]
Tom Wilson[1]
Nate Bastian[2]
Francesca D'Antona[3]
Richard de Grijs[4]
Dirk Froebrich[5]
Emmanuel Galliano[6]
Preben Grosbøl[1]
Kelsey Johnson[7]
Eric Keto[8]
Ralf Klessen[9]
Tom Megeath[10]
Marina Rejkuba[1]
Jürgen Steinacker[11]
Hans Zinnecker[12]

[1] ESO
[2] University College London, United Kingdom
[3] Osservatorio di Roma, Italy
[4] University of Sheffield, United Kingdom
[5] University of Kent, United Kingdom
[6] Universidad de Chile, Santiago de Chile, Chile
[7] University of Virginia, Charlottesville, Virginia, USA
[8] Harvard-Smithsonian Center for Astrophysics, Cambridge, Massachusetts, USA
[9] Universität Heidelberg, Germany
[10] University of Toledo, Ohio, USA
[11] Max-Planck-Institut für Astronomie, Heidelberg, Germany
[12] Astrophysikalisches Institut Potsdam, Germany

The Workshop "12 Questions on Star and Massive Star Cluster Formation" was held in Garching from 3 to 6 July 2007. The programme was set up to allow long (and fruitful) discussions around several questions connecting the formation of stars and star clusters. Here we summarise some of the discussions, and encourage interested readers to download the contributions from *http://www.eso.org/star07*.

In view of the booming fields of star formation and star-cluster formation, we had thought, back in mid-2006, to organise a meeting that would bring these two communities together. To an outsider, star formation and star-cluster formation might look like one and the same thing, yet these two communities rarely interact for various reasons. The main one is probably the distance of the studied objects. Star formation can be studied in great detail close-by, i.e. in our Milky Way where distances are expressed in parsecs, and the studied regions enclose typically a few hundred stars. In contrast, suitable targets for studying the formation of massive star clusters are only available in neighbouring galaxies and distances to them are rarely smaller than a few million parsecs – the studied objects enclose up to hundreds of millions of stars. The scales in which the two communities typically think are thus different and the time had come to try to connect them. Further, ALMA – the large sub-mm array – is now within reach and will boost both fields, exactly allowing to connect the two scales thanks to an increased sensitivity and angular resolution.

The format we have chosen for the workshop was a new one: we built the programme of the workshop around a number of questions to be addressed in dedicated sessions. We summarise here some (not all) of the discussed points. All presentations are available for download from the workshop web site *www.eso.org/star07.*

"How are the stellar and cluster initial mass functions related and how are they influenced by the star-formation history?"

The first question of the workshop was posed and introduced by Marina Rejkuba. It is an indisputable fact that star formation is hierarchical. The empirical evidence indicates that the initial mass function (IMF) of young embedded stellar clusters is a universal power law with a slope of 2.0, and that the stellar IMF follows a universal segmented power law in many different environments. The validity of the power-law form for the IMF was questioned in the discussion, but opinions remain divided. The theoretical arguments for the universal stellar IMF were presented by Ralf Klessen, while Hugues Sana and Jorge Melnick showed the pitfalls and problems in empirical determination of the stellar IMF in clusters and in the field. Andrés Jordán discussed the form of the initial old cluster-mass function.

The fact that the clusters undergo mass-loss and disruption on short timescales, leads to the composite nature of the field-mass function. Whether this composite IMF is steeper, or has the same slope as

Figure 1: The conference delegates collected in the entrance hall of the ESO Headquarters in Garching.

the star cluster IMF, has been shown to depend on the answer whether 20 clusters with 10^4 $M_\odot$ can produce the same IMF, with the same maximum stellar mass, as one cluster with 2×10^5 $M_\odot$. With respect to this point the two major theoretical works of Elmegreen and of Weidner and Kroupa disagree. Unfortunately, due to the often poorly known star-formation history of the observed field, and the problems to establish the frequency of binaries in the population, the observational evidence seems to be still inconclusive. Until the errors of the IMF derivation can be reduced, the question remains open.

"What are the effects of stellar feedback?"

In this session negative feedback effects, namely the destruction of clusters, were addressed. During the collapse and fragmentation of a molecular cloud into a star cluster, only a modest amount of the gas is turned into stars. The stellar winds, photoionisation, and supernovae from massive stars inject enough energy into the gas to remove it extremely rapidly (in less than a dynamical crossing time). This rapid gas removal can leave a cluster significantly out of equilibrium. If the star-formation efficiency is low enough (~ 30 % of the initial fraction of gas turned into stars) the entire cluster can become unbound.

Nate Bastian reviewed the physics and some recent observations of this process. In particular he discussed recent N-body simulations of the effects of gas removal on the early evolution of clusters. He also reviewed recent attempts to quantify the amount of infant cluster mortality, with most studies finding values of 60–90 % of young clusters being disrupted in the first 40 Myr of their lives. Sabine Mengel focused on the young massive cluster Westerlund 1 in the Galaxy. She concluded that the star-formation efficiency of this cluster was quite high (> 60 %). Dieter Nürnberger concentrated on another young massive cluster in the Galaxy, namely NGC 3603. On the basis of multi-wavelength observations he pointed out that this cluster is part of a much larger area of star formation. He also showed examples of how the high-mass cluster stars affect the ISM and the young sources in their neighbourhood.

"What is the demographics of star formation in our Galaxy and others?"

In studies of galactic star formation, young stars have traditionally been separated into two demographic groups: isolated stars and clustered stars. This picture is evolving for many reasons. Tom Megeath posed this question. He showed Spitzer surveys of the giant molecular clouds in the nearest 1 kpc revealing the presence of large clusters, small groups, and large numbers of relatively isolated stars. These surveys suggest that isolated stars and dense clusters are extremes of a continuum. Galactic studies provide the opportunity to study physical processes in great detail and trace the distribution of low-mass stars which dominate the mass but are undetected in extragalactic observations. Detected extragalactic clusters are much more massive than clusters near the Sun such as the Orion Nebula Cluster. Frédérique Motte suggested that our Galaxy contains large clusters which overlap with the continuum of observed extragalactic ones. Arjan Bik presented a programme to obtain infrared spectroscopic maps of young embedded clusters in our Galaxy; infrared spectroscopy of the massive stars are needed to determine the membership, age and size of these highly reddened Galactic regions.

Finally, there was a discussion of how best to characterise the clusters, associations and complexes of star formation in our Galaxy and others. Nate Bastian introduced the minimum spanning tree analysis (see Figure 2) and applied this to Spitzer surveys of nearby molecular clouds and the distribution of OB stars in other galaxies. This analysis suggested hierarchical structure with no preferred scale. Mark Gieles showed a minimum spanning tree analysis of the Small Magellanic Cloud where they segregated sources by age. The youngest stars showed clear hierarchical structure while the distribution of the oldest stars was indistinguishable from a random structure, indicating that structure is erased as the stars migrate from their birth sites. In summary, the discussion of this question motivated the need to find Galactic analogues of extragalactic clusters and associations. Furthermore, it demonstrated the need for new methodologies for analysing structure on many different spatial scales, such as the minimum spanning tree or wavelet-based multi-resolution techniques.

"How did star formation proceed in Globular Clusters?"

In recent years, research on these very old systems has shown that they are not the 'simple stellar populations' we thought they were; this topic was introduced by Francesca D'Antona. There is precise spectroscopic evidence that chemical anomalies are present, generally involving about 50 % of the stars in each globular cluster (GC). Anomalies are found in practically all clusters observed so far. Anomalies are also present among unevolved stars, so that they cannot be imputed to 'in situ' mixing in giants. In particular, sodium is enhanced and oxygen depleted with respect to the normal values in the field population II. This, in the end, means that about half of the stars in the clusters (a second generation) are born from matter contaminated by

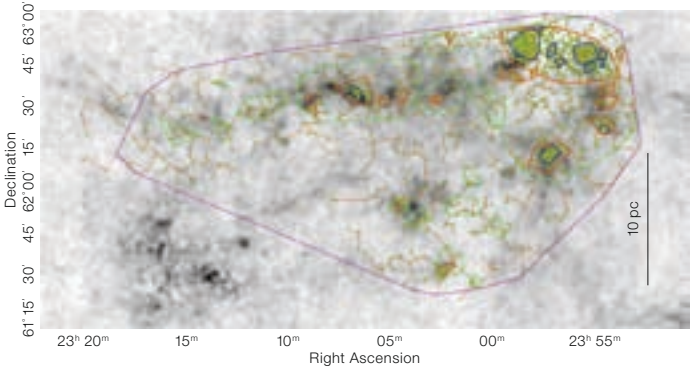

Figure 2: Example of a minimum spanning tree, presented by Nate Bastian and collaborators, revealing the hierarchical structure of star formation (Figure courtesy Gutermuth et al., in preparation).

products of hot CNO burning in stars of the first generation, but not by supernova ejecta, as the metallicity stays constant. The culprits may be the ejecta of massive Asympotic Giant Branch (AGB) stars, as pointed out by Paolo Ventura, or even the envelopes of massive rotating stars, as presented by Thibaut Decressin. The two suggestions imply very different time scales for the formation of the second stellar generation (a few million years, or many tens of millions of years after the formation of the first-generation stars). The number ratio of the two generations, however, implies that the first generation in the pristine globular cluster must have been much more massive (by a factor of 5–10) than today's globular clusters, and this may provide us with hints about how to model the second stage of star formation. Additional evidence of nuclear processed matter is the presence of stars with helium content higher (and even much higher, implying an incredibly high slope of the He enrichment function dY/dZ) than the standard Big Bang abundances. Beautiful observations of splitting of the main sequences in two clusters were presented by Antonino Milone, on behalf of Giampaolo Piotto's group. This view was enlarged to consider low-mass dwarf galaxies by Michael Hilker.

"What governs protostellar mass accretion?"

The physical processes at work in the main mass accretion phase during the process of star formation were presented initially by Dirk Froebrich. In particular, the question of what are the main physical forces and/or initial conditions responsible for converting the observed core mass distribution into the stellar IMF was discussed. It became apparent during the discussion that, beside gravity, the initial specific angular momentum of the core most likely is the main influence on the time dependence of the mass-accretion rate onto the central object. In turn this is, together with the structure of the object, what determines the time evolution of the protostellar observables (e.g. T_{bol}, L_{bol}). Magnetic fields are considered to also be important in determining the accretion rates, which reach much higher values than predicted by self-similar collapse solutions. Further impact on the time evolution of the objects might come from competitive accretion. However, no agreement could be reached on how to interpret the observational evidence.

"How does spiral structure affect star formation?"

Preben Grosbøl drew the attention back to extragalactic objects. Many grand-design spiral galaxies display a concentration of HII regions and OB associations in their arm regions. The increased number of very young sources in the arms suggests an enhanced star-formation rate which could partly originate from a higher surface density in the arms due an underlying density wave. On near-infrared *K*-band images of late-type spiral galaxies, one frequently observes bright knots aligned along the arms. The colours of these knots indicate that they are very young, massive stellar clusters. The number and brightness of such sources correlate with absolute magnitude and spiral perturbation of the host galaxy. The alignment is seen mainly in the galaxies with strong spiral arms, suggesting a triggering mechanism associated with the underlying density wave. This could support a scenario in which young, massive clusters are disrupted in an early phase, since fainter, aging clusters are not observed downstream, as expected due to the relative motion between material and wave.

"How important is 'primordial' mass segregation in the context of massive star cluster formation and evolution?"

This question was posed by Richard de Grijs and led to a controversial discussion. Observations of young clusters in the local Universe show that almost every single cluster is significantly mass segregated, out to radii well outside their cores. This is particularly puzzling for the youngest star clusters, given that their ages are often only a fraction of the timescales required for dynamical effects to become significant on cluster-wide scales. If there is significant, possibly 'primordial', mass segregation within a cluster at the youngest ages, and hence a possible spatial dependence of the IMF (i.e., in the sense of preferential formation of the more massive stars in higher-density environments), this will have important consequences for the accuracy of the physical output parameters.

Joana Ascenso challenged this view. From a series of Monte Carlo realisations of non-segregated synthetic clusters with a standard IMF and a surface density distribution, she performed the 'standard' mass-segregation analysis. Surprisingly, she found a similar degree of 'primordial' mass segregation as claimed in the observational studies of de Grijs and Gouliermis for young clusters in the Large Magellanic Cloud, by Espinoza in the Galactic Centre Arches cluster, and by Brandner in Westerlund 1. Enrico Vesperini used extensive N-body simulations to show that early mass segregation in young clusters may have a dynamical origin. Despite the animated discussion following these thought-provoking presentations, the jury is still out on the basic underlying question of the importance or even the reality of primordial mass segregation.

"What is the relationship between the properties of star clusters and the environments from which they form?"

The environment of massive star-cluster formation is determined by a large number of parameters, including pressure, density, temperature, turbulence, magnetic fields, metallicity, gas content, galactic rotation (or lack thereof), and triggering mechanisms. Of course, many of these parameters are not orthogonal. The challenge, posed by Kelsey Johnson by this question, was to ascertain which of these parameters can essentially be neglected and which may have a significant impact on the properties of the resulting cluster(s). For example, one might expect metallicity to play a role in the properties of the resulting cluster, yet the few observed ultralow metallicity systems (e.g. IZw18, SBS0335-052) show very diverse modes of cluster formation, suggesting that metallicity (at least down to this abundance) does not play a dominant role. Detailed studies of the relation between specific frequency of globular clusters and galaxy type may provide important insight. However, this is a blunt tool, and raises the challenge of relating the role of macroscopic phenomena to local physics. A re-

current theme in the presentations of this session has been the importance of star-formation efficiency to cluster formation. However, this then begs the question of what primarily determines the star-formation efficiency. On the macroscopic scale, perhaps the most plausible answer is pressure, but it is not yet clear what subtleties, which may have a secondary role, are hiding in the microphysics; we must keep in mind that star formation is a local process. Although it is currently the fashion to accumulate large data sets with impressive statistics, in-depth case studies are still critical if we wish to disentangle all of the ingredients affecting massive star and star-cluster formation.

Figure 3: A massive star-forming region, presented by Eric Keto, illustrating massive accretion flows. The figure shows an overlay of contours of emission from molecular gas on a background image of mid-IR emission from Spitzer Space Telescope data. The central cloud encloses a particularly massive flow of 10^3 $M_\odot$/yr into the centre of the star cluster seen in the IR. The innermost contour is about 30″ in diameter (0.9 pc at 6 kpc).

"Which physics determine the stellar upper mass limit?"

Finally, Hans Zinnecker, Eric Keto, Carsten Weidner and Hugues Sana set out to answer this question. The most massive stars in the Galaxy are typically found in a group of several similar stars at the centre of an OB cluster, for example, the Orion Trapezium. When we look at a very young, embedded OB associations still in formation, such as G10.6-0.4, we see a massive molecular accretion flow into the centre of the cluster. Thus we expect the most massive stars in the Galaxy to form at the centres of such cluster-scale accretion flows (see Figure 3). The accretion velocities indicate that the flow is a 'cooperative accretion flow' drawn by the cooperative gravitational pull of the combined mass of several O stars at the cluster centre. Within a few thousand AU of the O stars, the molecular accretion flow becomes ionised, but continues in toward the cluster centre because the escape velocity from the co-op of the stars exceeds the ionised sound speed. The ionised accretion flow spins up into an ionised accretion disc at the cluster centre. Because the dust that was originally in the molecular accretion flow is destroyed by the high temperatures and densities in the disc, accretion can continue onto the individual stars in the co-op, unimpeded by the intense radiation pressure on dust. Secondly, in the fully ionised flow there is no outward pressure between the hot ionised and cold molecular gas to impede the flow. Thus the cluster-scale cooperative accretion flow sets up these two conditions that allow accretion onto very massive O stars despite the presence of outward forces of radiation and thermal pressure. The observational evidence, and more of the physics of the upper stellar mass limit, are reviewed in the recent Annual Reviews of Astronomy and Astrophysics article by Zinnecker and Yorke.

Overall, the workshop certainly left us with more questions than answers, but the format was a success as the workshop was dominated by long and fruitful discussions. The two communities working on star formation and star-cluster formation moved a step closer towards each other and there is good hope that they will merge in the epoch of ALMA.

Acknowledgements

We wish to acknowledge Christina Stoffer, who managed all the logistics of the workshop, as well as Arjan Bik for his help in the local organising committee.

Announcement of a Workshop on

Science from UKIDSS

17–19 December 2007, ESO Headquarters, Garching, Germany

The workshop will take place a few weeks after the UKIRT Infrared Deep Sky Survey (UKIDSS) large Third Data Release (DR3). The purpose of the workshop is to provide a forum, bringing together European astronomers working on (or planning to work on) UKIDSS data, to hear about science being undertaken with UKIDSS, and to share knowledge gained in working with the data and ideas for exploiting the archive efficiently, in an informal atmosphere. The emphasis will be on work in progress. The workshop will include science and technical talks, and tutorials, as well as a summary of the current status of the surveys, and an opportunity to discuss the future direction.

Registration will be open from 15 September 2007 at *http://www.ukidss.org/esoworkshop.*

Observing at ESO: a New Procedure for Target and Instrument Set-up Changes

Francesca Primas, Petra Nass, Olivier Hainaut, Michael Sterzik (all ESO)

As stated in the ESO Call for Proposals, targets and constraints requested at time of proposal submission (i.e. at Phase 1) are binding, because once the proposals have been evaluated by the Observing Proposal Committee, the requested targets and constraints become one of the major inputs to finalise and optimise the scheduling of the telescopes. However, part of the success of an observatory comes also from the ability to balance operational efficiency (hence rules and procedures) and scientific return. In other words, target and/or instrument set-up changes are allowed also after Phase 1, but only after they have been carefully scrutinised. Their approval is subject to the following conditions:

a) all requests must be accompanied by a sound and robust scientific justification;
b) no conflict is found with already approved (thus protected) targets/set-ups from other programmes;
c) the impact on the telescope schedule due to the requested change is insignificant.

Until recently, requests for target/set-up changes/additions were handled manually, via the submission of an e-mail to the observatories (for Visitor Mode runs), to the User Support Department (for Service Mode runs), sometimes even via an e-mail to private accounts. In order to have a better overview of the requests and properly log them in one central place, we have now developed and deployed a new web-based form for the submission of these requests, which is available at *http://www.eso.org/observing/p2pp/ProgChange/.*

As for other services we provide (e.g. Service Mode run status progress report pages), access to the form requires a P2PP (Phase 2 Preparation tool) password and valid run ID, and the selection between a target or an instrument set-up change. Once the user and the run are verified, the list of the Phase 1 targets is displayed and a few fields need to be filled out: a scientific/technical justification in support of the request; coordinates of the new targets or the newly requested instrument set-up. If the change request is for targets, users also need to specify a target type, to be chosen among: REPL = replacement (when they wish to discard and replace one or more of their Phase 1 targets); ADDI = additional (if they want to add new targets, but please note that additional targets does not mean additional time); BACK = back-up (when observations of the main science targets may be at risk due to specific atmospheric conditions – this applies only to Visitor Mode runs). At time of submission, the requester receives an acknowledgement message, and later on the official answer with the approval or rejection of (or part of) the request. Response time may vary, depending on the urgency of the request.

The form was publicly released on 3 July 2007 (announced under the "What's New" section of the USD P2PP public web page), simultaneously with the start of the Phase 2 preparation for Period 80. After a smooth transition period for Service Mode runs, the new procedure for target/set-up change requests is now in place also for Visitor Mode runs, as reflected in the Paranal and La Silla Science Operations pages for Visiting Astronomers (*http://www.eso.org/paranal/sciops/vm_backup.html* and *http://www.ls.eso.org/lasilla/sciops/*). We are still working on the form and small changes in its appearance will certainly appear in the coming semesters, because it is only with experience that possible shortcomings can be identified.

Personnel Movements

Arrivals (1 July–30 September 2007)

Europe	
de Zeeuw, Pieter Timotheus (NL)	Director General
Döllinger, Michaela (D)	Fellow
Hansen, Camilla Juul (DK)	Student
Hinterschuster, Renate (D)	Draughtswoman
Jochum, Lieselotte (D)	System Engineer/Physicist
Korhonen, Heidi Helena (FIN)	Fellow
Lind, Karin (S)	Student
Raiter, Anna (PL)	Student
Russo, Pedro Miguel (P)	Paid Astronomer
van Belle, Gerard (USA)	Instrument Scientist
Ventimiglia, Giulia (I)	Student
Vera Sequeiros, Ignacio (ES)	Software Engineer/Database Design

Chile	
Bensby, Thomas Lennart (S)	Fellow
Carraro, Giovanni (I)	Operations Astronomer
Garcia-Appadoo, Diego Alex (ES)	Fellow
Gutierrez, Adriana (RCH)	Administrative Assistant
Rabanus, David (D)	Telescope Scientist
Saavedra, Marcia (RCH)	Personnel Officer
Sanzana, Lilian (RCH)	Software Engineer
West, Michael (USA)	Senior Astronomer

Departures (1 July–30 September 2007)

Europe	
Bik, Adrianus (NL)	Fellow
Fedele, Davide (I)	Student
Harrison, Paul (GB)	Software Engineer
Jordán, Andrés (RCH)	Fellow
Kainulainen, Jouni (FIN)	Student
Messineo, Maria (I)	Fellow
Parker, Laura (CDN)	Fellow
Rzepecki, Jaroslaw P. (PL)	Student
Schuhler, Nicolas (F)	Optical Engineer
Silva Smiljanic, Rodolfo (BR)	Student
Thebaud, Nathalie (F)	Secretary/Assistant
Valenti, Stefano (I)	Student
Villegas Mansilla, Daniela (RCH)	Student
Zilio, Davide (I)	Student

Chile	
Anciaux, Michel (B)	Engineer
Caruso, Fabio (I)	Instrumentation Engineer
Demartis, Walter (I)	Personnel Officer
Elliott, David (GB)	Student
Galliano, Emmanuel (F)	Fellow
Papadaki, Christina (GR)	Student

Scisoft VII – with Virtual Observatory Support

Richard Hook (ST-ECF/ESO)
on behalf of the Scisoft Team

The Scisoft bundle is a collection of astronomical software intended mostly for ESO users but which is also distributed to other interested parties. It includes most of the packages needed by working observational astronomers, with emphasis on those widely used for handling optical and infrared data sets. Scisoft is installed on almost all the scientific computers running Linux at ESO Garching and widely at the ESO sites in Chile. More complete details can be found on the Scisoft web pages at *http://www.eso.org/scisoft.*

We are pleased to announce the availability of Scisoft VII (June 2007). This new version of the collection includes many updates and additional packages and also incorporates some new features. For the first time we have a collection of Virtual Observatory (VO) tools as well as extended support for longer-wavelength data handling from submillimetre facilities such as APEX.

A list of the items included in the new version, and where there are changes from the previous one, is given on the web pages. Scisoft VII was built on, and intended to be used on, Fedora Core 6 Linux, but is likely to run on many similar modern Linux systems. We no longer maintain a version of Scisoft for other architectures such as Solaris or HPUX, but a similar version for Mac OSX, produced independently of ESO, is also available through a link on the Scisoft web page.

Scisoft VII can be either downloaded from the ESO ftp site (*ftp://ftp.eso.org/scisoft/scisoft7/linux/fedora6/*) or the entire collection may be requested on DVD through the ST-ECF on-line shop at *http://www.spacetelescope.org/hubble-shop/webshop/webshop.php?show=sales&section=cdroms*. We also continue to support a mirror of the Scisoft collection in China (*http://scisoft.lamost.org/*). Note that only requests from China, to be delivered in China, are accepted by the Chinese mirror site.

Scisoft is a collaboration involving many people. I would particularly like to thank Mathias André and Jean-Christophe Malapert for their help with the preparation of the release. I would also like to thank Markus Dolensky for proposing the addition of VO content and Mark Allen (CDS, Strasbourg) for selecting the VO tools we include. We are grateful to Chenzhou Cui of the National Astronomical Observatory, Chinese Academy of Sciences, for his continued support of the Chinese mirror. Finally a special word of thanks goes to Peter Stetson (HIA, Canada) for allowing us to include DAOPhot and related tools in the collection.

Gruber Prize in Cosmology Awarded for the Discovery of the Accelerated Expansion of the Universe

Nearly a decade ago astronomers from two competing teams announced that they had found evidence for an accelerated cosmic expansion. The Gruber Prize in Cosmology 2007 honours this achievement and has been awarded to two groups: the Supernova Cosmology Project team, led by Saul Perlmutter (Lawrence Berkeley Laboratory), and the High-*z* Supernova Search Team, led by Brian Schmidt (Australian National University). Their results were based on the observations of distant Type Ia supernovae and were obtained with the major telescopes at the time (Riess et al. 1998, AJ 116, 1009; Perlmutter et al. 1999, ApJ 517, 565). Both teams used the 3.6-m telescope and the NTT to contribute photometry and spectroscopic classifications of the supernovae. Four people at ESO were directly involved in the two teams and are recognised as co-recipients of the Gruber Prize. Isobel Hook (now at Oxford University) and Chris Lidman (ESO Chile) were ESO Fellows when they contributed to the work of the Supernova Cosmology Project, while Jason Spyromilio and Bruno Leibundgut (both ESO Garching) participated in the High-*z* Supernova Search Team.

The citation by the Gruber foundation reads: “Saul Perlmutter and Brian Schmidt and their teams: the Supernova Cosmology Project and the High-*z* Supernova Search Team, independently discovered that the expansion of the Universe is accelerating. Their discovery led to the idea of an expansion force, dubbed Dark Energy. And it suggested that the fate of the Universe is to just keep expanding, faster and faster.”

The Peter and Patricia Gruber Foundation is a private, United States-based philanthropic organisation established in 1993 to honour and encourage educational excellence, social justice and scientific achievements that better the human condition.

In the meantime research on Dark Energy has become a major cosmological enterprise. Characterising the nature of Dark Energy has direct implications on particle physics as well. The original work on the cosmic acceleration has been continued and expanded by several active teams. Many of the scientists in the original teams are members of these new efforts working towards determining the equation of state of Dark Energy. Most of these experiments make extensive use of the VLT, together with Keck, Gemini and the Magellan telescopes, for the spectroscopic classification and examination of possible evolutionary trends of the supernovae.

Fellows at ESO

Steffen Mieske

Steffen Mieske

My fascination with astronomy started very early in life. At the age of 14, I wrote a 200-page science fiction novel – which nobody except my best friend and I has ever read. At about the same time, I made a very daring bet with the same friend regarding our future professions, the stake being 100 Deutsche Mark. He bet that he would become a boarding-school teacher, and I bet I would become an astronomer. Both of us have won the bet.

At Bonn University I studied physics between 1996 and 2001, and my fascination for astronomy continued. During the last year of my undergraduate studies I spent 10 months in Chile at the Astronomical Institute of the Pontificia Universidad Católica. I pursued my Ph.D. work at Bonn University between 2002 and 2005, supervised by Michael Hilker and Klaas S. de Boer. During this time I spent another 22 months at Universidad Católica, my Chilean thesis advisor being Leopoldo Infante. Back in Germany, three days before Christmas 2004 I was notified of being selected as an ESO fellow. What a nice present! I started my fellowship in August 2005.

My scientific interests focus on extragalactic globular clusters and dwarf galaxies. I am particularly interested in the transition region between these classes of objects, represented by the so-called 'ultracompact dwarf galaxies'. Furthermore, I study the peculiar velocity field in the nearby Universe and the faint end of the galaxy luminosity function.

For my functional duties, I am assigned to the User Support Department, where I support service mode runs for WFI, Feros and VIMOS. While working for ESO I have gained invaluable insights into many aspects of running the world's most advanced ground-based observatory. Personally, I have been very much impressed by the momentum gained for the E-ELT development since I started at ESO two years ago. I am looking forward to an exciting last year of my fellowship.

Julia Scharwächter

While observing stellar constellations in minus-degree German winter nights, I became interested in the physical background of night-sky phenomena. When I discovered that "astrophysicist" could also be a profession, I decided to study physics at the University of Cologne, where later I did my diploma and Ph.D. theses in astrophysics, supervised by Prof. Dr. Andreas Eckart. For my diploma thesis I used multiparticle simulations to model the dynamics of a quasar host galaxy. This aroused my curiosity about host galaxies of active galactic nuclei, the evolution and dynamics of which has since then been my main research area. As Ph.D. project, which was partly supported by a scholarship of the German National Merit Foundation, I extended my work on multiparticle modelling of quasar host galaxies and became acquainted with the reduction of a complementary set of near-infrared images and spectra.

Having completed my Ph.D. without any practical observing experience, I was eager to find a postdoc position which would involve observational tasks. The ESO fellowship in Chile was my first choice and has more than fulfilled my expectations. Since my first days in Chile in May 2005 I have been fascinated by the combination of research and functional work in a multinational environment. As for the functional part, I am assigned to La Silla science operations, where I work as a support astronomer at the NTT and, since July 2007, as the first instrument scientist for SOFI. The expertise among my colleagues and the continuous interaction with visiting astronomers provide a unique opportunity to learn about different research areas and observational techniques, as well as to advance one's own research projects with new ideas. In addition, I very much enjoy living in Chile, every now and then stealing a glance at the Andes or by night at Orion upside down.

Julia Scharwächter

ESO is the European Organisation for Astronomical Research in the Southern Hemisphere. Whilst the Headquarters (comprising the scientific, technical and administrative centre of the organisation) are located in Garching near Munich, Germany, ESO operates three observational sites in the Chilean Atacama desert. The Very Large Telescope (VLT), is located on Paranal, a 2 600 m high mountain south of Antofagasta. At La Silla, 600 km north of Santiago de Chile at 2 400 m altitude, ESO operates several medium-sized optical telescopes. The third site is the 5 000 m high Llano de Chajnantor, near San Pedro de Atacama. Here a new submillimetre telescope (APEX) is in operation, and a giant array of 12-m submillimetre antennas (ALMA) is under development. Over 1600 proposals are made each year for the use of the ESO telescopes.

The ESO Messenger is published four times a year: normally in March, June, September and December. ESO also publishes Conference Proceedings and other material connected to its activities. Press Releases inform the media about particular events. For further information, contact the ESO Public Affairs Department at the following address:

ESO Headquarters
Karl-Schwarzschild-Straße 2
85748 Garching bei München
Germany
Phone +49 89 320 06-0
Fax +49 89 320 23 62
information@eso.org
www.eso.org

The ESO Messenger:
Editor: Jeremy R. Walsh
Technical editor: Jutta Boxheimer
Technical assistant: Mafalda Martins
www.eso.org/messenger/

Printed by
Peschke Druck
Schatzbogen 35
81805 München
Germany

ISSN 0722-6691

Contents

Front Cover Picture: The southern barred spiral galaxy NGC 1313. Active star formation is evident from the presence of many H II region nebulae which surround clusters of young hot stars, including Wolf-Rayet stars (see article on page 53). This colour-composite (ESO Press Photo 43/06) is based on images obtained with the VLT FORS1 instrument.

Corrigendum: In the June issue of the Messenger (No. 128), the caption (back page, page 80) to the front cover image wrongly described the configuration of two of the three ALMA antennas. The European (AEC Consortium) antenna is in fact the one on the left and the US (Vertex RSI) antenna the one in the middle. In addition the photograph was by Herbert Zodet (ESO).